LHCb Spectrometer Alignment and Verification of its Performance using the Decay $B_d^0 \to K^{*0} J/\psi$

Dissertation

zur

Erlangung der naturwissenschaftlichen Doktorwürde
(Dr. sc. nat.)

vorgelegt der
Mathematisch-naturwissenschaftlichen Fakultät

der

Universität Zürich

von

Christophe Salzmann

von

Maschwanden ZH

Promotionskomitee

Prof. Dr. Ulrich Straumann (Vorsitz)
Dr. Olaf Steinkamp
Dr. Jeroen van Tilburg

Zürich 2012

Abstract

The LHCb detector is one of the four experiments located at the Large Hadron Collider at CERN close to Geneva and is dedicated to so-called B physics. A good vertex and momentum resolution is crucial to this experiment. Detector alignment is an essential ingredient for obtaining the best possible measurement precision of a detector.
The internal and relative alignment of the LHCb tracking subdetectors is performed using a novel method based on a Kalman filter track model. Alignment tests for the subdetector Tracker Turicensis preformed on top of the global alignment, provided important information to improve the global alignment.

Flavour changing neutral currents are suppressed in the Standard Model and therefore offer the possibility to search for processes related to new physics. The angular distribution of the weak neutral current decay $B_d^0 \to K^{*0}\mu^+\mu^-$ could deviate from Standard Model predictions, since particles predicted by new physics model could enter the process on the loop level and alter the angular distribution.
The method to extract the acceptance effects of the detector of the LHCb detector on the angular distribution of the decay is based on simulation. The agreement between data and simulation is tested using the control channel $B_d^0 \to K^{*0}J/\psi$ $(J/\psi \to \mu^+\mu^-)$. The comparison is made for the 2010 and 2011 data samples and show a good agreement.

Zusammenfassung

Der LHCb Detektor ist eines von vier Experimenten am Large Hadron Collider am CERN nahe Genf. Der Schwerpunkt des Experiments liegt in der sogenannten B-Mesonenphysik. Eine gute Vertex- und Impulsauflösung ist für dieses Experiment von zentraler Bedeutung. Die computergestützte Ausrichtung der Detektorkomponenten, auch Alignment genannt, ist ein fester Bestandteil im Verfahren eine bestmögliche Messgenauigkeit des Detektors zu erreichen.
Unter Verwendung einer neuen Methode, die sich auf ein Kalman-Filter Spurmodell stützt, werden in LHCb alle Subdetektoren gleichzeitig intern und relative zueinander in einem globalen Alignment ausgerichtet. Alignmenttests, die für den Subdetektor Tracker Turicensis ausgeführt wurden, lieferten wertvolle Informationen um das globale Alignment zu verbessern.

Flavour–ändernde Ströme sind im Standardmodell unterdrückt und ermöglichen somit die Suche nach neuen physikalischen Prozessen. Die winkelabhängige Zerfallsverteilung des schwachen neutralen Stromes $B_d^0 \to K^{*0}\mu^+\mu^-$ kann von der Vorhersage des Standardmodells abweichen. Teilchen die von neuen Physikmodellen vorhergesagt werden, können auf dem Loop-Level in den Prozess eingehen und somit die Winkelverteilung ändern. Akzeptanzeffekte des LHCb Detektors werden mittels der Detektorsimulation bestimmt. Die Übereinstimmung zwischen Daten und Simulation wurde mit Hilfe des Kontrollkanals $B_d^0 \to K^{*0}J/\psi$ $(J/\psi \to \mu^+\mu^-)$ überprüft, wobei sowohl 2010 wie auch 2011 Daten verwendet wurden. In beiden Fällen zeigt sich eine gute Übereinstimmung.

Contents

Introduction

Particle physics is the study of the smallest constituents of our universe, the elementary particles. Today, men know that all visible matter in our universe is built up of electrons and up- and down-quarks.
The first elementary particle was discovered by Joseph J. Thomson in 1897, who discovered the electron while investigating cathode rays. This experiment was comparatively simple. To discover the quarks postulated in the 1960s much larger facilities were needed. Today, particle physics uses large accelerators and detectors, which act as huge microscopes to probe elementary particles and their related processes. So far, the most powerful accelerator built by man is the Large Hadron Collider located at CERN close to Geneva. Four detectors are built around the accelerator to study the particle collisions generated by the accelerator.

Over the last five decades particle physics experiments confirmed the well established Standard Model of particle physics. All elementary particles predicted by the Standard Model have been discovered except the Higgs, which is the elementary particle supposed to give mass to all other elementary particles. To discover this final piece of the Standard Model is one of the reasons why physicists built the Large Hadron Collider.
Even if the Higgs is discovered the Standard Model would not be the final truth. The Standard Model is not able to solve the problem of the divergent mass of the Higgs. Moreover, many questions related to unexplainable phenomena in our universe remain unanswered. Only a small fraction of matter and energy can be explained by the Standard Model. The Large Hadron Collider offers the opportunity to search for new physical processes in the particle collisions which could give an explanation to these open issues.

The LHCb experiment is specially designed to investigate bottom quark decays via neutral currents, which are strongly suppressed in the Standard Model, to a high precision. New physical processes are expected to change the behaviour of such decays compared to the expectations of the Standard model. This thesis presents measurements performed on data collected by the LHCb experiment in 2010 and 2011.

The first Chapter of this thesis gives an overview of the physics motivation leading to this thesis. The Standard Model is briefly introduced, flavour changing neutral currents are discussed and an overview of measured results is given.

The facilities needed to perform particle physics experiments, i.e. the Large Hadron Collider and the LHCb detector, are described in the second Chapter. The detailed modelling of the Tracker Turicensis used in the detector description is presented in Chapter 3.

The internal and relative global alignment of the LHCb tracking system and the additional alignment tests performed for the Tracker Turicensis are described in Chapters 4 and 5.

Chapter 6 presents the comparison between data and simulation using the control channel $B_d^0 \to K^{*0} J/\psi$ $(J/\psi \to \mu^+\mu^-)$ for data collected in 2010 and 2011. Cross check measurements on the $b\bar{b}$ cross section and the Forward-Backward Asymmetry are also shown. The thesis concludes with a summary.

Chapter 1

Physics motivation

The *Standard Model* (SM) of particle physics describes elementary particle interactions to impressive precision. However, the SM yields unphysical results for one of its fundamental particles, the Higgs. The calculated Higgs mass including radiative corrections diverges quadratically as a function of the energy. Furthermore, there are open questions that do not find an explanation in the SM. For instance, it does not explain the evident imbalance between matter and anti-matter in the universe. Other hints of the existence of *New Physics* (NP) are the presence of *Dark Matter* and *Dark Energy*. In the last twenty years a main focus of particle physics research has been to provide a physical explanation to these observations, looking for NP in particle physics processes. This chapter gives a brief introduction to the SM in the first section. In the second chapter the mechanism leading to processes which are suppressed in the SM is discussed. Section 1.3 introduces the operator production expansion, which distinguishes between short and long range interactions and is commonly used to describe heavy quark physics. Finally, experimental results regarding the decay $B_d^0 \to K^{*0}\mu^+\mu^-$ and their comparison with SM predictions are discussed.

1.1 The Standard Model of particle physics

The Standard Model describes the electromagnetic, weak and strong interaction. It is composed of the *Glashow-Salam-Weinberg* model, which unifies the weak and the electromagnetic to the electroweak interaction, and *Quantum Chromodynamics* (QCD), which describes the strong interaction. The fourth fundamental force, gravity, is not included in the SM. A detailed introduction to the SM is given in Ref. [1]. All particles of the SM have been observed apart from the Higgs boson.

In the Standard Model all matter consists of twelve fermions, six quarks and six leptons, which all have an intrinsic spin 1/2. The strong force only acts on quarks. They are the elementary particles which build up nucleons (protons and neutrons). The quarks form three generations, distinguished by increasing mass. Each generation contains two quarks, one *up* and one *down* type quark, according to the names of the two quarks of the first generation. The up type quarks have an electrical charge of +2/3, the down type quark of -1/3. The properties of the quarks are listed in Tab. 1.1.

Quarks

Generation	Particle	Symbol	Charge	Mass [GeV]
1	up quark	u	2/3	$1.7–3.1 \cdot 10^{-3}$
	down quark	d	-1/3	$4.1–5.7 \cdot 10^{-3}$
2	charm quark	c	2/3	1.2–1.3
	strange quark	s	-1/3	$80–130 \cdot 10^{-3}$
3	top quark	t	2/3	172.9
	bottom quark	b	-1/3	4.2

Table 1.1: The quarks of the Standard Model of particle physics.

The leptons are also divided into three generations containing two particles each. The generations contain an electrically neutral neutrino and the electron-like particle with an electrical charge of -1.
Every fermion has an antiparticle, which is identical to the particle itself, except that all charge-like quantum numbers have opposite sign.

Leptons

Particle	Symbol	Charge	Mass [MeV]	Generation
1	electron-neutrino	ν_e	0	$< 2.3 \cdot 10^{-6}$
	electron	e	-1	0.511
2	muon-neutrino	ν_μ	0	< 0.19
	muon	μ	-1	105.7
3	tau-neutrino	ν_τ	0	< 18.2
	tau	τ	-1	$1.8 \cdot 10^3$

Table 1.2: The leptons of the Standard Model of particle physics.

Interactions between matter particles are mediated by bosons with integral intrinsic spin. These are the gluons g for the strong force, the photon γ for the electromagnetic force and the $W^\pm$ and Z^0 bosons for the weak force, respectively. Table 1.3 lists the SM forces and the corresponding bosons.

Bosons

Particle	Symbol	Charge	Mass [GeV]	Force mediated	Relative strength
gluon	g	0	0	Strong	$\mathcal{O}(1)$
photon	γ	0	0	Electromagnetic	$\mathcal{O}(10^{-2})$
W^+ boson	W^+	+1	80.4	Weak	$\mathcal{O}(10^{-6})$
W^- boson	W^-	-1	80.4		
Z boson	Z	0	91.2		

Table 1.3: The bosons of the Standard Model of particle physics, which are the force carriers of the three fundamental forces in the SM.

The strong force couples to the colour charge of the quarks, which can be red, green or blue. For anti-quarks the colours are anti-red, anti-green or anti-blue. Quarks only occur in bound states inside colour neutral objects. These correspond to baryons composed of three quarks with different colour and mesons composed by a quark and an anti-quark. In B mesons one of the two quarks is a b quark. The electromagnetic force acts only on electrically charged particles. The weak force couples to all fermions.

1.2 The CKM matrix and flavour changing neutral currents

The bosons of the weak force change the quark flavour. However, the quark mass eigenstates are not the same as the quark weak eigenstates. This means that the weak force bosons couple to a mixture of weak eigenstates. The Cabibbo-Kobayashi-Maskawa (CKM) quark mixing matrix [2, 3] gives the composition of the weak eigenstates (d', s', b') in terms of the mass eigenstates (d, s, b) via

$$\begin{pmatrix} d' \\ s' \\ b' \end{pmatrix} = V_{CKM} \begin{pmatrix} d \\ s \\ b \end{pmatrix} , \tag{1.1}$$

where

$$V_{CKM} = \begin{pmatrix} V_{ud} & V_{us} & V_{ub} \\ V_{cd} & V_{cs} & V_{cb} \\ V_{td} & V_{ts} & V_{tb} \end{pmatrix} \tag{1.2}$$

is the CKM quark mixing matrix.

Flavour changing neutral currents (FCNC) at tree level are highly suppressed in the SM. This is explained by the *GIM* mechanism [4]. The transition contributions from the exchange of a Z^0, like $s \to d$, cancel each other out. However, in higher order such FCNC are allowed in the SM through so-called box or penguin diagrams. Figure

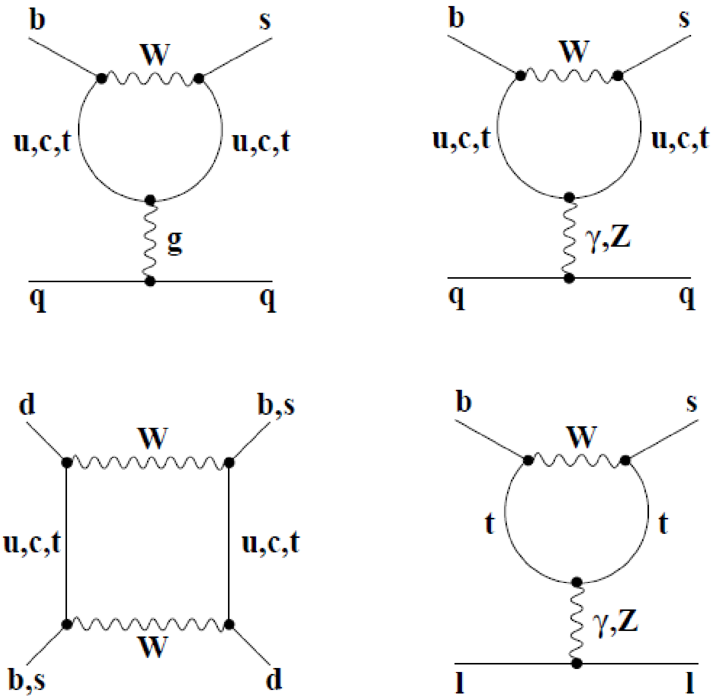

Figure 1.1: FCNC in the SM. The diagram on the bottom left is a so-called box diagram referring to its shape . All other diagrams are penguin diagrams.

1.1 shows a few diagrams that can lead to FCNC in the SM. These kind of decays are strongly suppressed as they require two weak interactions in one process and therefore are often referred to as rare decays. This implies that contributions from NP processes can enter at the same level as the SM contributions. One promising test for NP is the decay $B_d^0 \to K^{*0}\mu^+\mu^-$, which is a FCNC and has a branching ratio of the order $\mathcal{O}(10^{-6})$. Figure 1.2 shows the dominating Standard Model decay diagrams.

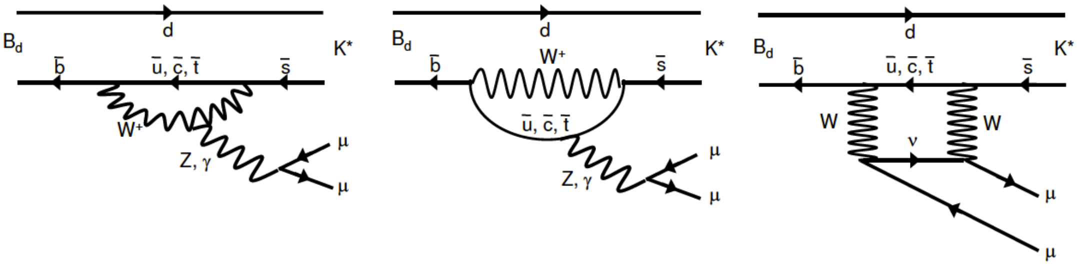

Figure 1.2: Dominant SM decays for the decay $B_d^0 \to K^{*0}\mu^+\mu^-$.

Particles postulated by models beyond the SM can enter the process in the loops and in the case of the decay $B_d^0 \to K^{*0}\mu^+\mu^-$ could alter the angular distribution of the final state particles. Figure 1.3 shows as an example how charged Higgs bosons could enter into the decay. Higgs bosons are scalar particles, with an intrinsic spin 0, whereas W bosons are vector particles with an intrinsic spin 1. Therefore, the angular distribution of the muons could be affected by processes involving the Higgs.

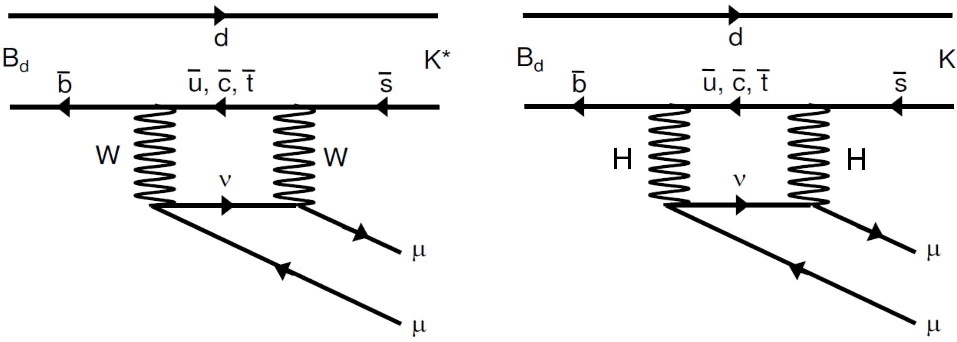

Figure 1.3: How particles from extension of the SM can enter the decay $B_d^0 \to K^{*0}\mu^+\mu^-$. A SM process is shown where the quark transitions are performed by W bosons (left). The same digram is shown where the quark transition is performed by charged Higgs bosons (right). Such Higgs bosons do not exist in the SM.

1.3 The OPE formalism of semi-leptonic B decays

The decay amplitude $A(B \to f)$ of a B meson into a final state f can be described using an effective Hamiltonian

$$A(B \to f) = \langle f|\mathcal{H}_{eff}|B\rangle \ . \tag{1.3}$$

The decays themselves are induced by the weak force. However, strong and electromagnetic interactions have an influence on the particles involved in the decay. Because of the large mass of the weak force carriers, $W^\pm$ and Z^0, the weak force acts only over a short range $\mathcal{O}(10^{-18}\text{m})$. Comparatively, the strong force acts over short and long ranges. One can separate the short and the long range interaction contributions using the operator product expansion (OPE). The OPE introduces coefficients that take into account the weak and strong short range interactions, which are calculated by perturbative methods. Figure 1.4 illustrates how the W interaction gets wrapped into a coefficient of a four fermion interaction. The effective Hamiltonian can then be written as a linear combination of fermion operators which yield the transition from the initial state to the final state.

$$\langle f|\mathcal{H}_{eff}|B\rangle = \frac{4G_F}{\sqrt{2}}\lambda_{CKM}\sum_i C_i(\mu)\langle f|Q_i(\mu)|B\rangle \tag{1.4}$$

Here, G_F is the Fermi constant and λ_{CKM} is a quark transition factor from the CKM matrix. The short range weak and strong force interaction contributions are wrapped into the Wilson coefficients C_i. The operators are represented by Q_i, and μ is the scale marking the transition from the long to the short range interactions. For B physics the scale μ is of the order $\mathcal{O}(m_b)$. The Wilson coefficient accounts for all kind of short range interactions.

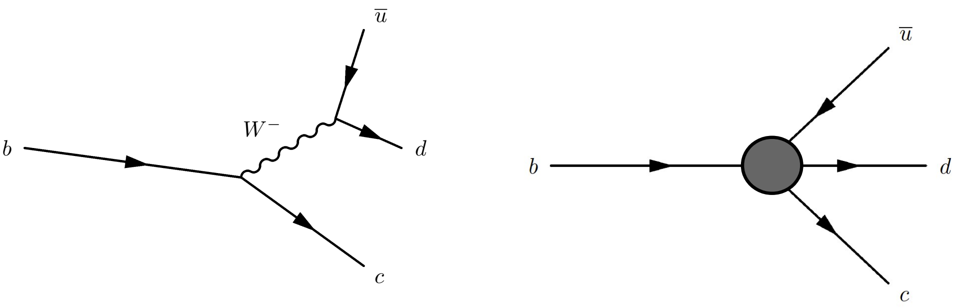

Figure 1.4: Illustration of the OPE. The $b \to c$ quark transition is shown for the full theory (SM) on the left. The effective theory is shown on the right where the short range interaction W is included in the four fermion coupling.

The operators Q_i are classified according to their Lorentz structure, so different decays receive contributions from different operators. New Physics can manifest itself in a given decay either adding new operators, not present in the SM, or by changing the Wilson coefficients for the operators already present in the SM. This thesis is concerned with the analysis of the decay $B_d^0 \to K^{*0}\mu^+\mu^-$. This decay is sensitive to the following operators:

$$Q_7 = \frac{e}{16\pi^2}m_b\left(\bar{s}\sigma^{\mu\nu}\frac{1}{2}(1+\gamma_5)b\right)F_{\mu\nu}\ , \tag{1.5}$$

$$Q_7' = \frac{e}{16\pi^2}m_b\left(\bar{s}\sigma^{\mu\nu}\frac{1}{2}(1-\gamma_5)b\right)F_{\mu\nu}\ , \tag{1.6}$$

$$Q_9 = \frac{e^2}{16\pi^2}\left(\bar{s}\gamma_\mu\frac{1}{2}(1-\gamma_5 b\right)\left(\bar{l}\gamma^\mu l\right)\ , \tag{1.7}$$

$$Q_{10} = \frac{e^2}{16\pi^2}\left(\bar{s}\gamma_\mu\frac{1}{2}(1-\gamma_5)b\right)\left(\bar{l}\gamma^\mu\gamma_5 l\right)\ , \tag{1.8}$$

with $\sigma^{\mu\nu} = [\gamma^\mu, \gamma^\nu]$ and where $F_{\mu\nu}$ and $G^\alpha_{\mu\nu}$ are the electromagnetic and the strong interaction tensor, respectively. The electric charge is denoted by e. The operators Q_7 and $Q_{9/10}$ are illustrated in Fig. 1.5

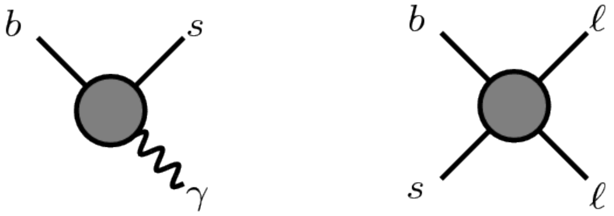

Figure 1.5: Illustrations of the operator Q_7 (left) and for the operators Q_9 and Q_{10} (right).

1.4 Probing New Physics with $B_d^0 \to K^{*0}\mu^+\mu^-$

The kinematics of the decay $B_d^0 \to K^{*0}\mu^+\mu^-$ can be described by the variables q^2, θ_L, θ_K and ϕ, where q^2 is the di-muon invariant mass, θ_L is the angle between between the B_d^0 ($\overline{B_d^0}$) flight direction and the positive (negative) muon direction in the di-muon rest frame, θ_K is the angle between the kaon and the B_d^0 flight direction in the K^{*0} rest frame, and ϕ is the angle between the $K\pi$ plane and the $\mu^-\mu^+$ plane in the B_d^0 rest frame [5]. The variables are illustrated in Fig. 1.6.

Several angular observables can be measured which are predicted with small theoretical uncertainties in the SM [6]. The partial decay rates

$$\frac{\partial^2\Gamma}{\partial\theta_L\partial q^2}\,, \qquad \frac{\partial^2\Gamma}{\partial\theta_K\partial q^2} \qquad \text{and} \qquad \frac{\partial^2\Gamma}{\partial\phi\partial q^2} \tag{1.9}$$

can be expressed in terms of the observables A_{FB}, F_L, A_T^2 and A_{Im} [7]. F_L denotes the fraction of longitudinal K^{*0} polarisation and A_T^2 is the transverse asymmetry. A_{FB} is the Forward-Backward Asymmetry and is the most popular of these observables. The partial decay rates are:

$$\frac{\partial^2\Gamma}{\partial\theta_L\partial q^2} = \left(\frac{3}{4}F_L\sin^2\theta_L + \frac{8}{3}(1-F_L)(1+\cos^2\theta_L) + A_{FB}\cos\theta_L\right)\sin\theta_L\,, \tag{1.10}$$

$$\frac{\partial^2\Gamma}{\partial\theta_K\partial q^2} = \frac{3}{4}\sin\theta_K\left(2F_L\cos^2\theta_K + (1-F_L)\sin^2\theta_K\right)\,, \tag{1.11}$$

$$\frac{\partial^2\Gamma}{\partial\phi\partial q^2} = \left(1 + \frac{1}{2}(1-F_L)A_T^2\cos^2\phi + A_{Im}\sin^2\phi\right)\,. \tag{1.12}$$

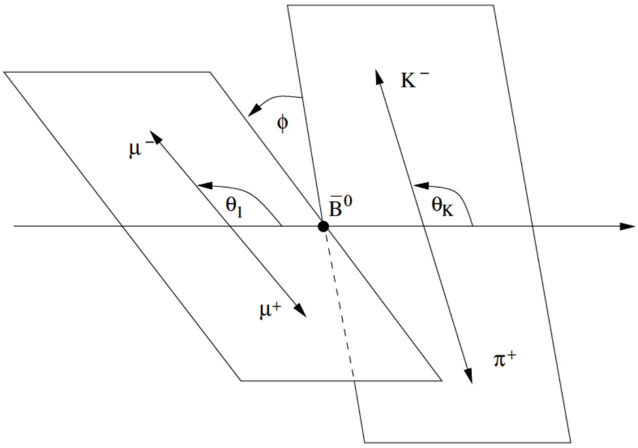

Figure 1.6: Definition of the four variables q^2, θ_L, θ_K and ϕ kinematically describing the decay $B_d^0 \to K^{*0}\mu^+\mu^-$. The horizontal line gives the $\overline{B_d^0}$ flight direction. The K and π and the $\mu^+\mu^-$ are given in the K^{*0} and in the di-muon rest frame respectively. The two frames represent the different rest frames.

The A_{FB} for the B_d^0 ($\overline{B_d^0}$) as a function of the di-muon invariant mass q^2 is defined as the number of forward- and backward-emitted positive (negative) muons in the di-muon rest frame

$$A_{FB}(q^2) = \frac{\int_0^1 \frac{\partial^2\Gamma}{\partial q^2 \partial cos\theta_L} \mathrm{d}\ \cos\ \theta_L - \int_{-1}^0 \frac{\partial^2\Gamma}{\partial q^2 \partial cos\theta_L} \mathrm{d}\ \cos\ \theta_L}{\int_0^1 \frac{\partial^2\Gamma}{\partial q^2 \partial cos\theta_L} \mathrm{d}\ \cos\ \theta_L + \int_{-1}^0 \frac{\partial^2\Gamma}{\partial q^2 \partial cos\theta_L} \mathrm{d}\ \cos\ \theta_L}\ . \tag{1.13}$$

Figure 1.7 shows A_{FB} as a function of q^2 for the SM and popular extensions of the SM [8], such as Minimal Flavour Violating models (MFV) and Minimal Supersymmetric Standard Models (MSSM). In MFV models the flavour violation structure of the SM is preserved. New parameters describing flavour violation are added to those present in the CKM matrix in the SM. The deviations of MFV models from the SM in the observables are small as processes are all SM like. In this class of models, the largest effects are calculated for a unified extra dimension model (UED). The MSSM include a symmetry between fermions and bosons not present in the SM. This symmetry adds to every fermion (boson) in the SM a corresponding supersymmetric boson (fermion). The number of additionally needed Higgs is kept to a minimum, i.e a second doublet. In General Supersymmetric Standard Models (GMSSM) the supersymmetric partners of the quarks can mix additionally, whereas in Flavour Blind Minimal Supersymmetric Standard Models (FBMSSM) the CKM matrix remains the only source of flavour violation.

The angular distributions of the decay $B_d^0 \to K^{*0}\mu^+\mu^-$ have already been measured at Babar [9], Belle [10] and CDF [11]. Figure 1.8 shows A_{FB} measured by the three

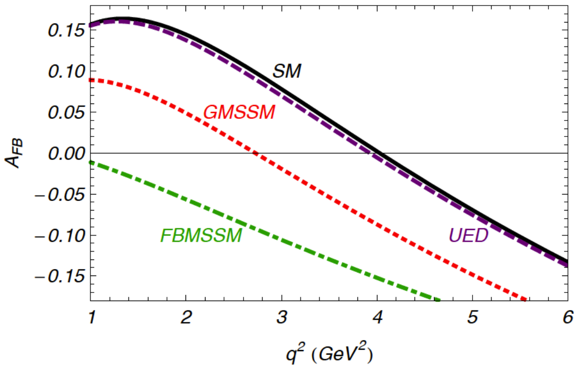

Figure 1.7: The A_{FB} as a function of q^2 predicted by the Standard Model (SM) and popular NP models [8].

Experiment	# of events (type)
Babar [9]	60 ($B^0_d \to K^{*0}\ell^+\ell^-$)
Belle [10]	230 ($B^0_d \to K^{*0}\ell^+\ell^-$)
CDF [11]	100 ($B^0_d \to K^{*0}\mu^+\mu^-$)
LHCb [12]	323 ($B^0_d \to K^{*0}\mu^+\mu^-$)

Table 1.4: The number of $B^0_d \to K^{*0}\ell^+\ell^-$ events analysed by the different experiments.

experiments. In each of the plots the solid line shows the SM prediction. All three experiments seem to find an opposite sign of A_{FB} with respect to what is expected in the SM in the low q^2 region. However, the errors are still large due to the limited statistics collected by these experiments (see Tab. 1.4). If this is confirmed with better statistical precision this would be an unambiguous sign of NP. Note that these plots use the opposite sign convention from the theoretical predictions shown in Fig 1.7.

The LHCb experiment (see Sec. 2.4) has been designed to study B physics and offers unique possibilities to improve the precision of these measurements. High statistics of B mesons (see Tab. 1.4), good momentum resolution and excellent particle identification capabilities allow for a precise measurement of the angular observables. A_{FB} and F_L are extracted by simultaneously fitting the B^0_d mass distribution and the cosθ_L and cosθ_K distributions [12]. The measurements of A_{FB}, F_L and the differential branching fraction using 309 pb^{-1} collected in 2011 are shown in Fig. 1.9. The results are in good agreement with the SM prediction [13]. The discrepancy to SM predictions at low q^2, seen by the previous experiments, is not confirmed. LHCb collected already more than 1 fb^{-1} by now and expects to collect another 2 fb^{-1} by the end of 2012 and thus more precise results on the angular distributions are expected.

The extraction of A_{FB} and F_L requires a precise knowledge of the detector accep-

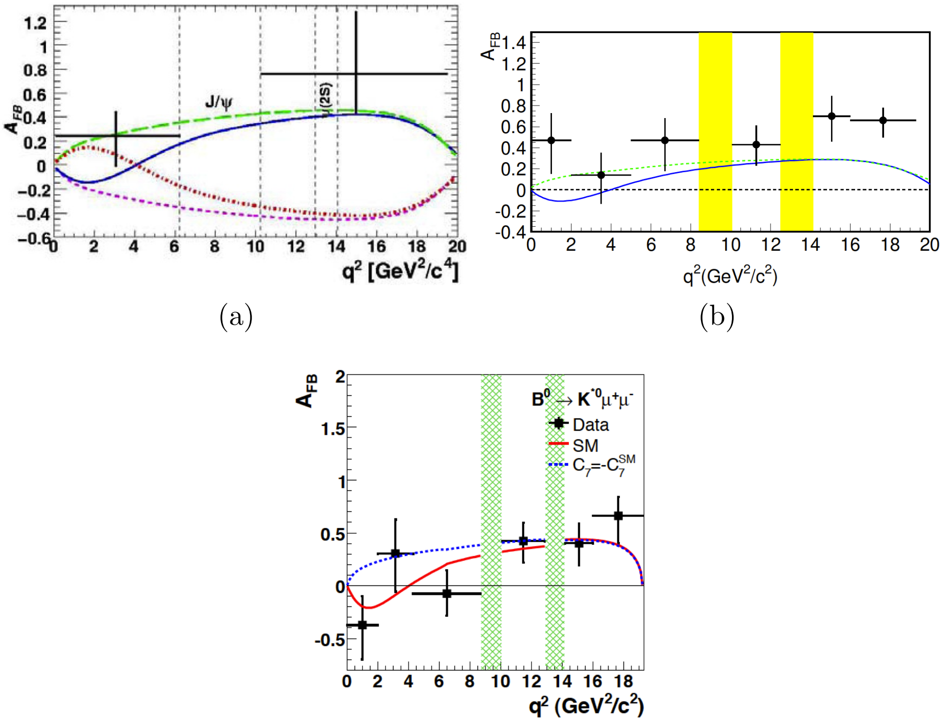

(a) (b)

(c)

Figure 1.8: A_{FB} as a function of the di-muon invariant mass q^2 for the experiments Babar (a), Belle (b) and CDF (c). The Standard Model prediction is marked by the solid line in each of the plots. The shaded area show the excluded di-muon resonances J/ψ and $\psi(2S)$. The green dashed line in (a) and (b) show the prediction if the Wilson coefficient $C_7 = -C_7^{SM}$. The same is shown in (c) by the blue dashed line. The other lines show the predictions for Wilson coefficients with opposite sign from the SM.

tance. This information is obtained from studies based on a full detector simulation. Tests need to be done to show that this simulation reproduces accurately the momentum spectra of the B mesons and decay products and the distortion of the angular distributions introduced by the experimental apparatus. In this thesis an analysis on the data collected in 2010 and 2011 using the decay $B_d^0 \to K^{*0}J/\psi$ $(J/\psi \to \mu^+\mu^-)$ is made to test the accuracy of the simulation and to show that an unbiased extraction of A_{FB} is possible. This work was fundamental to test the complete analysis before accessing to the angular observable of the signal.

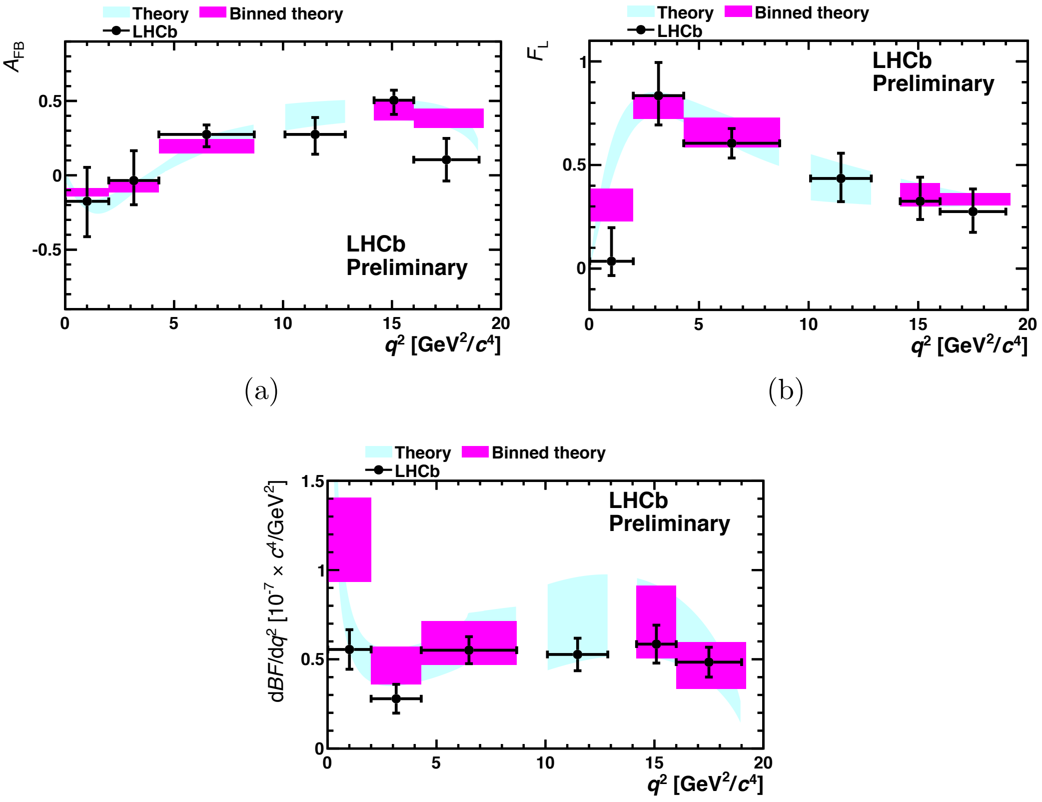

(a)

(b)

(c)

Figure 1.9: A_{FB}, F_L and the differential branching fraction as a function of q^2 measured at LHCb. The results are in good agreement with the SM prediction shown in Ref. [13].

Chapter 2

Experimental environment

To study physical processes as they took place in the early universe large facilities are necessary to simulate the same conditions nowadays. To reach these conditions one has to obtain large energy densities. Colliding protons at high energy can offer the required energy densities. The laboratories of the European Organisation for Nuclear Research (CERN) run a proton collider called Large Hadron Collider (LHC). The proton collision points are surrounded by large detectors measuring the processes taking place right after the collision. This chapter gives an overview of the experimental environment. The first section gives information about the research laboratory CERN. Section 2.2 shows an overview about the LHC. The B production at LHC is discussed in Sec. 2.3. Finally, the last section discusses the detector of the LHCb experiment with a focus on the tracking system.

2.1 CERN

CERN (**C**onseil **E**uropéen pour la **R**echerche **N**ucléaire) was founded in 1954 by 12 European members and is located near Geneva on the border between Switzerland and France. The collaboration among European countries now has 20 members.

The first accelerator was set up in 1957, the synchrocyclotron with a beam energy of 600 MeV. Two years later a proton synchrotron (PS) started its operation and is still operating today. In 1971 the first proton-proton collider was finalised with a diameter of 300 m. At that time this was a very large machine. The SPS (Super Proton Synchrotron) build in 1976 with a circumference of 7 km marks the next big step in terms of particle accelerators. This accelerator is still used today to pre-accelerate protons before they get injected into the main accelerator. In 1989 the Large Electron Positron collider (LEP) started operating, located in a 27 km circular tunnel. LEP stopped running in the year 2000 to make way for the Large Hadron Collider (LHC) that is installed in the same tunnel. The LHC started running for the first time in 2008. The LHC is designed to reach a beam energy of 7 TeV, a beam energy more than 10000 times higher than the one achieved by the very first accelerator located at CERN. Figure 2.1 shows a schematic view of the accelerator facilities operating today at CERN with its four detectors LHCb, ATLAS, CMS and ALICE.

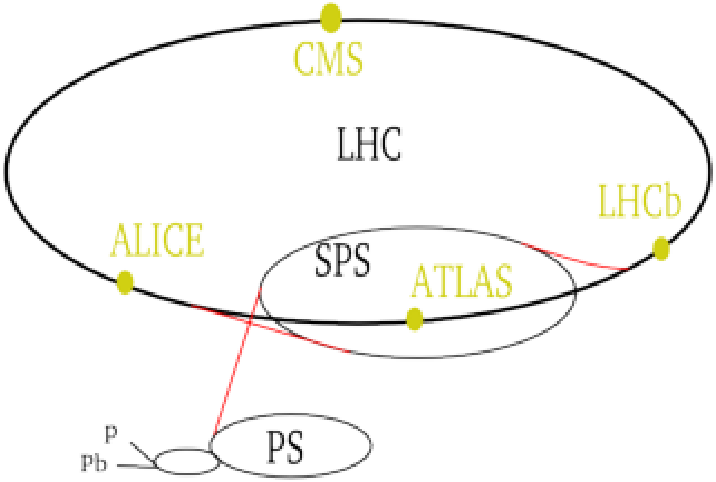

Figure 2.1: The LHC with its pre-accelerators and the four experiment located at the LHC.

ATLAS [14] and CMS [15] are so-called multi-purpose detectors, in first order designed to discover the Higgs. The ALICE detector [16] is tuned to physics taking place in heavy-ion collisions. The fourth experiment at LHC is the **L**arge **H**adron **C**ollider **b**eauty experiment (LHCb), dedicated to B physics. The following sections will focus on this experiment.

2.2 The Large Hadron Collider

The Large Hadron Collider [17, 18] is located in the tunnel 100 m underground, where previously LEP was located. Two oppositely circulating proton beams are brought to collision at four different collision points. The designed proton beam energy is 7 TeV resulting in a centre-of-mass energy of 14 TeV. Figure 2.2 shows a comparison of the LHC to previous accelerators. Before protons can be accelerated to such energies they have to run through a cascade of pre-accelerators. The protons are accelerated first in the PS to an energy of 25 GeV and subsequently in the SPS to 450 GeV before they

get injected into the LHC.
The proton beam is kept on its circular trajectory via superconductive magnets. As superconductivity sets in only at very low temperature, the machine has to be cooled down to 1.9 K. The beam energy and the radius of the ring define the strength of the magnetic field. Each of the total 1232 superconducting dipole magnets along the 27 km long tunnel has to reach a magnetic field strength up to 8.33 T.

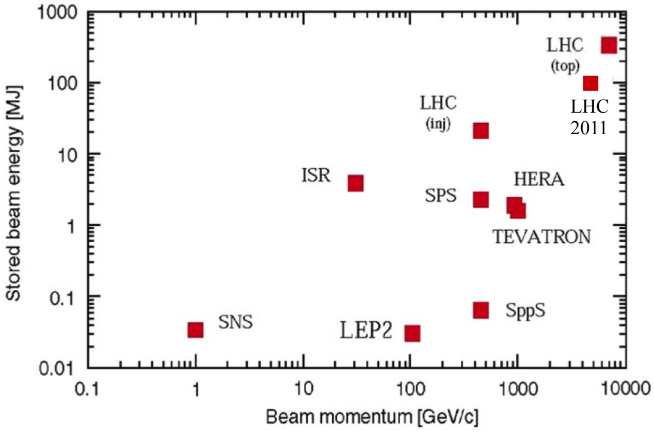

Figure 2.2: The LHC compared to previous accelerators. The LHC reaches orders of magnitude higher energies.

The proton beam is not a continuous beam, but consists of 2808 bunches filled with approximately 10^{11} protons. The time spacing between the bunches is 25 ns resulting in a collision frequency of 40 MHz. The bunch time spacing will allow for about 3600 bunches in the 27 km long tunnel, but due to the beam filling procedure only 2808 bunches are filled reducing the average collision frequency down to 30 MHz.

The performance of an accelerator is given by the beam energy and the luminosity. The luminosity is the number of collisions of beam particles at an interaction point per second per cm^2 . The number of collisions during a time period Δt, is given by

$$N_{collision} = \sigma_{inel} \int_0^{\Delta t} \mathcal{L} \, dt \ , \tag{2.1}$$

where $\sigma_{inel} = 80$ mb (1 mb $= 10^{-27}$ cm^2) is the inelastic cross section for *pp* collisions at a centre-of-mass energy $\sqrt{s} = 14$ TeV [19]. The Poisson statistic gives the probability of a given number of interactions n in a bunch crossing with a mean μ,

$$P(n, \mu) = \frac{\mu^n}{n!} e^{-\mu} \ . \tag{2.2}$$

The mean μ is related to the luminosity via

$$\mu = \frac{\sigma_{inel} \mathcal{L}}{f} \ , \tag{2.3}$$

(a) (b)

Figure 2.3: The start of LHC on the 10 September 2008 attracted much interest from the public and the media . Google designed an extra logo for that day (a) and the LHC control room was crowded by journalists (b) (© Google and CERN).

where f is the crossing rate of colliding bunches at a given interaction point.

On the 10 September 2008 the very first bunches were injected into the LHC starting a new era in particle physics attracting much interest of the media and the public (see Fig. 2.3). The commissioning of the accelerator went smoothly and fast. Unfortunately, on the 19 September 2008 a failure in a soldered joint between two magnets caused a severe accident putting the machine out of order for more than a year [20].

The LHC resumed in November 2009 delivering pp collision at the injection energy of 450 GeV. Shortly after, a centre-of-mass energy of $\sqrt{s}$ = 2.1 TeV was reached, setting a new record for the highest centre-of-mass energy ever achieved in a particle accelerator, beating that achieved at the Tevatron ($\sqrt{s}$ = 1.96 TeV). From March to November 2010 the Large Hadron Collider was operated the first time for a longer period at an even larger centre-of-mass energy $\sqrt{s}$= 7 TeV delivering an integrated luminosity of 36 pb^{-1} to the *B* physics experiment LHCb. The machine will be operated at the beam energy of 3.5 TeV until 2012. After a shutdown and repair work related to the 2008 incident, the LHC will be ramped up to the designed centre-of-mass energy of $\sqrt{s}$ = 14 TeV.

2.3 *B* meson production at LHC

B mesons originate from hadronising $b\bar{b}$ pairs created during the proton-proton collisions. Four different processes contribute to the $b\bar{b}$ cross section $\sigma_{b\bar{b}}$ [21]. The largest contribution, 60%, comes from flavour excitation. Every fourth $b\bar{b}$ pair is created by

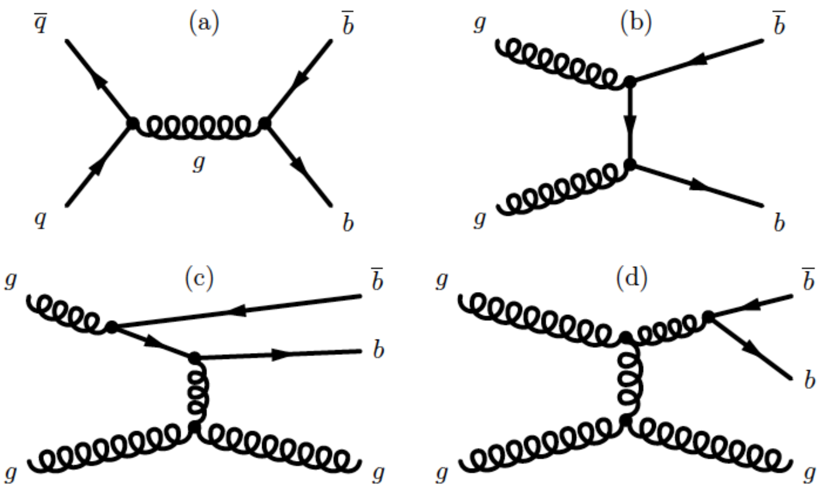

Figure 2.4: Feynman diagrams of the processes contributing to $b\bar{b}$ pair production. The quark-antiquark annihilation shown in (a) and the quark fusion in (b) contribute 15% to the total $b\bar{b}$ production cross section. The larges contribution of 60% comes from flavour excitation (c) and the gluon splitting (d) contributes 25%. The contributions are the numbers used in PYTHIA [22].

gluon splitting. The rest comes from pair creation, that is gluon fusion or $q\bar{q}$ annihilation, where the contribution from the latter one is marginal. The numbers given are the ones used in *B* meson production simulation using PYTHIA [22]. Figure 2.4 shows Feynman diagrams of the four processes producing $b\bar{b}$ pairs. The large momentum difference of the two partons involved in the $b\bar{b}$ pair creation at $\sqrt{s} = 14$ TeV leads to a boost in the forward or backward direction. Consequently, *B* mesons are produce mainly under small polar angles. Figure 2.5 shows the correlation of the production angle of the two *b* quarks. The production of *B* mesons in comparatively small cones along the beam pipe motivates the design of the LHCb detector as a single arm forward spectrometer.

The expected $b\bar{b}$ cross section at the LHC running at $\sqrt{s} = 14$ TeV is $\sigma_{b\bar{b}} = 500$ μb. Since the accelerator is running only at half its designed energy the cross section reduces and is measured to $\sigma_{b\bar{b}} = 284 \pm 69$ μb [23]. In addition to the lower centre-of-mass energy, the number of bunches per beam is lower than the designed 2808. A bunch spacing of down to 150 ns allows for approximately 400 bunches per beam in the 2010 data. In 2011 the spacing was reduced to 50 ns giving space to more than 1000 bunches per fill.

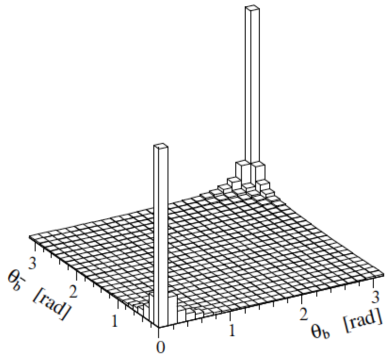

(a)

Figure 2.5: The simulated correlation of the polar angle of the two b quarks produced in a proton-proton collision with a centre-of-mass energy of 14 TeV (a).

2.4 The LHCb experiment

The Large Hadron Collider Beauty (LHCb) experiment [19, 24, 25] is designed as a single arm forward spectrometer dedicated to B physics. This configuration optimises the number of B mesons detected per sensitive detector area. Figure 2.6 shows a side view of the detector in the y-z plane. The z axis is defined in positive direction from the interaction point through the detector along the beam pipe. Upstream names the positive z direction and downstream the negative direction. The y axis is defined vertically perpendicular to the z axis, the positive direction pointing upwards. The x axis is defined perpendicular to the two other axes building a right handed coordinate system. This coordinate system corresponds to the LHC coordinate system. The origin of the coordinate system coincides with the interaction point. According to their position relative to the beam pipe, detector components are called to be on the A- or C-side, or on the top or bottom, respectively. The A-side (access) denotes the area with positive x values, the C-side (cryo) the one with negative x values. Detector components called to be top are located above the beam pipe, those below the beam pipe are called bottom.

Basically, the subdetectors of LHCb can be divided into two classes: the tracking detectors and the particle identification (PID) detectors. The subdetectors are classified as follows:

- **tracking detectors**:
  The **Ve**rtex **Lo**cator (VELO), the Tracker Turicensis (TT)[1], the Inner Tracker

---

[1] Previously, the Tracker Turicensis was called Trigger Tracker, supposed to provide momentum information to the trigger. After losing its purpose as part of the trigger, it was renamed after its place of development, which is Zürich, known as Turicum during the Roman Empire.

(IT) and the Outer Tracker (OT).

- **PID detectors**:
  The two Ring Imaging Cherenkov detectors RICH1 and RICH2, the electromagnetic and hadronic Calorimeter (ECAL and HCAL) and the five muon stations (M1 - M5).

The last component finally, is the magnet located between the tracking detectors needed to determine the momentum of charged particles. The main component of the magnetic field points in z direction, bending charged particles in x direction. In the bending plane the detector covers a region between $15 < \theta < 300$ mrad, where θ is the angle to the beam pipe. In the non-bending plane the range is $15 < \theta < 250$ mrad. All over, the dimensions of the LHCb detector are 6 m × 5 m × 20 m (x, y, z).

LHCb is meant to be operated at an instantaneous luminosity of $\mathcal{L} = 2 \cdot 10^{32}$ $\text{cm}^{-2}\text{s}^{-1}$. To lower the nominal luminosity of the LHC of $\mathcal{L} = 10^{34}$ $\text{cm}^{-2}\text{s}^{-1}$ the beam gets less focussed at the LHCb interaction point. However, all the subdetectors are designed to cope with a peak instantaneous beam luminosity of $\mathcal{L} = 5 \cdot 10^{32}$ $\text{cm}^{-2}\text{s}^{-1}$.

A component of the experiment not obviously visible, but not less important is the trigger. The trigger has to select the events of interest and to reject background events. Analysing all events produced at a collision rate of 40 MHz would take to much time and computational power. The aim of the trigger is to cut this rate down to a feasible level. It is separated into three levels, a hardware trigger called L0, and two software triggers HLT1 and HLT2.

The lower cross section and the smaller number of bunches per beam reduce the number of produced $b\bar{b}$ pairs considerably. Alternatively, the beam conditions can be changed that way, that the average number of interactions per collision is increased. The luminosity $\mathcal{L}$ can be increased by focusing the beam more at the interaction point. It should be noted that more interactions per bunch crossing lead to a higher occupancy in the detector affecting the precision of the experiment.
The LHCb detector was designed for an average number of collisions per event $\mu \approx 0.5$. To compensate for the lower beam energy and the lower number of bunches per fill μ is set to values larger than the designed one. In 2010 LHCb operated with μ up to a maximum of 2.7. In 2011 the average μ is about 1.5.

2.5 The tracking system

The tracking system comprises three parts. The VELO located at the interaction point, the Tracker Turicensis between the RICH1 and the magnet and the three T-stations T1, T2 and T3 between the magnet and the RICH2. The T-stations consist of the Inner Tracker, covering the area around the beam pipe, and the Outer Tracker covering the

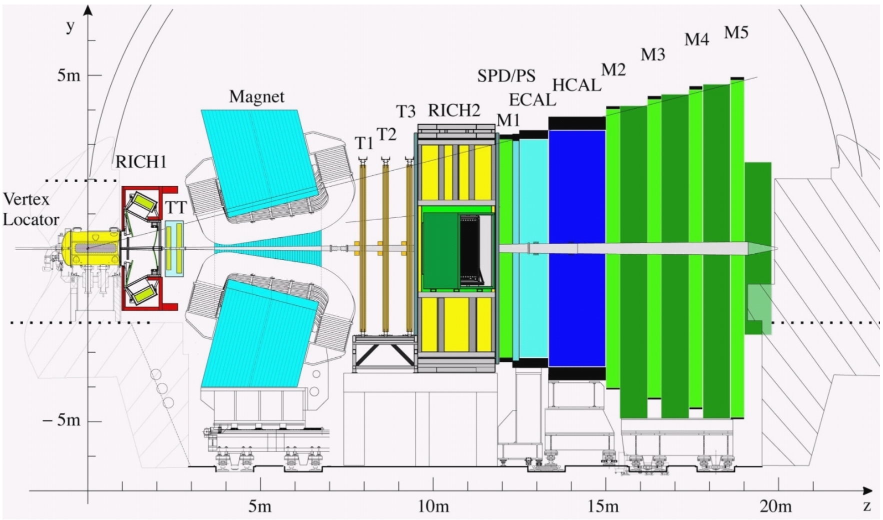

Figure 2.6: View of the LHCb detector in the y-z plane

rest of the acceptance. The reason to divide the stations into two different subdetectors is the large occupancy for detector areas close to the beam pipe. While the VELO, TT and IT are silicon micro-strip detectors, the OT is a straw tube detector. In contrast to the OT tubes which are more than 2 m long, the silicon strip detectors have short strips, which are up to about 40 cm long, allowing to cope better with high occupancy. In addition the silicon micro-strip detectors have a fine strip pitch of about 200 μm, compared to the OT straw tube with a straw pitch of 5 mm.

2.5.1 The Vertex Locator

The Vertex Locator [25, 26] is the tracking subdetector located around the interaction point (see Fig. 2.6). The VELO is designed to measure vertices to a very high accuracy. Due to the lifetime of the B meson, particles coming from the B decay can be selected requiring some distance to the primary vertex, i.e. the proton-proton collision. Therefore, the VELO needs to have a very good vertex resolution. The error on the extrapolated track at a given position depends on its distance to the closest measurement. Thus, a good resolution implies obtaining hits as close to the beam as possible.

The VELO has 21 stations along the beam axis. Figure 2.7 shows a sketch of the arrangement of the 21 stations. Every station consists of two modules, mounted perpendicular to the beam on the A-side and on the C-side. The module itself is a combination of two 300 μm thick silicon sensors, one r and one ϕ-sensor, glued together back-to-back. The setup allows to reconstruct tracks with polar angles starting from 390 mrad down to 15 mrad.

The layout of the two different types of sensors is shown in Fig. 2.8. The sensors

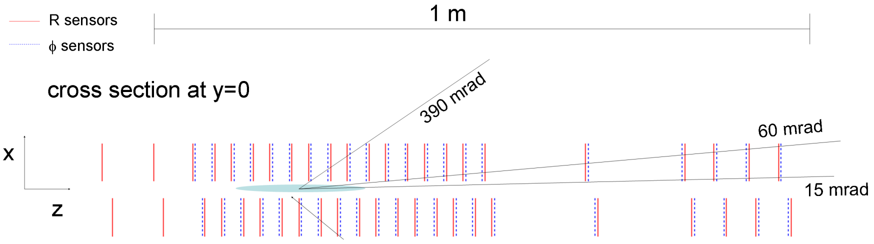

Figure 2.7: Top view of the VELO in the x-z plane. The interaction region shaded in grey is at $y = 0$.

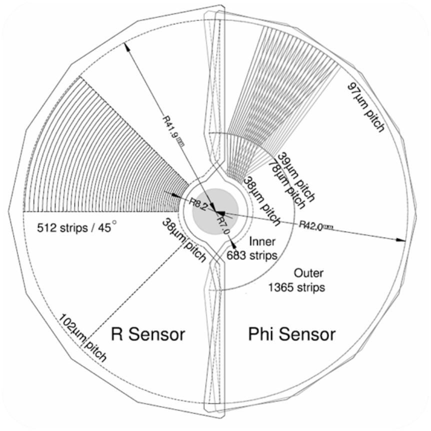

Figure 2.8: The VELO r and ϕ sensors.

have the shape of half discs with an inner active area radius of 8.17 mm. The outer active area radius measures 42 mm. The half-discs have an angular coverage of 182° to guarantee overlaps between the A- and C-side modules. The r-sensors have circular strips with a strip pitch growing linearly from 40 μm for the smallest radius to 101.6 μm for the largest radius. The ϕ-sensors measure the azimuthal angle. The strip is a straight line with a kink, having a stereo angle with respect to the radial of 20° for the inner region and -10° for the outer region. For the inner region the strip pitch grows from 35.5 μm to 78.3 μm and for the outer region the pitch grows from 39.3 μm to 96.6 μm. The modules are alternately mounted on the station, one time the r-sensor facing the RICH1 and then the ϕ-sensor facing the RICH1.

During the fills of the LHC the beam size is too large and the beam conditions are not stable enough to allow for sensors being 8 mm close to the beam. To avoid any severe damage by the beam, the two halves are retracted by 3 cm horizontally as shown in Fig. 2.9. As soon the beam reaches stable running conditions, the VELO station are moved in to 8 mm from the beam, making the VELO to be the detector having sensors the closest to the beam among all the experiments located at LHC.

VELO fully closed
(stable beam)

VELO fully open

Figure 2.9: View of the VELO in the x-y plane in the closed mode during data taking and in the open mode during the beam filling.

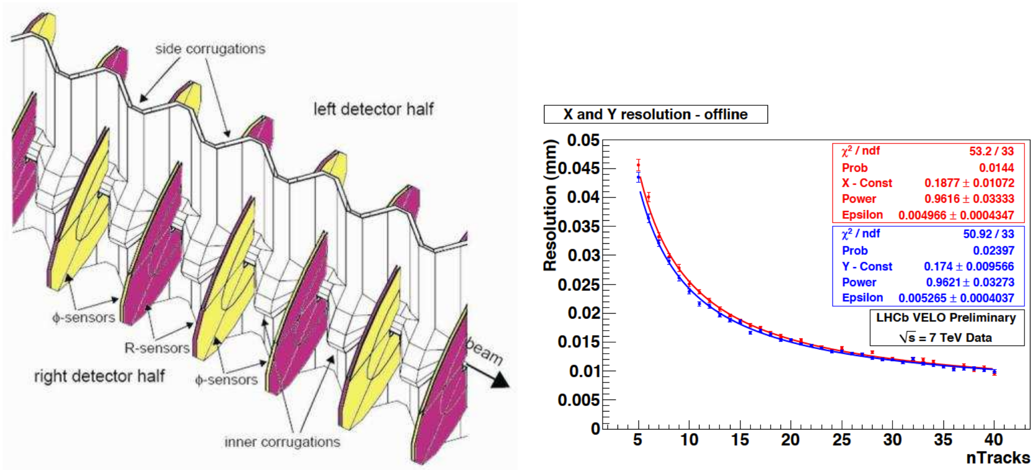

(a) (b)

Figure 2.10: Close up view of some sensors and the RF-foil (a). The LHCb primary vertex resolution (x red, y blue) as a function of the track multiplicity (b).

To allow to place the VELO sensors that close to the beam, the sensors are located in a vacuum tank which is bonded to the beam pipe. To protect the beam vacuum, a thin aluminium foil separates the vacuum where the sensors are located from the beam vacuum. Additionally, the foil shields the VELO readout electronics from radio-frequent (RF) noise caused by the beam. Figure 2.10 shows a close up of a few sensors and the RF foil.

The primary vertex resolution of the VELO is found to be 16 μm in the x and y coordinate and 76 μm in the z coordinate for a vertex with 25 tracks [27] (see Fig. 2.10).

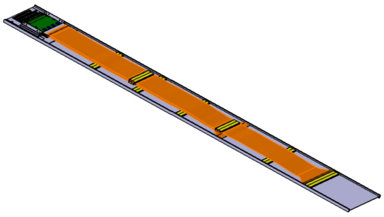

Figure 2.11: A TT half-module consisting of 7 silicon sensors.

2.5.2 The Tracker Turicensis

The Tracker Turicensis [25, 28] is located between the RICH1 and the magnet (see Fig. 2.6). Although the TT lost its original function, it still provides important information. For example, TT hits do improve the momentum resolution considerably. Furthermore, TT hits are used to reconstruct tracks of particles that decay outside the VELO. The Tracker Turicensis has four layers along the z direction, where the first two and the last two are grouped into the stations TTa and TTb. Every station has one X-layer with vertical strips followed by, a stereo layer with a stereo angle, $+5°$ for TTaU and -5° for TTbV. The TTaX layer is facing the RICH1 and the TTbX layer faces the magnet, i.e. it is rotated by 180° around the y coordinate with respect to the TTa station. That means that the two stereo layers are located between the two X-layers.

The TTa layers are composed of 30 half-modules, the TTb layers of 34. Every half-module consists of 7 silicon sensors mounted to a ladder as shown in Fig. 2.11. Two half-modules are combined to a full module, which gets mounted vertically in the X-layer or with the corresponding stereo angle for the U or V layer. For the modules at $x = 0$, i.e. the module at the x coordinate where the beam pipe goes through the TT station, no full module can be mounted. In each layer, two half-modules are positioned above and below the beam pipe, referred as top and bottom modules. Figure 2.12 shows the TTaX and TTbV layer. Every square designates a sensor. To avoid any insensitive area in a single layer, one has to make sure that the projection of all the sensitive areas of the sensors on the x-y plane has no gaps. That means, that sensors have to be arranged within a layer that way, that looking in z direction, the sensors overlap. To allow for such overlaps the modules are staggered in z. As the average track conditions change over the area of the TT, the dimensions of the overlaps have to be adapted according to the track slope. The staggering of the module is shown in Fig. 2.13 [28].

The sensors used for the TT modules have a thickness of 500 μm and a pitch width of 183 μm. The active area has a height of 91.6 mm and a width of 93.906 mm. As the active area does not cover the full area of the silicon sensor, the arrangement of the sensors to half-modules and the combination of two half-modules to a full module causes some horizontal sensitivity gaps within a module. The resolution of the Tracker Turicensis is about 55 μm [27].

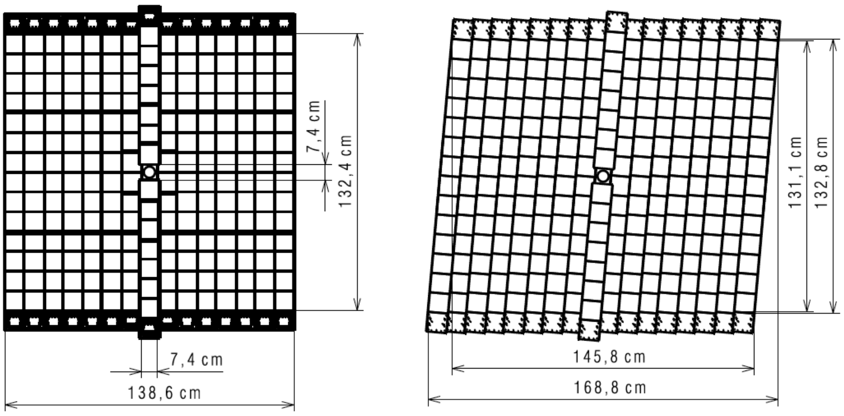

(a) (b)

Figure 2.12: The TTaX layer (a) with vertical strips and the TTbV layer (b) with a stereo angle of -5°.

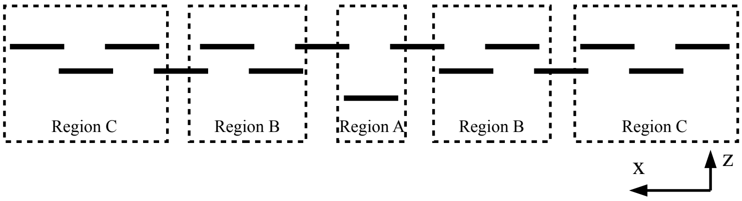

Figure 2.13: The staggering of the TT modules of the TTaX layer in the x-z plane [28]. Every black solid line denotes a module, except the one in the very centre in region A, that shows the two half-modules above and below the beam pipe . The staggering allows for overlaps of the sensitive areas of adjacent modules. The overlapping region in the x coordinate varies from 9.5 mm (region A), over 3.5 mm (region B) to 4.5 mm (region C). The distances are not to scale.

2.5.3 The Inner Tracker

The Inner Tracker [19, 29] is part of the three T-stations T1, T2 and T3, located between the magnet and the RICH2 (see Fig. 2.6). Each of the IT stations consists of four boxes mounted around the beam pipe and named after their position with respect to the beam pipe (top, bottom, A-side, C-side). Every detector box has four layers and, as the TT, contains two X-layers with vertical strips in the front and in the back, and two stereo layers in between, with stereo angles +5° (U-layer) and -5° (V-layer). The modules built into the top and bottom modules consist of only one sensor, whereas

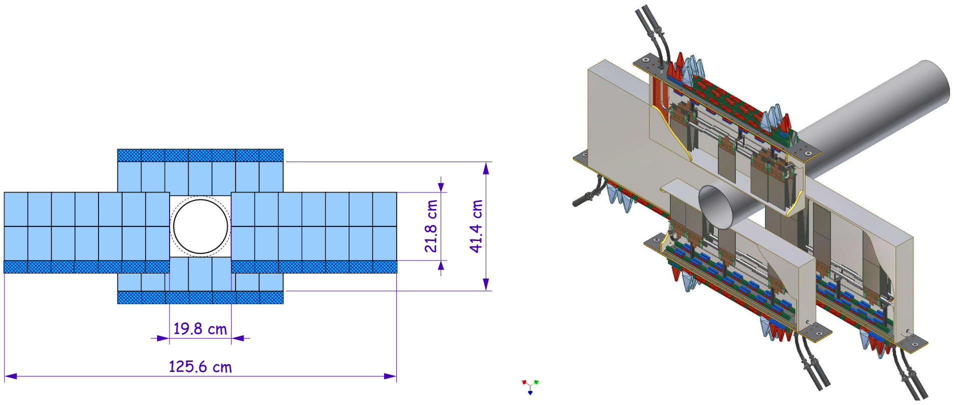

(a) (b)

Figure 2.14: Sensor arrangement in one of the the IT X-layer in the second T-station (a). Light blue marks the sensors and dark blue the readout electronic. The setup of the four IT boxes within a T-station (b).

the modules used for the A- and C-side boxes comprise two sensors (see Fig. 2.14). The IT modules are built up of 320 μm and 420 μm thick sensors with a pitch width of 198 μm. Similar to the TT, the modules within a layer are staggered in z to avoid non-sensitive gaps between adjacent modules. As the modules in the A- and C-side consist of two sensors, some dead area between the sensors cannot be avoided. The similar design of the IT and TT lead to a similar resolution of about 55 μm [27].

2.5.4 The Outer Tracker

The Outer Tracker [19, 24, 30] covers the largest part of the LHCb acceptance in the three T-stations (see Fig. 2.17). In contrast to the silicon strip detectors VELO, TT and IT, the OT is a straw tube detector. The detector exploits the fact, that particles traveling through a gas ionise the molecules. Anode and cathode of the tube are arranged such, that electrons do not recombine with the ions and drift towards the anode (see Fig. 2.15 and Ref. [31]). The accelerated electrons ionise further molecules causing an electron shower, and thus a signal that can be measured.

Each of the OT stations has four layers. Within a station, the OT has the same X-U-V-X layer structure as the TT and the IT. The X-layers have a vertical orientation, whereas the U and V-layer have a stereo angle of ± 5°. The layers are divided into an A- and a C-side. The OT modules are placed within a so-called C-frame on each side. In total, an OT layer is composed of 22 OT modules, 14 full modules (F-modules) and 8 short modules (S-module). The short modules have approximately half the length of a full module. They are subdivided into three categories, S1-, S2- and S3-modules.

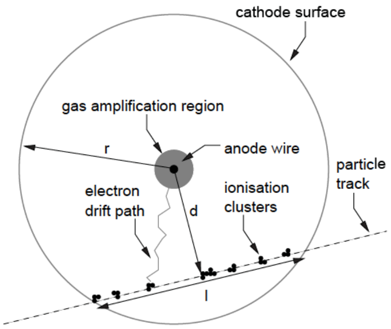

Figure 2.15: Functionality of a straw tube detector.

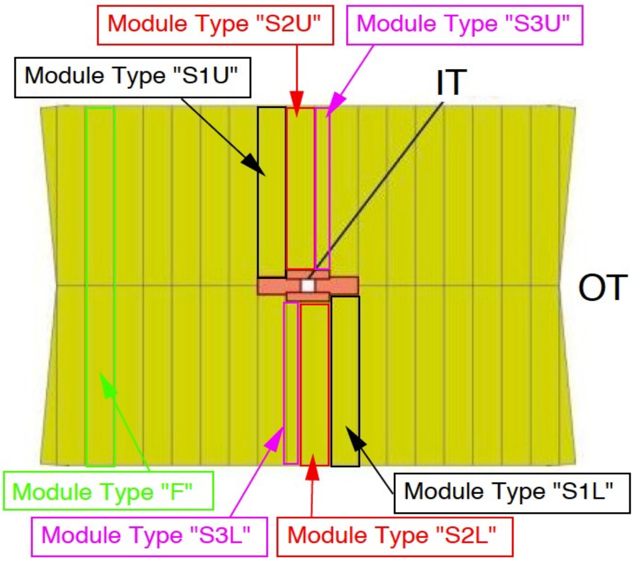

Figure 2.16: The position of the different OT module types [32].

Figure 2.16 shows the positions of the different OT module types. The short modules are used to cover the acceptance above and below the IT boxes.

All modules have 128 tubes arranged in two staggered monolayers of 64 tubes as shown in Fig. 2.18, except the S3-modules with only 64 tubes in total because of their half width. The tubes of the F-modules are split into two around $y = 0$ to avoid too large occupancy. To prevent insensitive areas within a layer, the split of the tube in the two monolayers is staggered in the y coordinate. The dimensions of a module are given in Fig. 2.18. The spatial resolution of the Outer Tracker is measured to be about 250 μm [27].

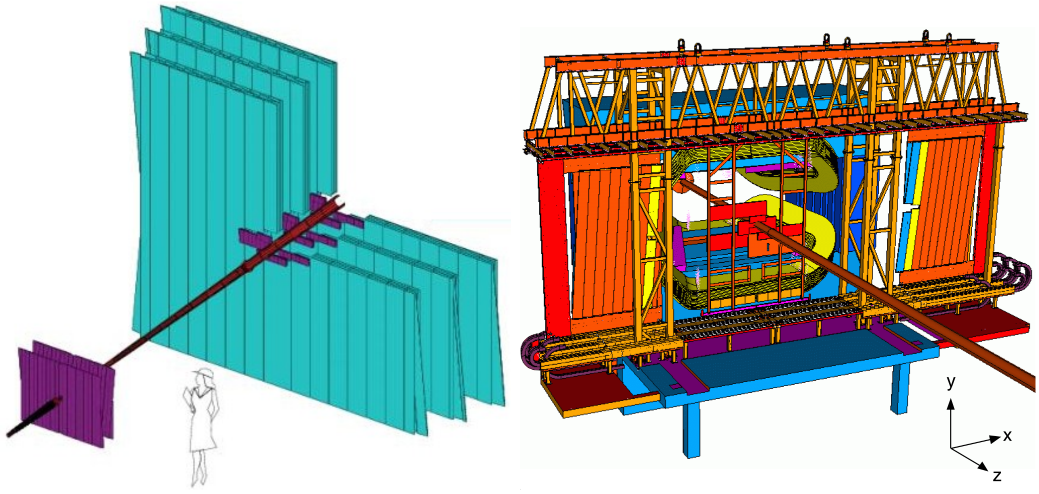

(a) (b)

Figure 2.17: The arrangement (a) of the OT (turquoise) and the IT and TT (purple). The OT modules installed in the C-frames in the opened position (b). One can see as well the IT boxes around the beam pipe.

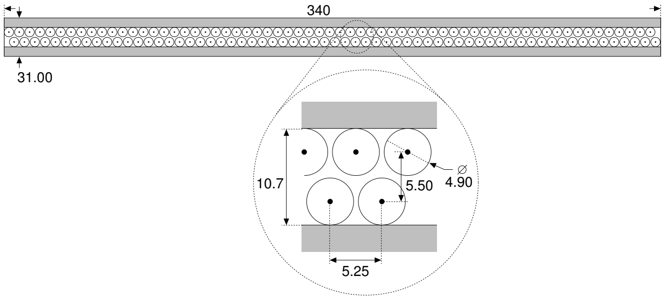

Figure 2.18: The OT module cross section in the x-z plane.

2.6 Particle identification

The identification of hadrons is basically done in the RICH1 and in the RICH2, upstream and downstream of the magnet, and the hadronic calorimeter, which in addition gives information about the hadron energy, positioned right in front of the second muon station M2. The electromagnetic calorimeter located in front of the hadronic calorimeter provides particulars about electrons and photons. Finally, the muon stations M1-M5 at the end of the detector identify muons.

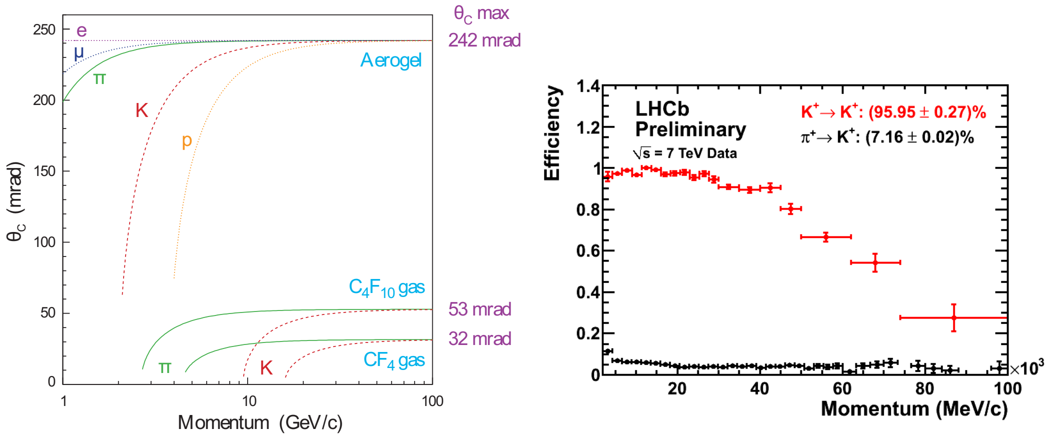

(a) (b)

Figure 2.19: Particle momentum versus Cherenkov angle (a). The particle identification probability (b) for the kaon (red) and the pion misidentification probability of the pion (black) to be identified as kaon.

2.6.1 The ring imaging Cherenkov detectors

LHCb comes with two Rich Imaging Cherenkov detectors RICH1 and RICH2 [24, 25, 33]. RICH1 covers the full acceptance range and is responsible to identify lower momentum particles. Particles with larger momentum are supposed to be identified by RICH2, which covers an angular acceptance region of 120 mrad horizontally and 100 mrad vertically. The combination of both RICH systems allows to identify particles in a momentum range of 2-100 GeV. As the name of the subdetector anticipates, the RICH exploits the Cherenkov effect. In vacuum the speed of light c is the absolute limit on velocity. In a medium however, the speed of light is reduced making it possible, that particles are traveling faster than the actual speed of light in this medium. Particles doing so emit light under a specific angle given by

$$cos(\theta_C) = \frac{1}{\beta n} \ , \tag{2.4}$$

where θ_C is the angle, n the index of refraction and β the velocity, given by $\beta = \frac{v}{c}$ in vacuum. Knowing the emitting light angle and the particle momentum the particle can be clearly identified. Figure 2.19 shows the particle momentum versus the Cherenkov angle. The aerogel and the C_4F_{10} in RICH1 cover the low momentum region of 2-60 GeV and the CF_4 in RICH2 covers the high momentum region of 15-100 GeV.

2.6.2 Electromagnetic and hadronic calorimeter

The electromagnetic and hadronic calorimeter [19, 34] provide information about the position, identity and energy of electrons, photons and hadrons. The ECAL and then the HCAL are placed between the first and the second muon station. As the calorimeters themselves can not distinguish between charged and uncharged particles, an other layer is added just in front of the ECAL, the scintillator pad detector (SPD). The SPD helps to select charged particles. An additional scintillator called PS (preshower detector) placed between the SPD and the ECAL helps do distinguish charge hadrons from electrons. All components of the calorimeter system follow the same basic principal. Particles going through the calorimeter are absorbed and cause a shower of particles. The particles again excite the scintillating material in the detector. These excited states falling back into their ground state emit light which is transmitted to a photomultiplier tube (PMT). The signal measured by the PMT is proportional to the energy of the particle at the beginning of the causal chain.

The calorimeter system has a vertical and horizontal segmentation. The size of the cell depends on whether it is located in an area with high particle flux or not. The regions with high pseudo rapidity[2] have a large hit density. The size of the square cells vary from about 40 mm in the high flux region to about 263 mm in the low flux region.

2.6.3 The muon system

The muon stations [24, 35, 36, 37] are located in the back of the experiment. Triggering events on muons is a fundamental requirement of the LHCb experiment, as many decays of interest can be easily selected via the muons. The muon stations M1 to M3 have a high spatial resolution in the bending plane (x coordinate) providing p_T information to the trigger. The first muon station is placed upstream of the calorimeter to improve the precision of the muon trigger. The stations M2-M5 are placed in the very back of LHCb. Between the muon stations 80 cm thick iron absorbers only allow muons to pass the stations. The stations M4 and M5 have a comparatively poor x coordinate resolution. They mainly perform the muon identification.

The muon stations mainly consist of multi-wire proportional chambers (MWPC). Figure 2.20 shows a sketch of such a chamber. An array of wires is located in a gas filled volume. Analogue to the straw tubes in the OT, muons traversing the gas volume ionise the gas molecules and the electrical field applied between the wires and the volume walls accelerates the ions causing an electron shower that can be detected. The wires are placed vertically along the y direction giving a spatial resolution in x. The wires have a pitch of 2 mm. The coarse segmentation of the cathode pads in y gives some spatial resolution in y.

---

[2] pseudo-rapidity $\eta = -\ln\left(\tan\frac{\theta}{2}\right)$ where θ is the azimuthal angle

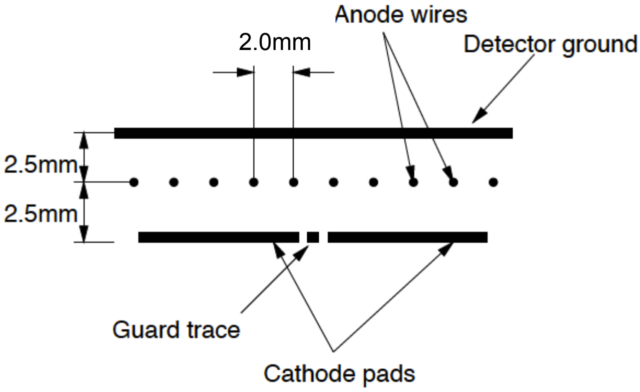

Figure 2.20: Schematic diagram of a multi-wire proportional chamber.

Due to high particle rates in the central region of the first muon station M1, this part of the muon system is based on gas electron multipliers, in this case so called triple-GEM detectors. An insulator with specific geometrical shape is placed between an anode and a cathode such that strong electric fields are generated. Again, muons ionising the gas will cause a cascade of charged particles that can be detected. This type of detector is built with a smaller segmentation than the MWPC allowing them to cope better with the high particle density.

2.7 The magnet

The magnet [24, 38] is located between the TT and T-stations. It is a warm dipole magnet and consists of two conical saddle-shaped aluminium coils arranged in a iron yoke. The main magnetic field component points along the y axis either in positive or negative direction. The integrated magnetic field for a particle traversing the magnet is about 4 Tm. Figure 2.21 shows the LHCb magnet. The picture was taken at a time where most of the other parts of the LHCb detector were not yet installed.

2.8 Trigger

The designed proton-proton collision rate is 40 MHz. Only a fraction of all the events would be of interest to a physics analysis. Writing all the events to storage would be very inefficient in terms of computing power and storage and is simply not feasible. The aim of the trigger is to select those events that look promising and reduce the rate at which the events are written to storage to a reasonable level. The trigger comprises two levels, the L0 (level zero) trigger and the HLT (high level trigger) [24]. The high level trigger is divided into the HLT1 and HLT2. Events passing the hardware-based

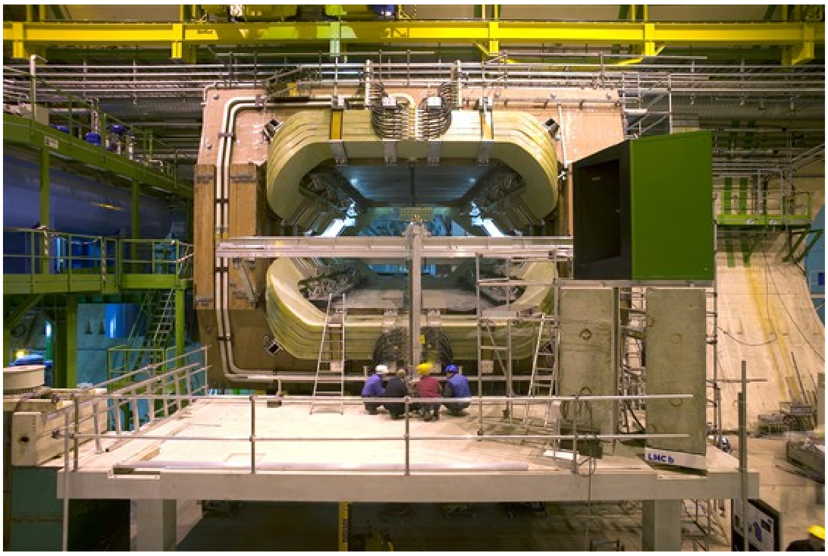

Figure 2.21: The LHCb magnet seen from the back looking upstream (© CERN).

L0 trigger are fed to the software-based HLT. Events passing the first high level and subsequently the second high level trigger are written to tape.

The L0 trigger reduces the beam crossing rate of 40 MHz to the level of 1 MHz, where the full LHCb detector can be read out. The data objects used by the L0 trigger have to be read out at the bunch crossing rate of 40 MHz. The characteristic of B events is the presence of high-p_T particles. Therefore the trigger looks at the largest transverse energy deposited in the hadronic calorimeter, at the highest deposited transverse energy in the electromagnetic calorimeter and the highest transverse momenta belonging to a single muon or a muon pair. If one of the three contribution is over a certain threshold the event is selected.

The HLT1 and HLT2 already exploit the combination of information from different subdetectors. The output rate of HLT1 is up to 50 kHz. To select decays including two muons in the final state, the HLT1 requires either one or two reconstructed muons. This selection already uses reconstructed particles. If two muons are found, the invariant mass of the di-muon system is calculated. The events are selected if they pass given criteria. The muon lines have a output rate of about 5 kHz.

As the HLT2 operates at a comparatively low rate many more variables can be used to reject or select an event. The selection requirements for HLT2 are determined using multivariate analysis techniques. At this point one has to make sure that this computer driven selection does not affect the physics to be investigated. The output rate of the HLT2 goes up to 3 kHz.

Chapter 3

Detector description and survey

Many physics analyses get input from studies performed on simulated data. The simulation depends on the description of the detector in the software. Therefore a detailed description of the actual detector is crucial. Almost every part in the acceptance of the LHCb detector is modelled in the simulation software. The simulation software uses this description to compute the interaction of each of the simulated particles with the detector material and to determine the location of the signals in the various sensitive detector areas. In this chapter a short overview of the framework managing the detector description data will be given. Secondly, the geometrical description of the Tracker Turicensis will be covered. Finally, the survey of the Tracker Turicensis and the implementation of this data as alignment parameters into the alignment database will be discussed.

3.1 Detector description

The detector description is one of the central parts of the LHCb software. The detector description framework stores, accesses and processes all data related to the description of the detector and provides the necessary information to algorithms requiring detector information such as the simulation and the reconstruction software. The detector description framework is integrated into the Gaudi framework [39, 40, 41]. The Gaudi framework covers all the tasks needed for event data processing at LHCb. All algorithms are embedded in this framework.

3.1.1 The framework

The geometry framework is split into three parts as depicted in Fig. 3.1:

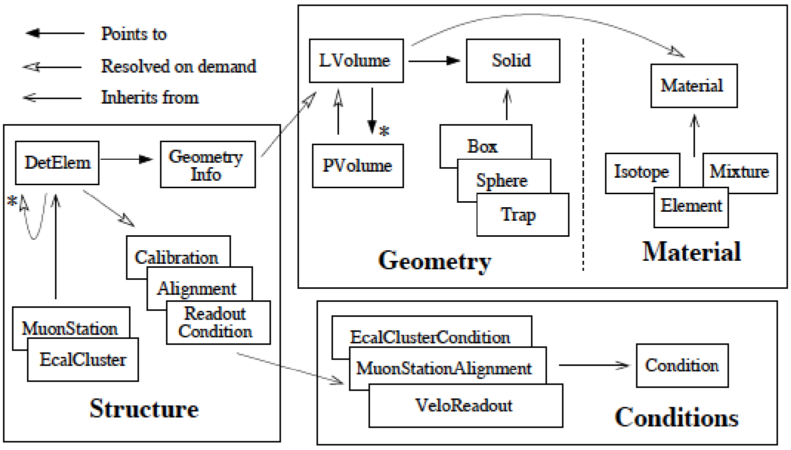

Figure 3.1: Pictogram of the detector description framework [42]. Central relevance has the detector element (DetElem) that is stored in the structure. Information from the geometry and the conditions can be accessed via the detector element.

- **Structure**
  The structure is a tree of detector elements describing the setup of all the different detector components. All information from the geometry or the conditions can be accessed via detector elements. The structure builds the basic of the detector description database (DDDB).
- **Geometry and Materials**
  This part describes the detector geometry by a hierarchy of *logical* and *physical* volumes, where *logical* volumes are unplaced volumes containing information about the shape and material of a data object. A *physical* volume is a positioned *logical* volume inside an other *logical* volume. A *physical* volume has a defined position within the coordinate system of its parent.
  Every volume has an allocated material which is stored in this part. Materials can be chemical elements, isotopes or mixtures, where a mixture can be built up of mixtures again. The composition of a mixture is given by the fraction of the component materials. The information about the detector geometry is stored in the detector description database.

- **Detector Conditions**
  Conditions are objects which are version or time dependent. Some parts of the detector description may change over time and have different values for a given version and time. Typical condition objects are the calibration parameters and the alignment parameters of detector elements.

One feature of the framework has to be highlighted at this point. Queries to the detector description, like determining the intersection points of a particle's trajectory with the physical volumes, require a search through the whole detector description tree. Grouping detector objects in virtual mother volumes can speed up the search through the detector description tree. These volumes have to be kept simple in shape (e.g. a box or a sphere) to keep the gain in search time.

In the Gaudi framework transient representations of data objects are separated from the persistent representations. This also applies to all the detector-describing data objects. Figure 3.2 shows an overview how Gaudi algorithms access detector informations through a transient detector store and how this is populated from the detector description database (DDDB). The *DetectorDataService* makes sure that the transient store is up to date.

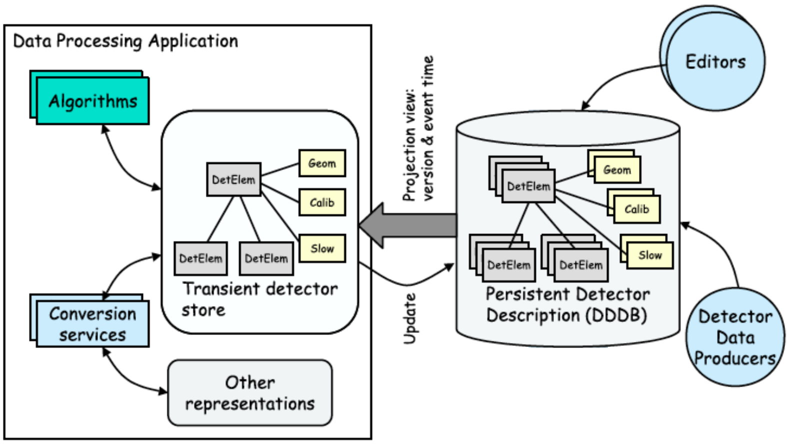

Figure 3.2: Scheme of how algorithms access information about the detector via the transient detector store [43]. The transient detector description is generated from the persistent detector description for a given version and event time.

The persistent storage of detector data is provided in the Extensible Markup Language (XML). The main reason for choosing XML is the ease of use and the large number of tools existing for its manipulation and parsing. Tools like XLST processor makes it easy to translate XML into other formats. More detailed information about the detector description and its framework can be found in Refs. [42] and [43] .

3.1.2 TT geometry and its detector description

The design of the Tracker Turicensis was finalised in 2004 [28]. Large efforts were made to produce a precise detector description. The material budget of the TT was calculated [44] and a detector description was written [45]. The description was modified and updated afterwards and offsets measured in the surveys were implemented in the alignment database (see Ref. [46]). This section lists the key features implemented in the detector description.

One of the main features in the description of the TT detector is the concept of virtual mother volumes. As mentioned in section 3.1.1 they are added to speed up the search through the detector description hierarchy tree. Volumes are added to group the modules on the access and cryo side of the detector for each of the four layers in the TT. The detailed description of the TT half-modules results in a large number of volumes. Adding a virtual mother volume for each of the modules comprising all the volumes related to the half-module improves the search through the large number of volumes. However, because of the staggering of the TT modules, the rails on each side of the module holding the sensors can not be included into this mother volume, as this would lead to overlaps of mother volumes. Figure 3.3 (a) shows a half-module with all its details. An important test after adding new volumes is the search for such overlapping volumes. In case a particle passes through overlapping volumes, the location, material and conditions would be ambiguous, causing the software to crash. Where needed, a clearance of 0.1 mm is introduced for mother volumes to prevent overlaps. The location and size of the physical volumes all remain unaffected. Simplifying the detector description by merging multiple volumes into one volume is an other possibility to make the search through the hierarchy tree more efficient. This might lead to overlaps and consequently to other simplifications. The hybrids of the half-modules are not incorporated into the detector description to avoid overlaps with the simplified volumes of the balconies and because they are located outside the acceptance region.

In the following the most important elements of the TT geometry will be described.

- **Module**
  - Each sensor within a module is put into the description. As the exact position of the sensors has been monitored using a metrology machine during assembly this gives the possibility to position and align single sensors.
  - The Kapton cables are modelled for every single module. The density of the cables is determined from their measured mass and the material of the

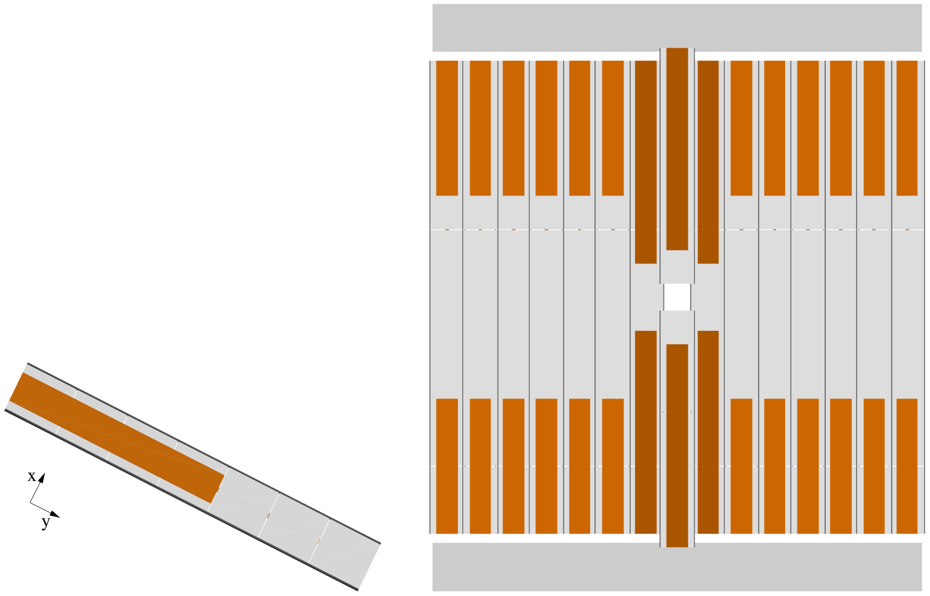

(a) (b)

Figure 3.3: A half-module (a) and the TTaX layer (b) as seen by the LHCb visualisation software. The coordinate system in (a) shows the local frame orientation.

  Kevlar caps is averaged over the cable volume to keep the number of volumes low.

  - The different orientations of the modules are taken into account. The modules of the TTa layer have the silicon strips facing the VELO, whereas the silicon strips of the TTb layer are facing the magnet. This guarantees that the alignment software knows about the correct local coordinate system within the module.
  - The modules are positioned using the same numbers as the technical drawings. Furthermore, the x dimension of the overlap region has the same value as the technical design.
  - A gap is introduced between the half-modules that are combined to one full module. This gap is measured to be 0.3 mm.

- **Beam pipe isolation**
  The part of the TT with the highest occupancy is the region around the beam pipe hole. The beam pipe insulation adds material exactly in this region. Therefore, big efforts have been made to model the beam pipe isolation as realistically as possible. The mass has been determined by putting it on a balance. The average

density is found to be 0.183 g/cm^3. A view of the the implemented beam pipe insulation is shown in Fig. 3.4. The beam pipe insulation covers the beam pipe over the full z-length in the TT. The description resigns to add the material at the z position of the four TT layers for simplicity reasons.

- **Sensor strip pitch**
  The strip pitch of the silicon strip sensors described in the module structure parameter files is set to the design value of 183 μm.
- **Balconies**
  The individual balconies for each module are merged into one simplified volume for each layer. The y dimension of the volumes is given by the height of the balconies. The length in the x coordinate reaches from the outer edge of the outermost balcony on the A side to the outer edge of the outermost balcony on the C side. The thickness is determined by averaging the total mass of all the balconies involved in the volume over the given x–y dimensions.
- **Cooling plates**
  The balconies are mounted on four cooling plates, two on top and tow on bottom. The two cooling plates on top and bottom are merged into one simplified volume in the detector description. Adding a further volume in the detector description on each side of the TT box accounts for the additional cooling elements in the TT.

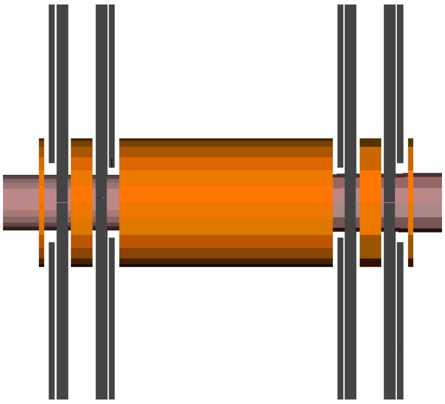

Figure 3.4: View of the beam pipe insulation (orange) in the y–z plane. One can see as well the beam pipe (horizontal) and the four TT layers (vertical).

In order to see the impact of the TT geometry in the detector description the material budget is evaluated. Scans are made that determine the amount of material a particle sees traversing the detector in a straight line. The amount of material is calculated in fractions of a radiation length. The scans are done in a x–y or in a η–ϕ projection, where η is the pseudo-rapidity and ϕ the azimuthal angle. The scan for the x versus y and the ϕ versus η plane can be seen in Fig. 3.5. Figure 3.6 shows the radiation length averaged over ϕ, as a function of η.

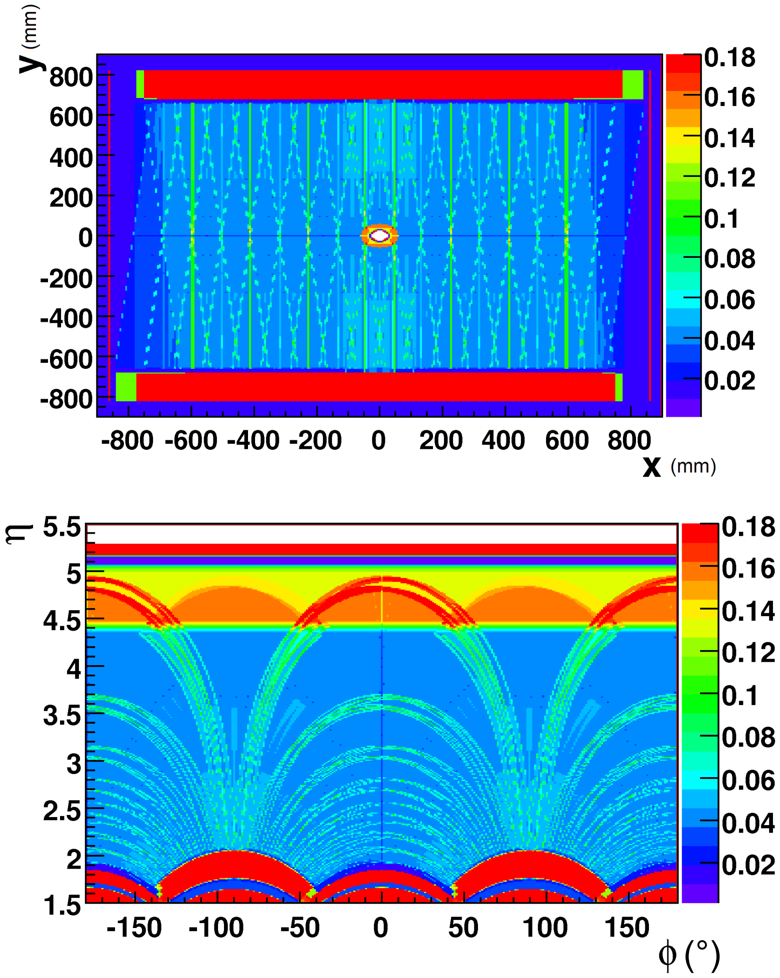

Figure 3.5: Material scan of x versus y (top) and ϕ versus η (bottom) in fraction of a radiation length.

Some details implemented in the detector description can easily be seen. At $y = 0$ in Fig. 3.5 one can see less material over the full x range of the TT. This is related to the gap between the two half-modules that form together a full module. Further on, the Kapton cables can be seen. The additional Kapton cable for the innermost sensors in the KLM-module can clearly be seen for the modules located around the beam pipe hole. The two simplified volumes accounting for the cooling elements on both sides of the TT can be seen as vertical red lines at $|x| > 800$ mm.

In Fig. 3.6, at low pseudo-rapidity value one can see the cooling plates. The material seen between $4.4 < \eta < 5.1$ comes from the beam pipe insulation. The spike at $\eta > 5.2$ is the contribution from the beam pipe, which consists of a cylindrical section and

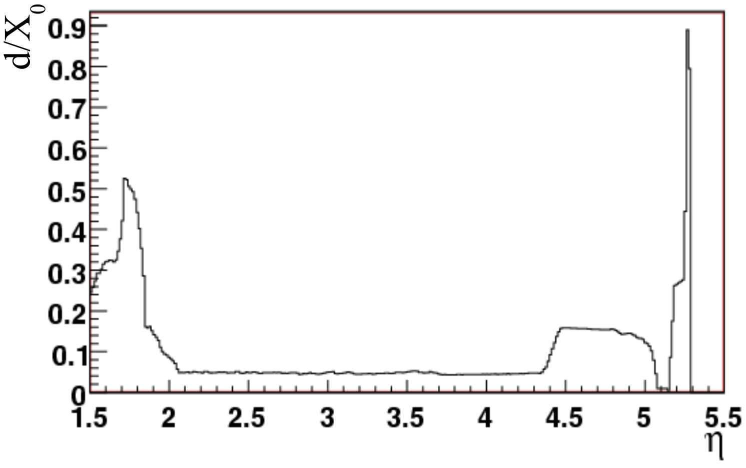

Figure 3.6: Thickness d of the TT in radiation length X_0 averaged over ϕ, as a function of η. The LHCb acceptance covers $1.8 < \eta < 4.9$. The large radiation length at $\eta < 2$ is caused by the cooling plates. Between $4.4 < \eta < 5.1$ one can see the effect of the beam pipe insulation. The spike at $\eta > 5.1$ is related to the beam pipe.

a 10 mrad conical section.

3.2 Optical survey of the TT

Before, during and after the installation the components of the TT detector were carefully surveyed. A half-module metrology after the assembly measured the relative position of the sensors to each other. The survey of the balconies was done using photogrammetry. In addition an optical survey of the full TT station was performed, measuring the global position of the TT detector in the cavern coordinate system. Further studies were done while the magnet was switched on, measuring the impact of the presence of the magnetic field to the TT position.

3.2.1 Metrology and photogrammetry

To classify the half-modules they have undergone a metrology in the lab in Zürich [47]. The position and the rotation of every sensor within a module is measured with respect to a line determined by the average of the seven sensors. Unfortunately there is no measurement that gives the relative position of the sensors to the positioning holes in the ceramic of the hybrid. Nevertheless, the average position of all sensors is used as a measure for the positions of the hybrid. The measurements from the sensor metrology are transformed into the local coordinate system and transformed to the XML format readable to the alignment algorithm.

Photogrammetry is a technique that uses pictures made by a camera to reconstruct a 3D profile of a given object. The position is calculated via triangulation. At least two pictures of the object are needed to be able to reconstruct an object in all three dimensions. More than two pictures increase the precision of the measurement. Several pictures were made for every measurement. The precision of the position depends on a clear differentiation between the point to measure and the background. Therefore retro-reflective targets as shown in Fig. 3.7 were placed on the detector.

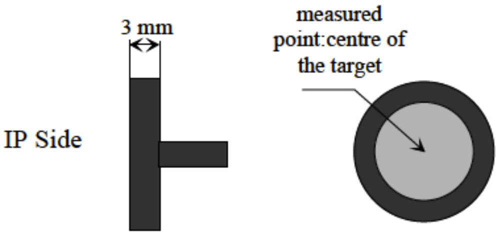

Figure 3.7: Design of the retro-reflective targets used for the photogrammetry.

The survey contains measurements of the location of the balconies. The position of the balconies is measured with respect to the outside of the insulation box. In combination with a survey of the TT detector box the position of the balconies in the global LHCb coordinate system can be determined. For the measurement of the TT box, the targets can directly be mounted on the positioning holes for the box insulation wall. Whereas for the balconies the targets have to be mounted on special target adapters as shown in Fig. 3.8. The adapters holding the targets were mounted on the balconies. The photogrammetry was performed before the installation of the modules. To place the modules at the designed position each balcony has two precision pins. These pins were also used to position the adapters onto the balconies. The photogrammetry method has an intrinsic resolution of 50 μm of the target. The four targets on the adapter allow to reconstruct the position of the two pins, which determines the position of the module.

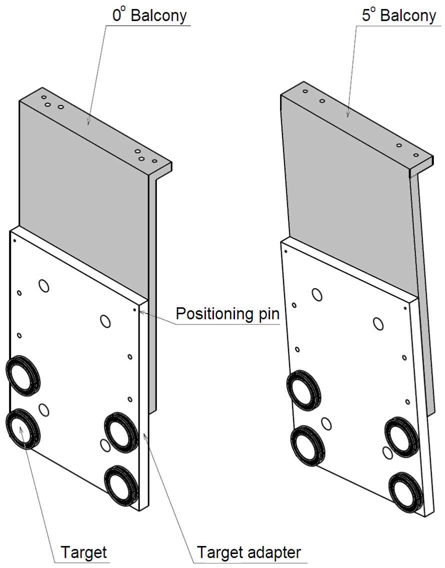

Figure 3.8: Target adapters mounted on balconies for straight (left) and stereo (right) layers. The balconies are drawn in grey, the adapters in white.

3.2.2 Implementation of the survey measurements

The calculated position of the precisions pins is compared to the nominal position of the pins in the design. The offsets are shown in Fig. 3.9 for the A side and in Fig. 3.10 for the C side balconies.

There are two cutouts in the ceramic of the hybrid that allow to position the module. The first cutout has the shape of a triangle, the second of a square. The cutouts in the ceramic can be seen in Fig. 3.11. On the top hybrid of a full module, only the pins matching the triangular cutouts are used, on the lower hybrid only the square cutout ares used. The upper pin defines the x-y position of the module. The z position is given by the surface of the upper balcony. The upper pin also defines the pivot point of a full module. The rotation around the x and z axis are given by the pin matching the square cutout on the lower hybrid. For the half-modules on top and bottom of the beam pipe, both pins are used to determine all these values. The offsets and rotation determined this way are transformed into XML format such that they can be used as input to the alignment procedure.

All the information gained out of the surveys are used as input to the alignment defining the starting point of all the alignment parameters used in the algorithm. The following chapter will treat this topic in more details.

The TT has undergone several additional surveys to check the global position of

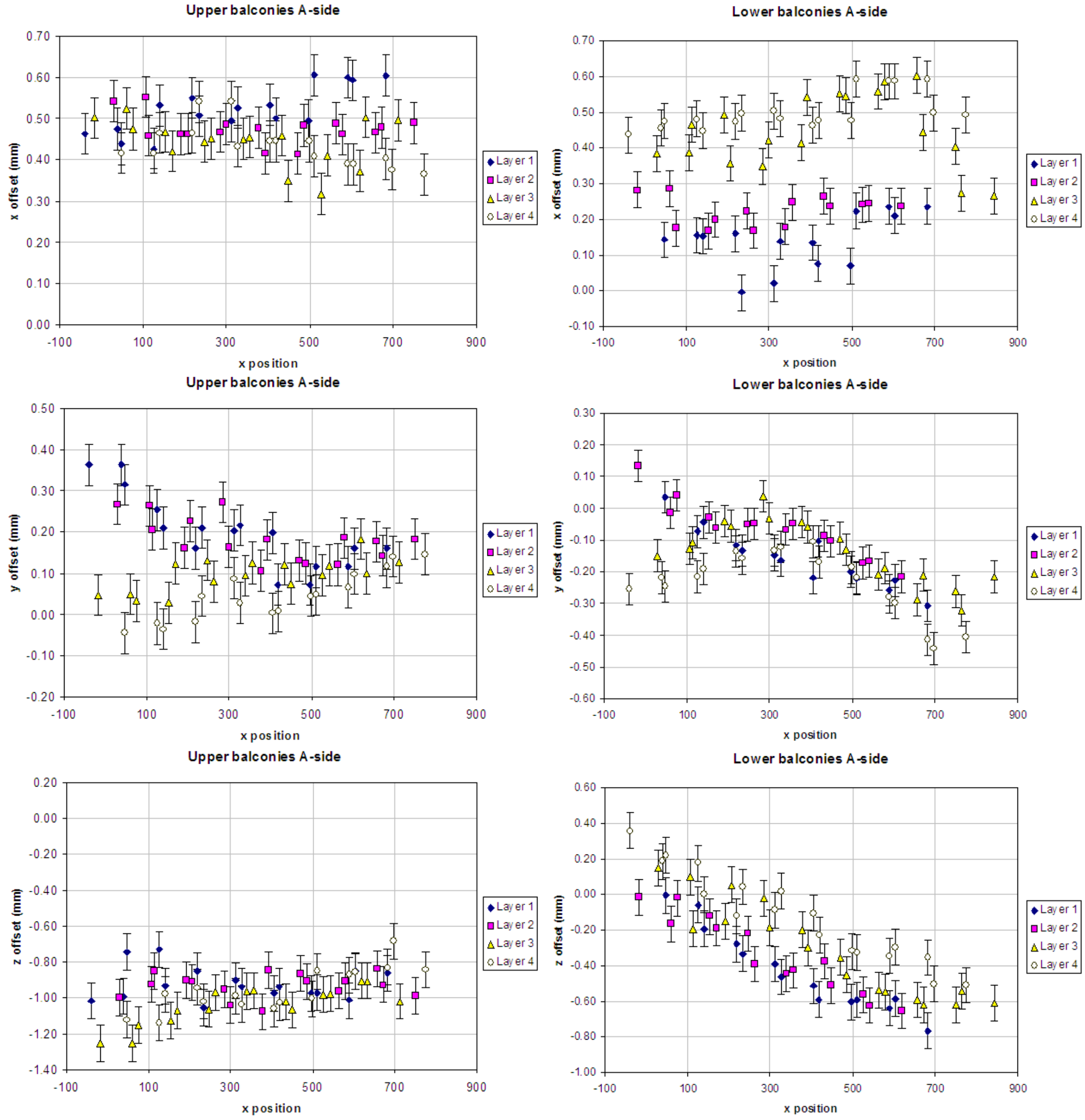

Figure 3.9: Offsets in x, y, and z for the precision pins of the upper and lower balconies on the A side versus the global x coordinate.

the detector. These measurements show that the Tracker Turicensis is located at its designed position within the accuracy of the various measurement techniques.

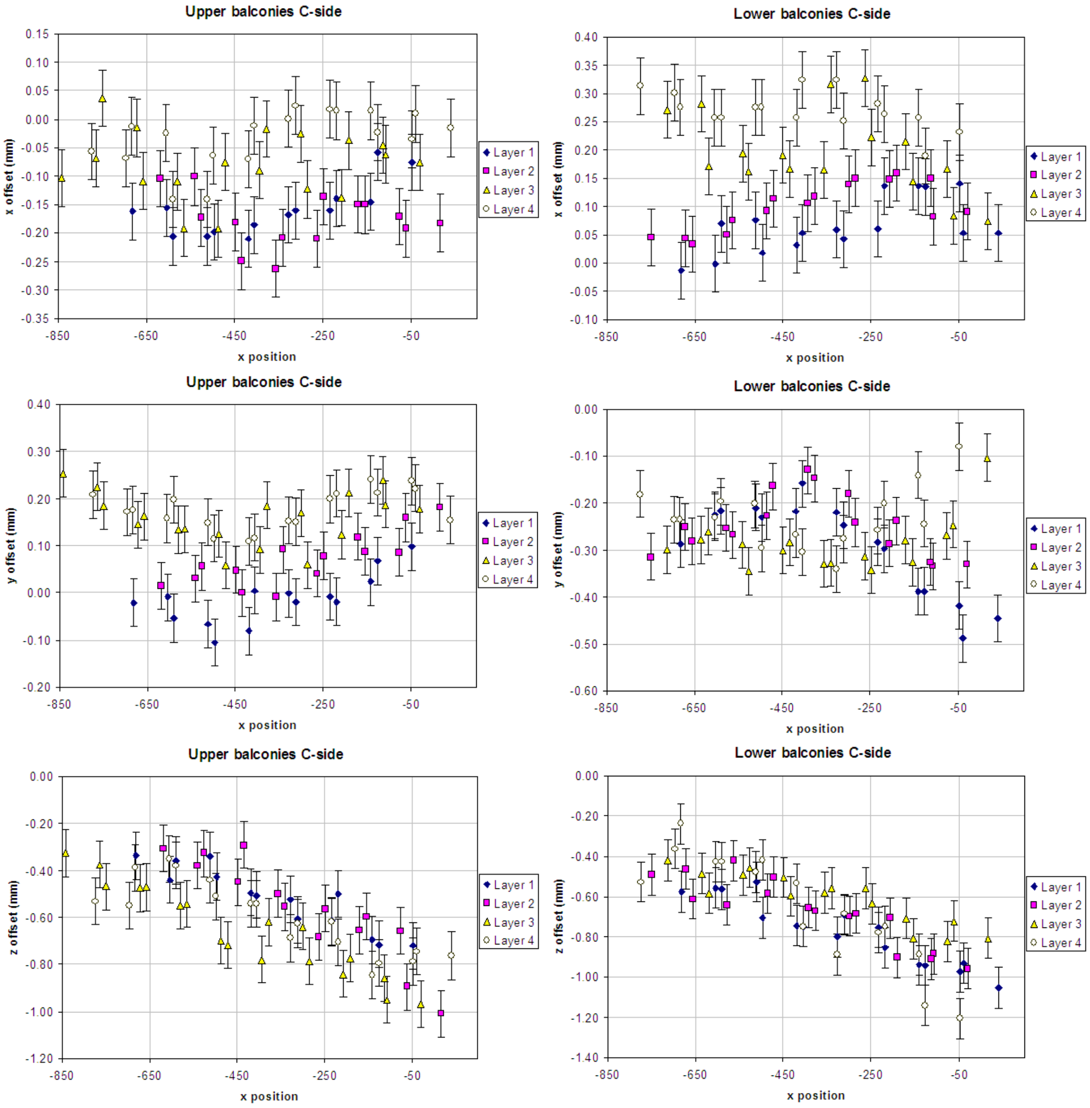

Figure 3.10: Offsets in x, y, and z for the precision pins of the upper and lower balconies on the C side versus the global x coordinate.

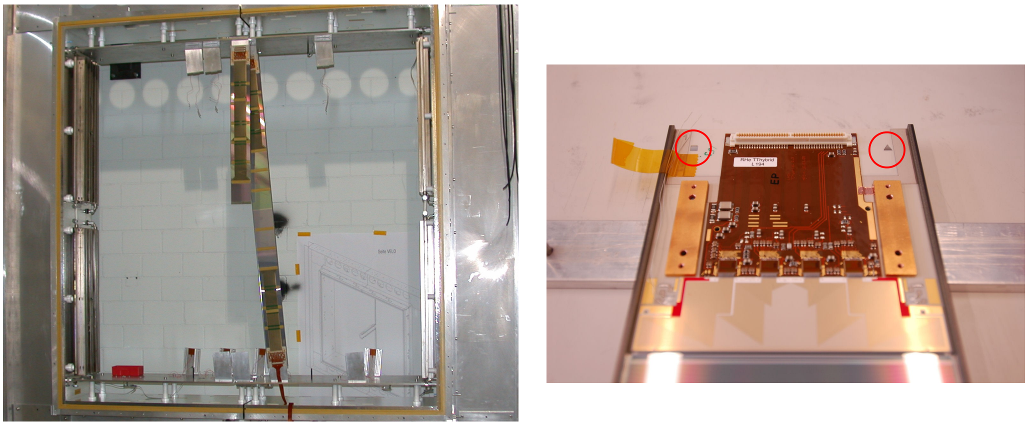

(a) (b)

Figure 3.11: A half-module mounted on an X layer and a full module mounted on a stereo layer in the test frame at the University of Zürich (a). Several balconies are mounted on the top and bottom cooling plates. The ceramic (b) at the end of a half-module with the readout hybrid. The red circles mark the cutouts used for the positioning of the modules.

Chapter 4

Tracking and alignment

Despite attempts to build the detector as precisely as possible, deviations from the designed positions are unavoidable. This affects the precision of the experiment. During its construction, the detector was surveyed several times. This data is implemented in the detector conditions. Nevertheless, one will never achieve the best possible precision of the experiment this way. Therefore, the software alignment uses reconstructed tracks and is able to improve the knowledge on the deviation from the designed position even more for each detector element. The goal of the alignment algorithm is to find the alignment parameters that minimise the track χ^2. The alignment parameters obtained from the alignment algorithm give an estimate on the real position for every element and improve the measurement precision of the detector. In the beginning this chapter will describe the different track types in LHCb and how they are reconstructed. Next the Kalman filter track fit will be explained. Then, the alignment procedure and strategy will be discussed. Finally, the different alignment database sets obtained from global alignments are presented.

4.1 Track types

Particles interesting to physics analyses do not necessarily travel through the full detector. Therefore, the reconstruction algorithms can find tracks using the full or only a fraction of the tracking system. The reconstructed tracks are classified depending on which subdetectors contribute to the track reconstruction. Figure 4.1 shows a sketch of the track types.

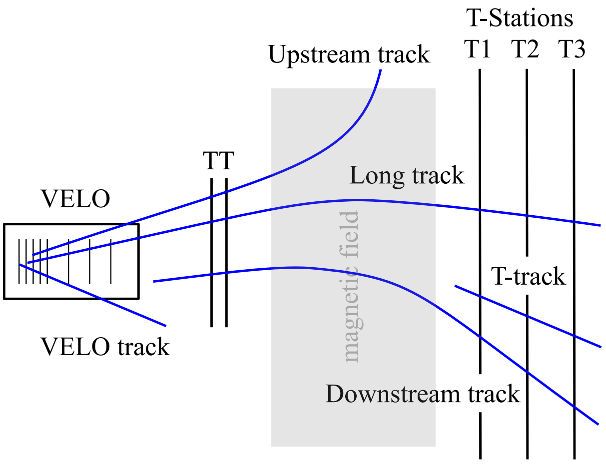

Figure 4.1: The five different track types defined in LHCb.

There are five different track types defined in LHCb:

- **Long tracks**
  Long tracks traverse the full length of the tracking system. They have hits in the VELO and the T-stations. These tracks exploit the full detector and hence are the most useful tracks. Note that a long track does not require hits in the TT.

- **VELO tracks**
  Particles produced within the VELO but passing outside the geometrical LHCb acceptance leave measurements only in the Vertex Locator. These tracks are used to improve the reconstruction of the primary vertex.

- **Upstream tracks**
  Low momentum particles get bent outside the geometrical detector acceptance by the magnetic field. These particles only generate measurements in the VELO and the TT.

- **Upstream tracks**
  These tracks only contain information from the TT and the T-stations. Long-lived neutral particles decaying outside of the VELO but within the LHCb acceptance produce this kind of tracks.

- **T-track**
  Tracks that have hits only in the T-stations are called T-tracks. They are used to improve the RICH2 reconstruction.

4.2 Track reconstruction

Due to the geometrical arrangement of LHCb, it is convenient to parameterise the tracks as a function of z, as z is the coordinate along the beam axis. The tracks are described by a collection of states at specific z positions. The track state vector consists of five parameters:

$$\vec{x}_z = \begin{pmatrix} x \\ y \\ t_x \\ t_y \\ \frac{q}{p} \end{pmatrix} , \tag{4.1}$$

where x and y denote the position at the given z position, $t_x = \frac{\partial x}{\partial z}$ and $t_y = \frac{\partial y}{\partial z}$ are the track slopes and q/p is the charge divided by the momentum of the particle. In the linear approximation a track state can be extrapolated to another z position via

$$\vec{x}_z = F_z \vec{x}_{z'} + \vec{w}_z \ , \tag{4.2}$$

where F_z is the transportation matrix and $\vec{w}_z$ is the process noise. Process noise is used to describe, for example, multiple scattering of a particle traversing material. The relation between the track state and the measurement (or hit) m_z, the quantity provided by the detector, is given through the projection equation

$$m_z = h_z(\vec{x}_z) + \epsilon_z \ , \tag{4.3}$$

where h_z is the projection function (see Eq. 4.16) and ϵ_z is the measurement noise.

As a track state has five free parameters, a track needs at least five hits to be well constrained. Therefore, a standalone tracking within a subdetector is only possible in tracking systems which have at least five layers or, in the absence of a magnetic field, at least four layers. The track reconstruction algorithms start by searching for track seeds in the VELO or T-stations and then expand these seeds to tracks containing hits from other subdetectors where possible, as described in Sec. 4.2.1.

The track reconstruction is divided into two parts, the pattern recognition and the track fitting. The job of the pattern recognition is to collect the hits that belong to a track. The track fitting determines the track parameters matching the hits best.

4.2.1 Pattern recognition

The LHCb track reconstruction software uses the following algorithms for the track finding:

VELO seed
The VELO pattern recognition [48, 49] searches for track segments in the VELO. The algorithm collects hits along a straight line and fits a straight line to them using a least-squares method. The smallness of the magnetic field in this area makes a momentum estimate impossible.

T-seed
The pattern recognition in the T-stations collects hits along a straight line in the y-z plane and uses a cubic function in the x-z plane [50]. The curvature in the x-z plane gives a first estimate of the particle momentum. For long tracks a more precise momentum estimate can be achieved assuming the track originated from the primary interaction, thus giving a better estimate on the bending of the particle trajectory. An alternative seeding algorithm is given in Ref. [51].

Forward tracking
The forward tracking starts with VELO seeds and searches for matching hits in the T-stations based on a Hough transform approach [52].

Track matching
The track matching [53, 54] extrapolates T-seeds to a specific z position, which is defined by the centre of the magnetic field. VELO seeds are extrapolated upstream to the same z position and are tested if they match the extrapolated T-seed.

Upstream tracking
The upstream tracking adds at least three TT hits to VELO seeds [55].

Downstream tracking
The downstream tracking adds at least three TT hits to T-seeds [56].

The most useful tracks, the long tracks, are reconstructed with the forward tracking and track matching algorithms. The two algorithm search for TT hits belonging to the long tracks within a search window. If the algorithm finds TT hits, they are added to the track. If a long track is found by both algorithms only one is kept.

VELO seeds that do not make it to a long track in the forward tracking or track matching are used in the upstream tracking. Using the T-seeds left over by the track matching algorithm, the downstream tracking adds TT hits. Seeds that could not be extended to long, upstream or downstream tracks are defined as VELO tracks in case of the VELO seeds and as T-tracks in case of the T-seeds.

4.2.2 Track fitting

Once all hits belonging to a track candidate are collected by the pattern recognition the track fit determines the track parameters that match the measurements the best. The LHCb track fitting uses a Kalman filter track fit [57, 58]. The Kalman method is an iterative method that adds one measurement after the other to the track, updating the track parameters to minimise the χ^2 contribution of the hit. There are several reasons which favour the use of the Kalman filter track fit. Two of them are, that the Kalman method is fast and, that it allows for a natural way to account for multiple scattering and energy loss. A detailed introduction to how the Kalman filter track fit adds hits iteratively is given in Ref. [21]. The Kalman filter proceeds in three steps:

- **Prediction:** The state $\vec{x}_z^{z'}$ at position z is predicted from the state $\vec{x}_{z'}$ at position z', using the transportation Eq. 4.2 .
- **Filter:** The prediction is updated using the measurement m_z at the same z position as the state $\vec{x}_z^{z'}$.

The prediction and filter steps are repeated until all measurements found by the pattern recognition are incorporated into the fit.

- **Smoothing**: After all measurements are added to the track, the information from the measurements added later is propagated back to the states of the previous measurements. The states of the track at all z positions are updated including the information of all other states.

In the following the superscript represents the level of information included in the track state and the subscript corresponds to the location of the track state. $\vec{x}_z^{z'}$ is the state at z predicted from the state at z'. $\vec{x}_z = \vec{x}_z^z$ is a filtered state at position z including the information of the measurement m_z at the same position z. The smoothed state is denoted by $\vec{x}_z^n$. Such a state contains the complete information from all n measurements included in the track fit.

Prediction

The predicted state $x_z^{z'}$ is derived using the transportation Eq. 4.2. The corresponding covariance matrix $C_z^{z'}$ is determined by

$$C_z^{z'} = F_z C_{z'} F_z^T + Q_z \ . \tag{4.4}$$

$C_{z'}$ is the covariance matrix of the state $\vec{x}_{z'}$ and Q_z is the covariance term belonging to the process noise, i.e. multiple scattering. These predictions are used to calculate the residual of the measurement m_z with respect to $\vec{x}_z^{z'}$. The covariance is determined using the projection in Eq. 4.16, the measurement matrix H_z and the measurement variance V_z. The predicted residual $r_z^{z'}$ and its covariance $R_z^{z'}$ are

$$\begin{aligned} r_z^{z'} &= m_z - h_z(\vec{x}_z^{z'}) \ , \\ R_z^{z'} &= V_z + H_z C_z^{z'} H_z^T \ . \end{aligned} \tag{4.5}$$

For example, the measurement matrix $H_z = H(z)$ for a vertical TT strip measuring the x coordinate is given by

$$H(z) = \begin{pmatrix} 1 & 0 & 0 & 0 & 0 \end{pmatrix} \ . \tag{4.6}$$

The contribution of this measurement to the global χ^2 of the fit is

$$(\chi^2_+)_z^{z'} = r_z^{z'}(R_z^{z'})r_z^{z'} \tag{4.7}$$

Filter

The information of the measurement m_z is added to the track state via

$$\begin{aligned} \vec{x}_z &= \vec{x}_z^{z'} + K_z r_z^{z'} \ , \\ C_z &= (\mathbb{1} - K_z H_z) C_z^{z'} \ , \end{aligned} \tag{4.8}$$

where K_z is a 5 × 1 gain matrix with

$$K_z = C_z^{z'} H_z^T (R_z^{z'})^{-1} \ . \tag{4.9}$$

A complete derivation of the gain matrix is given in Ref. [21]. The residual of the state r_z and its covariance matrix R_z, including the measurement m_z, are given by

$$\begin{aligned} r_z &= m_z - h_z(\vec{x}_z) = (1 - H_z K_z) r_z^{z'} \ , \\ R_z &= V_z - H_z C_z H_z^T \ . \end{aligned} \tag{4.10}$$

This leads to a contribution to the total filtered χ^2 of

$$(\chi^2_+)_z = r_z R_z^{-1} r_z \ . \tag{4.11}$$

The Kalman filter fit determines the parameters of the state $\vec{x_z}$ such that the χ^2 contribution of the measurement m_z is minimal.

Smoothing

The last step in the Kalman filter is to propagate the information of the states backward. The state vector and the covariance matrix at position $\tilde{z}$ after the smoothing are

$$\begin{aligned} \vec{x}_z^n &= \vec{x}_z + A_z(\vec{x}_{\tilde{z}}^n - \vec{x}_{\tilde{z}}^z) \ , \\ C_z^n &= C_z + A_z(C_{\tilde{z}}^n - C_{\tilde{z}}^z) A_z^T \ , \end{aligned} \tag{4.12}$$

where the state $\vec{x}_{\tilde{z}}^n$ denotes the smoothed state before the state $\vec{x}_z$ is smoothed and the gain matrix A_z is given by

$$A_z = C_z F_{\tilde{z}}^T (C_{\tilde{z}}^z)^{-1}. \tag{4.13}$$

This yields the residual of the smoothed state and its covariance matrix

$$\begin{aligned} r_z^n &= m_z - h_z(\vec{x}_z^n) \ , \\ R_z^n &= V_z - H_z C_z^n H_z^T \ , \end{aligned} \tag{4.14}$$

and finally, the value to be minimised in the track fitting, the total χ^2, the sum of all the smoothed state contributions

$$(\chi^2_+)_z^n = r_z^n (R_z^n)^{-1} r_z^n \ . \tag{4.15}$$

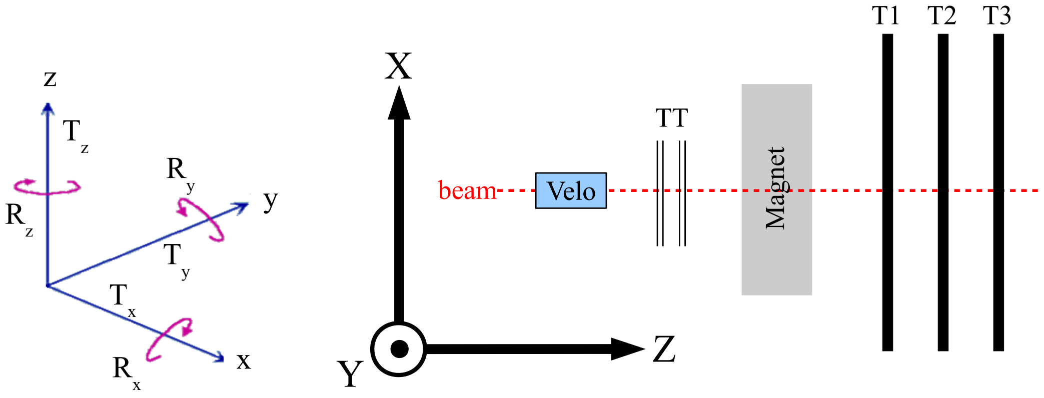

(a) (b)

Figure 4.2: The six degrees of freedom T_x, T_y, T_z, R_x, R_y and R_z of every alignable detector element (a) and the orientation of the LHCb detector within the LHCb coordinate system as seen from above (b).

4.3 Alignment of the tracking detectors at LHCb

The alignment of the tracking detectors at LHCb is based on a minimum χ^2 algorithm, using the *closed-form* method, i.e. it takes into account correlations between the hit residuals. LHCb uses the Kalman filter track model for alignment and physics analysis.

4.3.1 The alignment parameters

Every detector element that can be aligned adds six alignment parameters to the alignment algorithm. Three parameters are given by translations in the spatial dimensions x, y and z. These parameters are denoted by T_x, T_y and T_z. The rotation of the element around each spatial axis adds another three alignment parameters, denoted by R_x, R_y and R_z. Figure 4.2 shows the six degrees of freedom and the orientation of the LHCb detector within the LHCb coordinate system as seen from the top.

As the Tracker Turicensis and the Inner Tracker are silicon microstrip detectors measuring one spatial coordinate, the sensitivity of the alignment algorithm to a translation or a rotation of an element in any of the three spatial dimensions depends on the arrangement of the strips in space. The same holds for the straw tube Outer Tracker. The residual between a track state an its measurement m is given in the x–y plane at the z position of the strip. The projection of the track state onto the measurement is

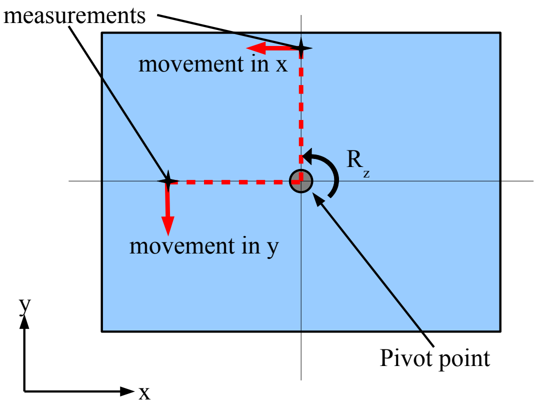

Figure 4.3: The effect of the relative position of the measurement to the pivot point in the alignment shown for a TT layer. The relative position of the measurement with respect to the pivot point of the alignment element defines the sensitivity of the measurement in the alignment algorithm. A rotation R_z transforms into a movement in x if there is a large lever arm in y. A large lever arm in x transforms into a movement in y.

$$h(\vec{x}_z) = x\ cos(\alpha_{stereo}) + y\ sin(\alpha_{stereo})\ , \tag{4.16}$$

where $\alpha_{stereo} = 0°, \pm 5°$ is the stereo angle of the layer. The residual given by $r = m - h(\vec{x}_z)$ is clearly insensitive to a change in y if the stereo angle is zero and only very limited in case of a stereo angle of $\pm 5°$. On the other hand, the alignment is sensitive to any change in x. Therefore, an alignment of TT elements in x can be made extremely precisely, whereas the determination of T_y is much more difficult. Nevertheless, the interplay of the residual contributions from different elements of the detector result in some sensitivity to alignment parameters that at a first sight could be neglected. For example, each of the four TT layers has some alignment sensitivity in the z direction, as the average track slope changes over the x–y plane in the TT. In general, the larger a detector element is, the more sensitive it is to the different alignment parameters.

The sensitivity of the alignment procedure to rotations of a detector element depends on the relative position of the measurement with respect to the pivot point of the element and how much the rotation transforms into a movement in x. For example, a rotation R_z considering a measurement with large lever arm in y leads at first approximation, to a movement in x, whereas a large lever arm in x leads to a movement in y. Figure 4.3 illustrates this behaviour for a TT layer. The sensitivity, for instance in the x coordinate, can be estimated using the linearised track model in the residual.

$$r = m - h(x) \rightarrow r = m - H_x \cdot x \qquad \text{with } H_x = \frac{\partial h}{\partial x} \ , \tag{4.17}$$

where x is the first component of the track state $\vec{x}$ and H_x is the x component of the measurement matrix H. If the measurement is set to zero ($m = 0$), one gets

$$x = -\frac{r}{H_x}. \tag{4.18}$$

The mean of the x distribution will give an estimate on the x position of the element and the RMS σ of the distribution will give an estimate on the alignment sensitivity through

$$\text{sensitivity} = \frac{\sigma}{\sqrt{N_{tracks}}} \ . \tag{4.19}$$

Equation 4.19 also shows that the sensitivity depends on the number of tracks that go into the alignment of an element. That means, only elements with enough hits can be aligned and more tracks are needed to align for parameters with low sensitivity.

4.3.2 Global track covariance matrix

The calculation of the alignment parameters using the *closed-form* method depends on the covariance matrix R of the residuals. Unfortunately, the covariance matrix is not calculated completely in the Kalman track fit because the correlations between the different states on the track are not calculated. These correlations have to be determined before they can be used as input to the *closed-form* method. This is achieved using a novel approach described in Ref. [59]. The covariance matrix is predicted from a neighbouring measurement given by Eq. 4.4 where

$$C_z^{z'} = F_z C_{z'} F_z^T + Q_z \ , \tag{4.20}$$

and the covariance matrix for the adjacent pair of states $(x_{z'}, x_z^{z'})$ is

$$Cov(x_{z'}, x_z^{z'}) = \begin{pmatrix} C_{z'} & C_{z'} F_z^T \\ F_z C_{z'} & F_z C_{z'} F_z^T + Q_z \end{pmatrix} \ , \tag{4.21}$$

using the transportation matrix F_z.
The method presented in Ref. [59] derives the correlation between any two states in the track by propagating the covariance information via intermediate states. This yields the covariance matrix for any combination of two states $(x_{z'}^n, x_\ell)$

$$C_{z',\ell}^n = C_{z',z}^n (C_z^n)^{-1} C_{z,\ell}^n = A_{z'} C_{z,\ell}^n \qquad z' \leq \ell \ , \tag{4.22}$$

using the smoother gain matrix introduced in Eq. 4.13.

The possibility to propagate covariances through the states of a track makes it possible to also use vertex information for the alignment [59]. This includes the possibility to include mass constraints in the alignment procedure.

4.3.3 Minimum χ^2 formalism for alignment

The track χ^2 can be defined as

$$\chi^2 = [m - h(x)]^T V^{-1} [m - h(x)] \ , \tag{4.23}$$

where m is a measurement vector, $h(x)$ is the measurement model and x is the track parameter vector. The matrix V is the covariance matrix of the measurements.

In Eq. 4.23, the measurement model depends only on the track parameters x. The measurement model can be extended to consider alignment parameters α,

$$h(x) \rightarrow h(x, \alpha) \ . \tag{4.24}$$

The alignment parameters α are common to all tracks. To estimate α, the χ^2 values of the tracks are minimised with respect to α with the condition that the track parameters already minimise the track χ^2 given an initial set of alignment parameters α_0. The minimisation uses the total derivative

$$\frac{d}{d\alpha} = \frac{\partial}{\partial\alpha} + \frac{dx}{d\alpha}\frac{\partial}{\partial x} \ , \tag{4.25}$$

where

$$\frac{dx}{d\alpha} = \frac{\partial^2\chi^2}{\partial\alpha\partial x}\left(\frac{\partial^2\chi^2}{\partial x^2}\right)^{-1} \ , \tag{4.26}$$

is a direct consequence of the requirement that the track parameters already minimise the track χ^2, i.e $\frac{\partial\chi^2}{\partial x} = 0$. This gives the minimisation equation

$$\frac{d\chi^2}{d\alpha} \equiv 0 \ . \tag{4.27}$$

Linearising the problem around the initial alignment parameters α_0 and applying the Newton-Raphson method gives

$$\left.\frac{d^2\chi^2}{d\alpha^2}\right|_{\alpha_0} \cdot \Delta\alpha = -\left.\frac{d\chi^2}{d\alpha}\right|_{\alpha_0} \ , \tag{4.28}$$

with $\Delta\alpha$ minimising the χ^2.

Using a linearisation of the residual $r = m - h(x, \alpha)$ around the expansion point $(x(\alpha_0), \alpha_0)$, its derivative

$$A = \frac{\partial r}{\partial\alpha} \ , \tag{4.29}$$

and Eq. 4.26, the total derivative with respect to the alignment parameter α in Eq. 4.25 is given by

$$\frac{d}{d\alpha} = \frac{\partial}{\partial\alpha} - A^T V^{-1} H C \frac{\partial}{\partial x} \ , \tag{4.30}$$

where $H = \frac{\partial h(x)}{\partial x}|_{x_0}$ is the derivative of the track model at the initial track parameter estimate x_0. This yields for the derivatives in Eq. 4.28

$$\frac{d\chi^2}{d\alpha} = 2A^T V^{-1}(V - HCH^T)V^{-1}r \ , \tag{4.31}$$

$$\frac{d^2\chi^2}{d\alpha^2} = 2A^T V^{-1}(V - HCH^T)V^{-1}A \ . \tag{4.32}$$

The matrix $R \equiv V - HCH^T$ is the covariance matrix of the residual r. The derivation of the last three equations can be found in Ref. [60].

If the track parameters x minimise the track χ^2 for the given initial alignment parameters α_0, $H^T V^{-1} r = 0$ and Eq. 4.31 simplifies to

$$\frac{d\chi^2}{d\alpha} = 2A^T V^{-1} r \ . \tag{4.33}$$

The change in the alignment parameters $\Delta\alpha$ can be derived by inserting the expressions from Eq. 4.32 and Eq. 4.33 into Eq. 4.28. In the case where the residual is non-linear in terms of the track or alignment parameters, several iterations of the procedure are necessary to converge on the optimal set of alignment values $\Delta\alpha$.

4.4 Weak modes

As the determination of the alignment parameters is based on the χ^2 minimisation method, the procedure is not sensitive to any linear combination of alignment parameters that leaves the χ^2 almost invariant. Such a combination of alignment parameters is called a weak mode. Figure 4.4 illustrates such a weak mode.

The alignment procedure has to prevent detector elements from moving along such weak modes. Alignment parameters contributing to weak modes are those which have the smallest eigenvalues of the matrix $\frac{d^2\chi^2}{d\alpha^2}$ [31]. Removing the eigenvectors related to these eigenvalues prevents detector elements being moved along the weak modes. An alternative is to introduce Lagrange multipliers adding constraints to the second derivative of the χ^2. A third alternative is to fix one or more detector elements to its survey position.

4.5 Alignment strategy

As the LHCb tracking system consists of several independent subdetectors separated in space, the procedure how to reach a well aligned detector must be defined. The procedure that was chosen is to align all detector components with respect to the VELO. This means, that the VELO coordinate system defines the global LHCb coordinate system.

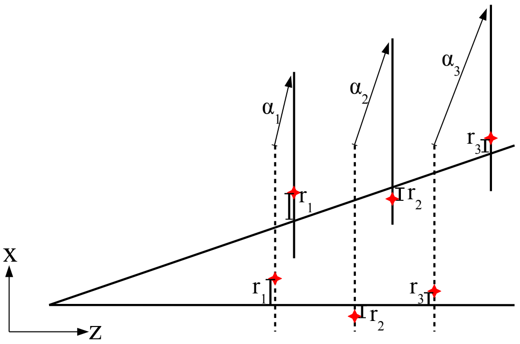

Figure 4.4: A weak mode, e.g. a shearing in the x-z plane. The dashed lines represent the measurement assuming the modules are at their nominal position. The χ^2 minimisation is insensitive to a linear combination of the alignment parameters α_i. The total sum of the residuals $r_i = m_i - h(x_i)$ remains the same for the shifted modules (vertical solid lines).

The VELO position is known to a precision of 10 μm, and is limited by the precision of the motion control system that moves the two VELO halves in and out depending on the beam conditions. Hence, the global LHCb detector position has an uncertainty of 10 μm. The precision of the internal VELO alignment is of the order of 5 μm. Of central interest is the relative alignment between the different subdetectors. For the relative VELO T-station alignment a precision of around 20 μm can be achieved [61]. The relative position between the different tracking systems affects physical observables such as the reconstructed invariant mass.

In principle the full LHCb tracking system can be aligned in one go. That means, using long tracks, all subdetectors of the tracking system are relatively and internally aligned at the same time. Such an alignment is called a global alignment. In practice however, the alignment is split into two steps, the VELO is first aligned internally. Then the TT, IT and OT are aligned with respect to the VELO. To make sure that the alignment algorithm converges properly it is important to start with a set of initial alignment parameters close to their real values. The initial alignment parameters are obtained from the detector surveys performed during and after the assembly of the detector.

Initial alignment parameters

All parts of the LHCb tracking system were carefully surveyed during the assembly and construction of the detector. The results obtained from these surveys are implemented into the conditions database and give a set of initial alignment parameters for each subdetector. The results from the survey of the TT are shown in Chapter 3 and Ref. [46]. The survey results of the VELO, IT and OT are shown in Refs. [62] (VELO),

[63] (IT) and [31] (OT).

Often, detectors built for particle physics experiments use tracks from cosmic rays to perform a very first alignment and to verify the survey results. However, the geometrical setup of LHCb with its planar and vertical sensors will only allow the OT to collect enough of such tracks to perform a first alignment and test the survey data. This initial OT alignment using cosmic rays showed a reasonable precision of the survey [31, 64]. Fortunately, beam injection tests from the SPS into the LHC in 2008, provided the possibility to verify the survey results of the VELO and IT well before the first *pp* collisions in the LHC. An alignment performed for the VELO using these data sets demonstrates the high precision of the VELO survey [65]. The results of the IT alignment using the injection-test data are shown in Ref. [66]. Neither cosmic rays data nor injection-test data could be used to perform a proper test of the TT survey, since the reconstructed injection-test tracks illuminated only small parts of the TT. An internal TT track reconstruction is not possible, as the TT has only four layers, and therefore, tracks need information from other subdetectors.

The verification of the survey data of the VELO and the OT using the alignment algorithm on cosmic and injection-test data confirm the survey data for the two subdetectors. The initial alignment parameters are set to the survey data for both. Furthermore, also the TT initial alignment parameters are set to the survey data. However, the alignment of the IT using the injection-test data showed a poor survey accuracy of the IT. The alignment values obtained from the IT alignment using the injection-test data did not lead to the required precision (see Sec. 5.2.1). An independent relative alignment of the IT using collision data is necessary before starting a global alignment. In fact, the IT is the only subdetector that needed an internal pre-alignment to compensate for the large offsets.

VELO alignment

The VELO alignment itself is divided into three steps [67]:

1: The relative alignment of the ϕ and R sensors glued together to one VELO module. This alignment is performed only once [68].

2: The module alignment within each VELO half. This alignment is performed as a cross check for relative module movements at the beginning of each fill, as the two halves are retracted at each fill [69].

3: The relative alignment of the VELO halves. The halves alignment is also performed at the beginning of each fill [70].

Two different alignment techniques were compared for the VELO alignment. The first technique is a relative sensor alignment based on fits to the residual distribution and a module and halves alignment based on the Millepede algorithm [67, 71]. The second technique is the χ^2 minimisation method based on Kalman filter fitted tracks discussed in Sec. 4.3.3. The two different techniques agree well and yield similar alignment pa-

Detector	Granularity
TT	full station → layers → modules → sensors
IT	T-stations → boxes → modules → sensors
OT	T-stations → C-frames → modules

Table 4.1: The granularity levels of the different subdetectors. "modules → sensors" means that the sensors are grouped in modules etc.

rameter values [65].

Global alignment of the detector

The global alignment of the detector aligns the TT, IT and OT internally and relative to the VELO. The alignment values for the VELO are fixed to the values obtained from the separate VELO alignment.

The choice of the degrees of freedom for TT, IT and OT is crucial to obtain reasonable alignment values. The alignment algorithm does not only allow to align for each individual detector element, but is able to provide alignment values for groups of elements on different granularity levels. For instance, the TTaX layer can be aligned as a whole, grouping all modules within the layer. The levels of granularity of the TT, IT and OT are shown in Tab. 4.1. The degrees of freedom for the alignment elements have to be chosen such that weak modes are avoided. First, large structures such as the TT station, IT boxes or OT stations are aligned. In a second iteration, smaller structures are added to the alignment algorithm. In practice, to reduce the number of degrees of freedom in the alignment algorithm, individual sensors are not yet aligned. The sensor level will be added to the procedure once a reliable alignment of the module level is achieved. The alignment values obtained from the first iteration are used as initial alignment parameter for the second iteration. Figure 4.5 shows the second and third granularity level of the IT and the OT. The second and third granularity level for the TT are shown in Fig. 4.6.

The TT and IT are designed such that a module overlays with adjacent modules in the x–y plane (see Sec. 2.5.2). In the T-stations the IT and the OT are arranged such, that the sensitive regions of the two subdetectors overlap in the x–y plane in each of the three stations. Consequently, some tracks travel through these overlap regions generating two hits in the same layer or generating hits in the two T-station subdetectors. These tracks are important for the relative alignment within the layers or between the two subdetectors. To increase the sensitivity of the alignment algorithm to these kind of tracks, the overlapping tracks are heavily weighted compared to other tracks.

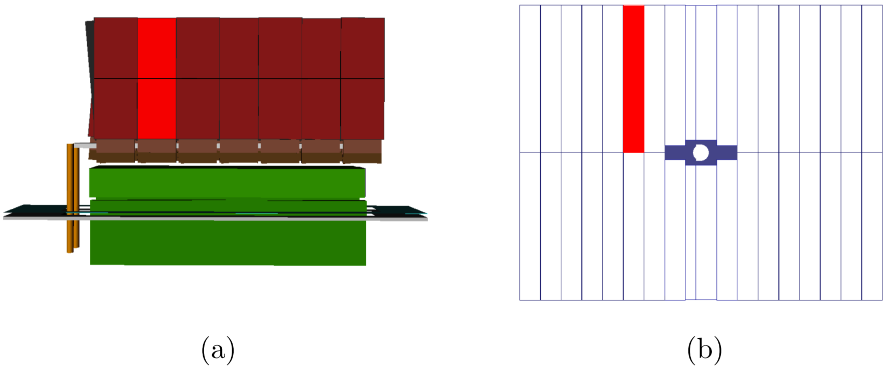
(a) (b)

Figure 4.5: The different granularity levels of the Inner Tracker (a) and of the Outer Tracker (b). The left picture shows an IT A side box (second level of granularity used in the alignment) with a ladder marked in light red (third level of granularity). The picture on the right-hand side shows a OT X C-frame (second level of granularity) with a module marked in light red (third level of granularity).

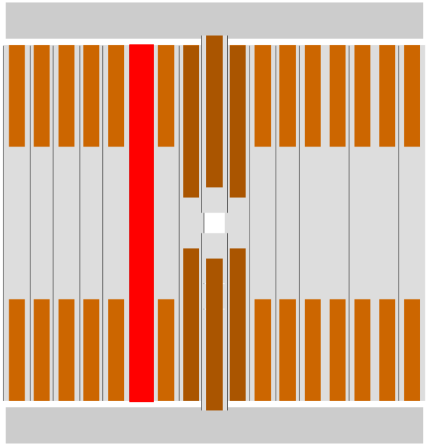

Figure 4.6: The layers of the Tracker Turicensis corresponds to the second level of granularity used in the alignment (TTbX layer is shown here). Marked in light red is a module, representing the third level of granularity.

4.6 Global alignment databases

The global alignment is performed by the LHCb alignment group. Each alignment provides a set of alignment values which is stored in the conditions database. Such a set of stored alignment values is referred to as an alignment database. The database is

Version	Description
v1.x	very first alignment based on 2009 magnet-off data
v2.x	based on 2009 magnet-on data extra IT stack alignment TT pitch fix
v3.x	based on 2009 magnet-on data fixed VELO halves alignment
v4.x	based on 2010 magnet-on data with J/ψ mass constraint
v5.x	based on 2011 magnet-on data new magnetic field map with J/ψ mass constraint

Table 4.2: The different alignment databases provided by the LHCb alignment group. The databases are used as initial alignment parameters for an additional alignment of the Tracker Turicensis.

Element	Degrees of freedom
TT modules [3]	$T_x R_z$
IT boxes IT modules	$T_x T_z R_z$ $T_x R_z$
OT T-stations OT C-frames OT modules	T_z T_x $T_x R_z$

Table 4.3: The alignment elements and corresponding degrees of freedom for the latest global alignment v5.4.

labeled depending on the data set used and the level of alignment performed. The label looks like vX.Y, where in general X defines the dataset used and the Y refers to the degrees of freedom of the alignment elements during the alignment. Several alignment databases have been provided since the first collision data in autumn 2009. Table 4.2 lists the different generations of alignment databases provided for the different data sets. It should be pointed out, that a higher version number of the alignment database does not implicitly mean a better alignment. During technical stops parts of the tracking system are moved, making a new alignment necessary for every run period. The databases used for reconstruction of 2010 and 2011 data are the v4.x and v5.x database generation respectively.

Finally, the most important database in summer 2011 is the version v5.4 obtained from an alignment performed using an updated field map of the dipole magnet and

---

[3] The alignment elements on the module level in TT are in general full modules, except the half-modules in the central region of the TT (above and bellow the beam pipe).

2011 collision data. The degrees of freedom for this alignment are listed in Tab. 4.3. An additional alignment constraint was added by requiring the reconstructed J/ψ mass from $J/\psi \to \mu^+\mu^-$ to be constrained to its PDG mass [72]. This database is used to perform the track reconstruction for the data collected in the first half of 2011, the data set used for the results shown during the 2011 summer conferences.

Since the first particle collisions, various corrections had to be made to the detector description database, the alignment code and the magnetic field map to solve problems spotted during the alignment procedure. In the following sections the experience gained during several alignment procedures performed for the TT will be described.

Chapter 5

Alignment of the Tracker Turicensis

As discussed in the previous chapter, the alignment software of LHCb allows the full tracking system to be aligned simultaneously. The number of free alignment parameters is very large in such global alignments. Therefore, the global alignment only aligns for the degrees of freedom that are well under control. However, one can perform an additional alignment of individual subdetectors on top of the global alignment. These alignment tests help to understand and validate the result obtained in the global alignment. Adding degrees of freedom in the additional alignment can give useful information for a future global alignment where more degrees of freedom are included. This chapter shows the experience gained during alignment tests performed for the TT. Section 5.1 shows the results obtained from the injection-test data. The results obtained from collision data are discussed in Sec. 5.2 and 5.3. The chapter concludes with a presentation of the effect of different alignment databases on the $J/\psi \rightarrow \mu^+\mu^-$ mass.

Although the track reconstruction at LHCb can be performed without hits from the Tracker Turicensis, adding TT hits to the track fitting significantly increases the momentum and invariant mass resolution of the detector. As an example, Fig. 5.1 shows the $J/\psi \rightarrow \mu^+\mu^-$ invariant mass signal using TT hits in the track fit and without using TT hits in the fit. The width of the signal improves from 17.4 ± 0.3 MeV/c^2 to 15.7 ± 0.3 MeV/c^2 when using TT hits in the reconstruction. The level of improvement of the mass resolution depends on the precision of the relative and internal alignment of the TT.

The TT alignment tests shown in this chapter are all performed for detector elements of the TT only. Most of them are performed on top of an initial global alignment, using the output of the global alignment as starting point for the TT alignment. An

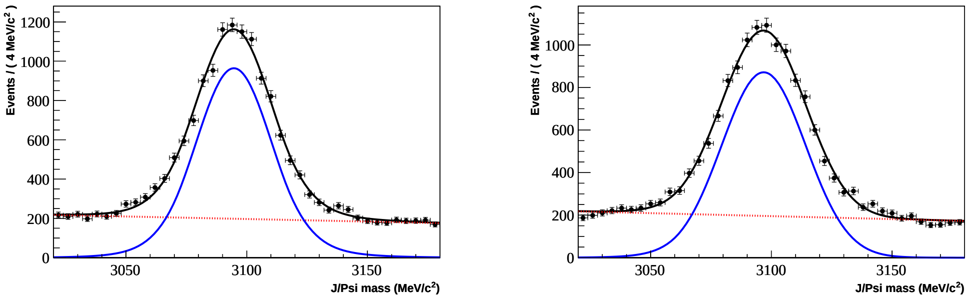

(a) (b)

Figure 5.1: The J/ψ invariant mass resolution with (a) and without (b) TT hits used in the track fitting.

Detector element	Degrees of freedom	Alignment degrees of freedom
full TT station	$T_xT_yT_zR_xR_yR_z$	6
TT layer $(0°, +5°, -5°, 0°)$	$T_xT_zR_yR_z$	16
TT module (60 full modules + 8 half-modules)	T_xR_z	128

Table 5.1: The sensitive alignment parameters of the TT.

additional TT alignment using the same degrees of freedom for the TT as the ones already used during the global alignment shows if a global alignment reached a stable minimum. Moreover, one would like to add additional degrees of freedom to improve the precision of the alignment. The alignment tests described here have the goal to gain experience and are not meant to be used as a contribution to the alignment databases used for physics event reconstruction. The alignment databases used for the event reconstruction are strictly obtained by a global alignment. Exceptionally, the alignment with injection-test data and the alignment with the very first collision data were done without prior global alignment. In the remainder of this chapter the experience gained during the alignment tests of the TT are chronologically given.

The considerations described in Sec. 4.3.1 yield the TT alignment degrees of freedom listed in Tab. 5.1. Obviously, all alignment elements of the TT can be aligned for the parameters T_x and R_z, as these are sensitive to movements in x direction. The dimensions of the layers allow to align the layers additionally for a translation in z and a rotation around the y axis. Finally, the full TT station can be aligned in all six parameters as it includes the two layers with opposite stereo angle $\pm 5°$ giving sensitivity to a translation in y and for a rotation around the x axis.

5.1 TED alignment

Attempts were made to perform a first alignment of the TT using data collected during injection tests from the SPS to the LHC in September 2009. During these tests the beam coming from the SPS was dumped into the Transfer-line External Beam Dump (TED). The impact of the beam particles into the beam stopper produced a spray of secondary particles that traversed the LHCb detector. Events collected during these injection tests are referred to as TED events. Figure 5.2 shows the location of the TED and the spray of the particles produced. The TED is located behind LHCb. Hence, the particles traversed LHCb coming from the back of the detector.

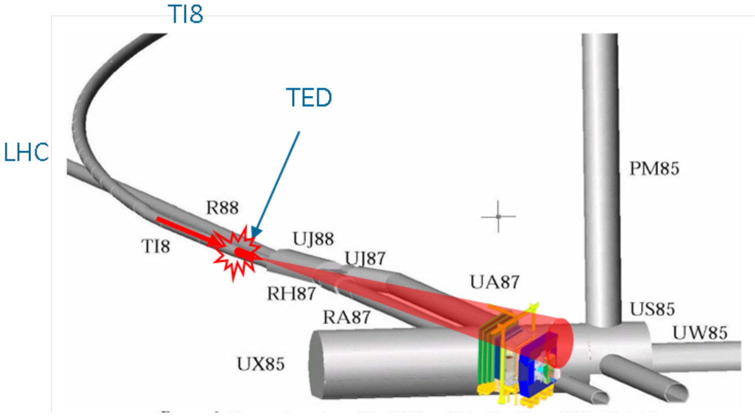

Figure 5.2: The TED in the transfer line TI8 between the SPS and the LHC. The red cone indicates the spray of particles generated by the beam dump. Note, that the direction of these particles is reverse from the direction of the particles coming from beam collisions.

The tracks in TED events are reconstructed using the upstream track reconstruction. Due to the size of the VELO, only a few hundred tracks could be reconstructed in the full data sample. As the beam stopper is located 350 m away from LHCb, the tracks are more or less parallel. The distribution of the tracks in the TT is defined by the projection of the VELO onto the TT under the angle of the incoming particles (see Fig. 5.3). During the injection tests, the VELO was in the opened position.

The small number of tracks and the small spread of the tracks in the TT allows only for an alignment of the full TT station in x and, therefore, the profit in terms of alignment of this study is limited. On the other hand, the TED runs produced the first tracks reconstructed in two different subdetectors at LHCb and gave confidence on the survey data by the fact that the residual distribution of the TT hits to extrapolated VELO tracks has a peak as shown in Fig. 5.4. The peak comes from hits belonging to the track, whereas the background comes from random combinations of tracks and hits. The residual before (black) and after (red) the full TT station alignment for the

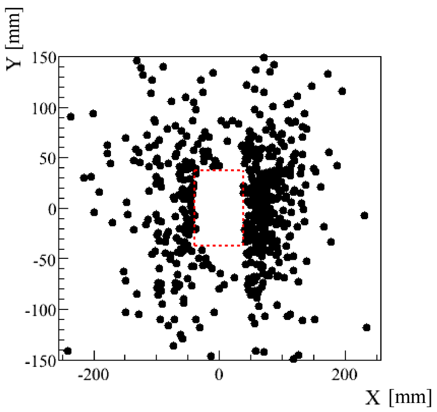

Figure 5.3: The upstream track distribution in the TT for a TED data sample. Due to the almost parallel tracks the distribution is defined by the projection of the VELO onto the TT. The figure shows only the innermost region of the TT. The red dashed square shows the beam pipe hole in the TT.

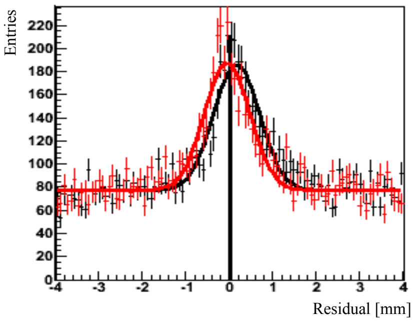

Figure 5.4: The residual of the TT hits to extrapolated VELO tracks for TED data. The residual is shown before (black) and after (red) the full TT station alignment for the parameter T_x.

parameter T_x are shown.

A larger number of tracks spread over a larger fraction of the TT could have been used if the downstream track reconstruction had been run. The very high occupancy of the IT and the TT during the TED runs made this an extremely difficult task. The occupancy in the IT was 20 times higher during the TED runs than it is in normal LHCb running condition [73]. In addition, the z distance between the IT and TT, which is 5 m, makes the reconstruction very sensitive to any misalignment within the IT or between the IT and the TT. The standard upstream reconstruction algorithm had to be adapted to the TED events, where the tracks are not coming from the interaction point. An algorithm was developed to reconstruct such TED downstream tracks, but could never be properly applied, as tests could not assure a high enough quality of the reconstructed tracks.

5.2 Alignment with first collision data

The first *pp* collision events at LHCb were recorded in November 2009. The colliding proton pairs had a centre-of-mass energy of 900 MeV. This data is divided into two subsamples: data taken with the LHCb dipole magnet off and data taken with the magnet on. To prevent the VELO getting damaged due to the larger beam size at 450 GeV beam energy compared to the designed size, the VELO halves were positioned 15 mm away from their nominal closed position [23].

5.2.1 Magnet-off data

The magnet-off data provides a sample of a few thousand straight tracks that could be reconstructed in all subdetectors of the tracking system. However, a look at the residuals of TT hits to extrapolated T-tracks from different IT stacks shows a bad relative alignment of the different IT stacks. An IT stack defines a set of three IT boxes in a the same location within each T-station, for example the three boxes on the A side. Figure 5.5 shows the residuals of TT hits with respect to extrapolated T-tracks reconstructed either in the A or the C side IT stack. The track residual for the A side stack peaks at about -1 mm, whereas the track residual of the C side stack peaks at about 2 mm. This shows that the two stacks do not point into the same direction, i.e. the IT stacks are insufficiently relatively aligned. The width of the peak is of the order of mm, which is related to the misalignment within the IT and the TT. In a perfectly aligned detector the width would be of the order of the TT spatial resolution (55 μm).

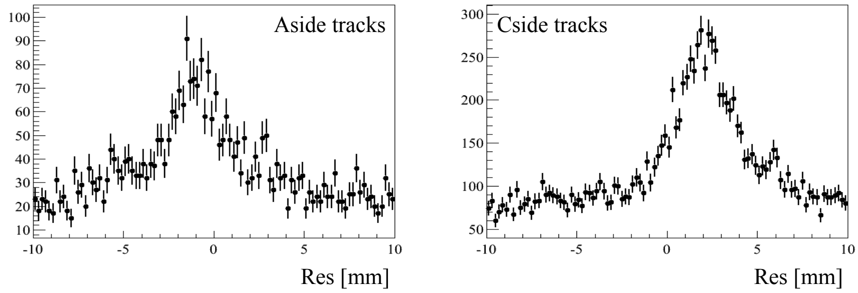

Figure 5.5: The residual of TT hits with respect to extrapolated T-tracks reconstructed in the A side (left) and the C side (right) IT stacks. The distributions peak clearly at different values, showing that the two stacks are badly aligned relative to each other.

This problem makes an IT interstack alignment necessary before starting to align the TT for any alignment parameter. A coarse *by-eye* alignment of the IT stacks was performed in the x direction. The boxes in T3 were kept at their surveyed position, whereas the boxes in T1 and T2 were moved in x direction, such that the residual distributions of TT hits with respect to the extrapolated T-tracks all peak at zero for every IT stack. The improvement in the residual distribution can be seen in Fig. 5.6, where the residual peaks at zero. Furthermore, the alignment is expected to improve the resolution of the detector. The smaller width of the residual distribution after the coarse IT alignment illustrates this effect. This alignment does not consider any relative positioning of the TT nor the IT within the LHCb coordinate system. Although this coarse IT alignment improves the residual distribution, it is far away from being precise enough to make a proper TT alignment.

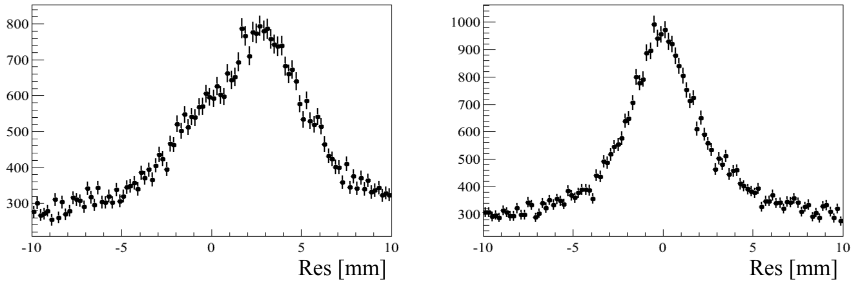

Figure 5.6: The residual of TT hits with respect to extrapolated T-tracks reconstructed before (left) and after (right) a coarse relative alignment of the IT stacks. The smaller width of the coarse alignment distribution clearly shows a better relative alignment.

5.2.2 Magnet-on data

The magnet-on data set provides several ten thousand events. This gives enough tracks to perform a global alignment down to the module level. This global alignment is referred to as the v2.x alignment database. This version includes a pre-alignment of the IT based on collision data preceding the global alignment, to correct for the large IT stack misalignment. The degrees of freedom allowed for the TT are listed in Tab. 5.2. The additional TT alignment aligns for the same TT degrees of freedom.

The resulting alignment values for the parameter T_x for the half-modules showed a remarkable behaviour as shown in Fig. 5.7. The figure shows on the horizontal axis the alignment value for the parameter T_x for the top (black) and bottom (red) TT half-modules with respect to the nominal position. The alignment value T_x of the modules clearly scales with the module x position in the LHCb coordinate system. This scaling behaviour was observed in the global alignment and confirmed in the additional TT alignment. A meticulous search for the cause of this effect, finally, identified a wrong

Elements	Degrees of freedom
full station	$T_xT_yT_z$
modules	T_xR_z

Table 5.2: The degrees of freedom for the TT in the alignment v2.2 using 2009 magnet-on collision data.

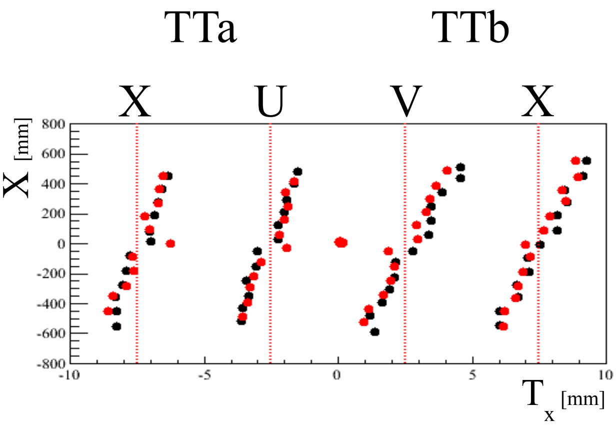

Figure 5.7: The alignment parameter T_x of the TT modules with respect to the nominal position obtained by an alignment using the wrong TT strip pitch. The figure shows on the horizontal axis the alignment values T_x for the top (black) and bottom (red) TT half-modules. A fixed offset, depending on the layer the module belongs to, is added to the alignment value T_x to split up the alignment values of the four different TT layers. The vertical axis represents the nominal x position of the module in the LHCb coordinate system. The alignment value T_x of the modules clearly scales with the module x position .

strip pitch for the TT sensors in the detector description as the source. Correcting the pitch from 183.37 μm to 183.0 μm solved the scaling problem of the TT. The relative alignment between the modules within one layer is mostly based on tracks going through the overlap region of adjacent modules. To compensate for the too large pitch, the modules were pushed apart in x direction. These offsets in x sum up over the several overlap regions resulting in a larger correction the more far away the module is positioned from $x = 0$.

Elements	Degrees of freedom
full station	T_xT_z
layers	T_z
modules	T_xR_z

Table 5.3: The degrees of freedom for the TT used in the alignment database v4.1.

5.3 Alignment with collision data at $\sqrt{s} = 7$ TeV

A powerful tool to improve the relative alignment of subdetectors is the implementation of a mass constraint in the alignment algorithm. The Kalman filter tracks offer the possibility to add vertex informations to the alignment algorithm (see Sec. 4.3.2). The vertex fit can be performed using a mass constraint. The invariant mass is sensitive to the momentum measurement, which again is sensitive to relative misalignments of the subdetectors. The momentum of a particle is given by the curvature of its track in the magnetic field. Constraining known mass resonances to the values in the PDG [72] reduces the curvature bias from misalignments, which results in less biased momentum and invariant mass measurements. Since autumn 2010, the LHC is operating at high energy and luminosity and the collisions provide enough data to reconstruct the J/ψ mass resonance. LHCb collected over half a million J/ψ events in about 5 pb^{-1} of data [74]. Taking the branching ratio of $J/\psi \to \mu^+\mu^-$ of 6 % into account gives a sample of 30000 $J/\psi \to \mu^+\mu^-$ candidates. The LHCb alignment group performed an alignment using the data collected in 2010 and constraining the alignment parameters to the J/ψ mass resulting in the database generation v4.x. The degrees of freedom of the TT included in the v4.x global alignment are listed in Tab. 5.3.

An additional TT alignment starting with the database v4.1 as initial parameters with TT degrees of freedom listed in Tab. 5.1, but excluding T_z for all TT elements shows no more scaling in T_x as can be seen in Fig. 5.8. However, the alignment parameter T_z for the TT station obtained from the global alignment v4.1 reaches a value larger than 1 mm with respect to the nominal position. Also the layers were shifted by approximately 500 μm along z relative to each other. Such large values in T_z are mechanically not possible and are not seen in the survey of the TT. It should be noted that in v4.1, the T_z alignment values of the T-stations were of the order of 5 mm. Performing an alignment with the z position of the VELO floating gives a displacement of the VELO, TT and T-stations along z of more than 1 cm. This corresponds to a displacement of the magnetic field in z direction. A new measurement of the magnetic field in the winter of 2010-2011 confirmed this shift.

The latest global alignment uses this new magnetic field map and 2011 collision data. The obtained T_z alignment values of the OT are all within 1 mm from the survey values and show that the new field map solves the z shift problem of the T-stations.

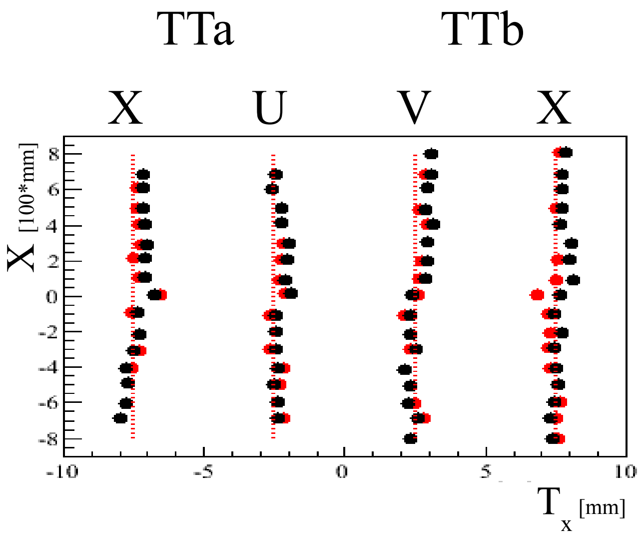

Figure 5.8: Results for the alignment parameter T_x of the TT modules with respect to the nominal position after a TT alignment on top of the global alignment v4.1. The alignment parameters are listed in Tab. 5.3, excluding the alignment for T_z of any element.

Elements	Degrees of freedom
TT modules	$T_x R_z$

Table 5.4: The degrees of freedom for the TT used in the alignment database v5.4.

The degrees of freedom for the TT used in the global alignment v5.4 are listed in Tab. 5.4. The alignment parameters of the TT station and layers were fixed to the survey values. However, a global alignment including degrees of freedom for the TTa layer in T_z still results in shifts of the order of 2 mm.

To better understand these unphysical offsets in T_z an additional alignment of the TT adding degrees of freedom for the TT layers on top of the global alignment v5.4 is performed. First the full TT station and the layers are aligned along the degrees of freedom listed in Tab. 5.5. In a second step, the modules are aligned for the same degrees of freedom as in the global alignment v5.4, listed in Tab. 5.4.

Figure 5.9 shows the performance of the track reconstruction during the alignment iterations of the first step of the TT alignment. The plots show the average track χ^2, the number of tracks and the number of hits used per iteration as a function of the alignment iteration. These three plots have a typical shape if the alignment algorithm works properly. As the alignment algorithm is based on track χ^2 minimisation, the average track χ^2 should drop from one iteration to the other and converge over the

Elements	Degrees of freedom
full TT station	$T_xT_zR_yR_z$
TT layers	$T_xT_zR_yR_z$
TT sides	T_x

Table 5.5: The degrees of freedom for the TT used in the first step of the additional alignment using the alignment database v5.4 as initial alignment parameters.

iterations. During the procedure the detector gets better aligned from one iteration to the other. Hence, more tracks should be found and more hits should be associated to the tracks from one iteration to the other.

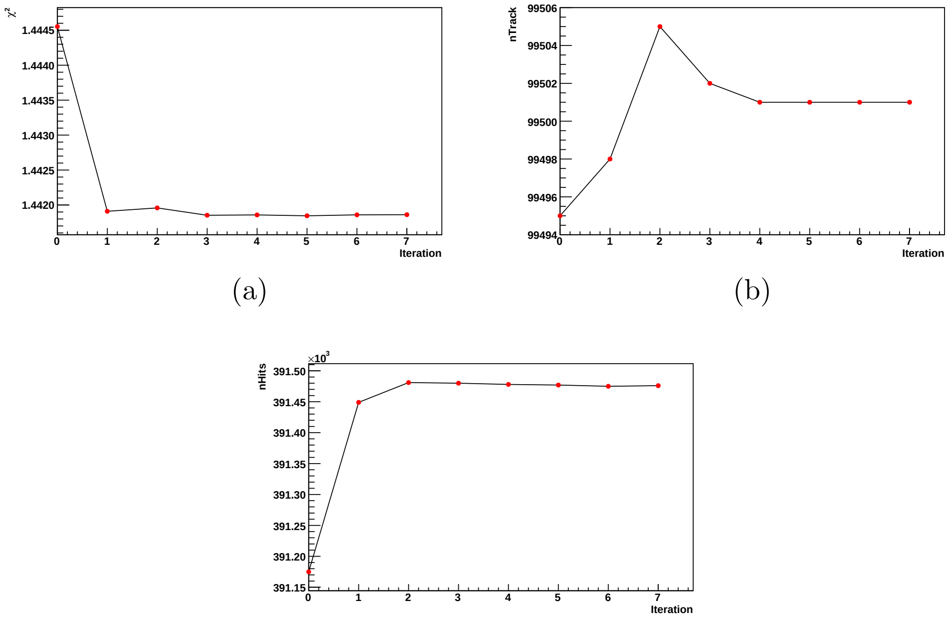

(a) (b)

(c)

Figure 5.9: Track reconstruction performance plots for the first part of the additional TT alignment on top of the global alignment v5.4. The plots show the average track χ^2 per degree of freedom (a), the number of tracks (b) and the total number of hits (c) used for the alignment as a function of the alignment iteration.

The values corresponding to iteration 0 are those obtained using the initial alignment values provided by the alignment database v5.4. Figures 5.10 and 5.11 show the resulting alignment values of the parameter T_x, T_z, R_y and R_z as a function of the

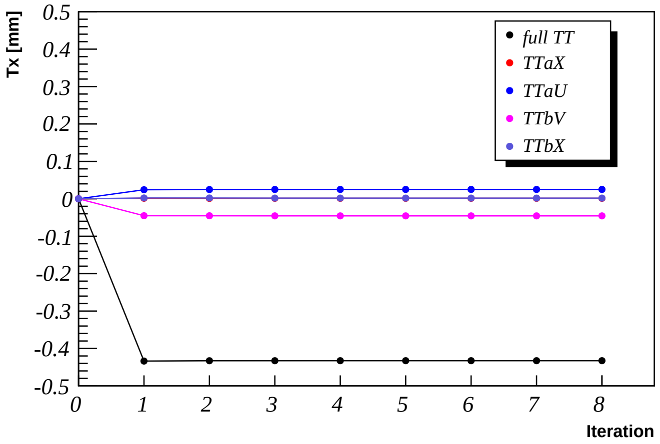

(a)

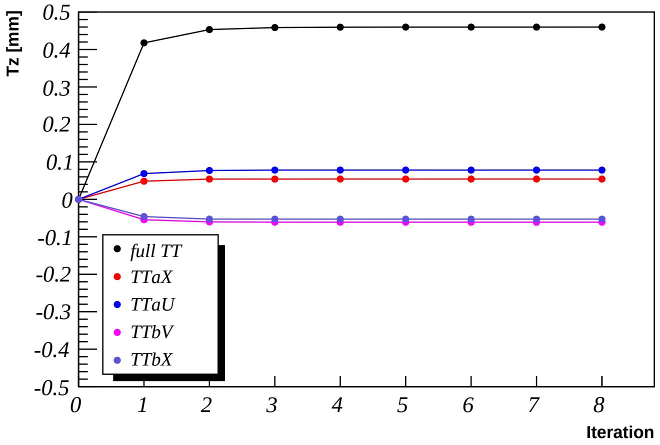

(b)

Figure 5.10: The T_x (a) and T_z (b) alignment values as a function of the alignment iteration of the full TT station and the four layers.

iteration in the first step of the additional TT alignment. All parameters show stable and physically reasonable results.

After the first part of the TT alignment, the second step is performed, aligning the modules in T_x and R_z. The tracking performance for the second part is shown in Fig. 5.12. Only the average track χ^2 shows the expected shape. Nevertheless, compared to the total number of tracks used for the alignment and the total number of hits used, the change over the iterations is very small. The change is less than one per mille.

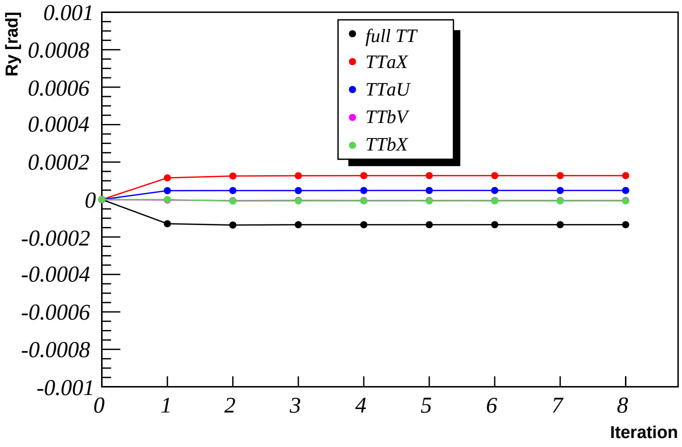

(a)

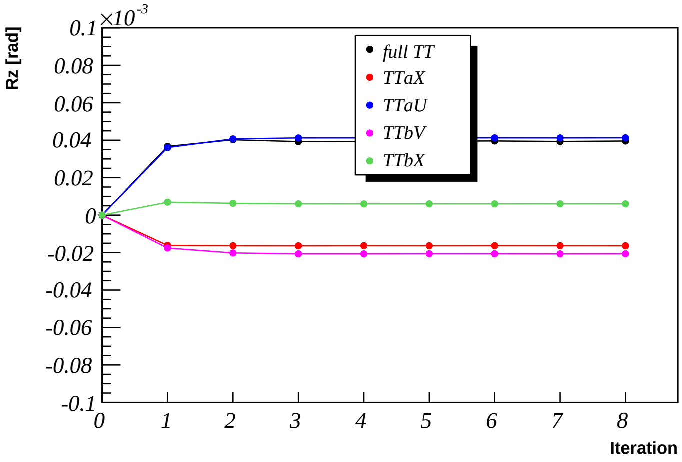

(b)

Figure 5.11: The R_y (a) and R_z (b) alignment values as a function of the alignment iteration of the full TT station and the four layers.

The evolution of the alignment values for the parameters T_x and R_z as a function of the iteration in the second step are shown in Fig 5.13 for the modules of the TTaX layer. The plots for the modules of the other layers can be found in the appendix. The alignment values from the global alignment v5.4 are used as initial alignment parameters for the modules in the second step of the additional TT alignment. These values are included in the first iteration. Both parameters converge after the first iteration and are then stable for all modules. The module with the large value in R_z is the half-module below the beam pipe. The half-modules are mounted only on one side, which makes large values for R_z possible for these modules.

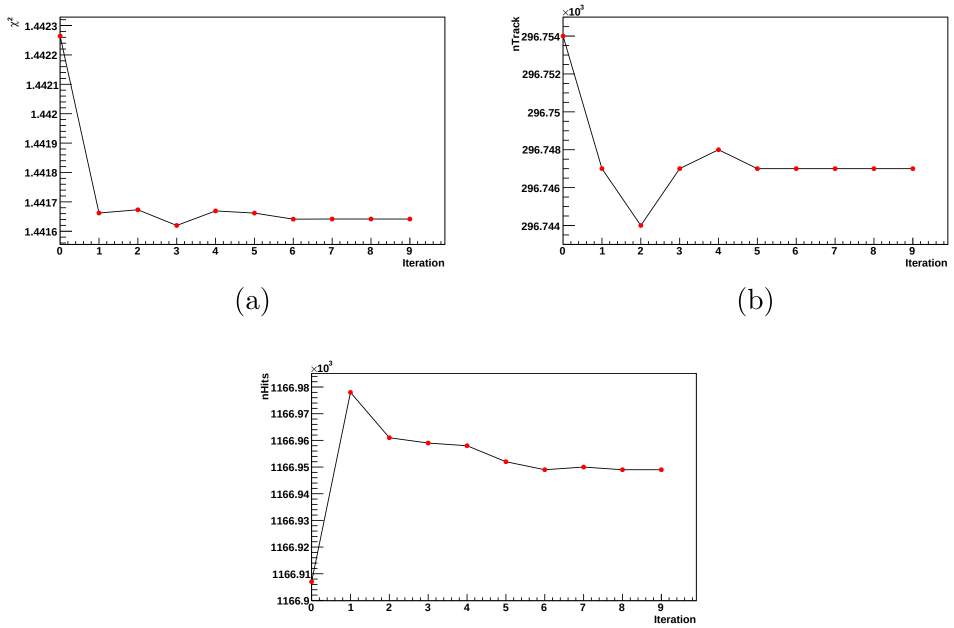

(a) (b)

(c)

Figure 5.12: Tracking performance plots for the second part of the additional TT alignment. The track χ^2 per degree of freedom (a), the number of tracks (b) and the number of hits (c) used for the alignment as a function of the alignment iteration.

Finally, the T_x values of the modules depending on the module position are tested. Figure 5.14 shows no scaling of the modules after the second part of the TT alignment. Furthermore, one can see, that all modules from the A side (positive x values) have T_x alignment values which are larger than zero. This means, that the TT station is not completely closed. This can already be seen in the survey data.

The TT alignment on top of the global alignment v5.4 shows that in general an alignment including the parameters for the TT layers should be possible and stable. The observation of the large z shifts of the TT layers in v5.4 clearly requires a further investigation. The effect of the additional TT alignment on the mass resolution for the $J/\psi \rightarrow \mu^+\mu^-$ resonance is shown in the next section.

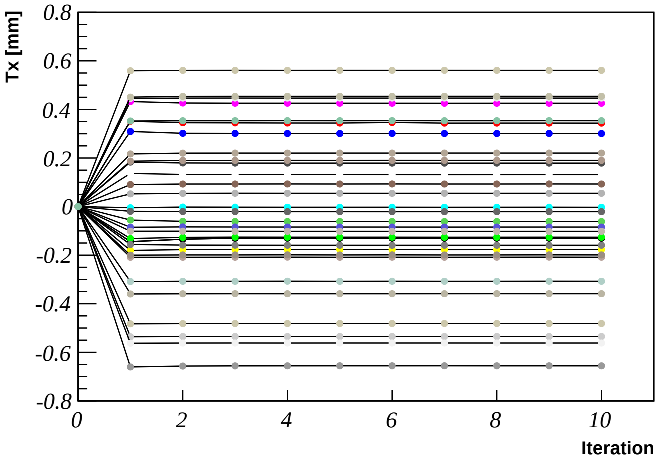

(a)

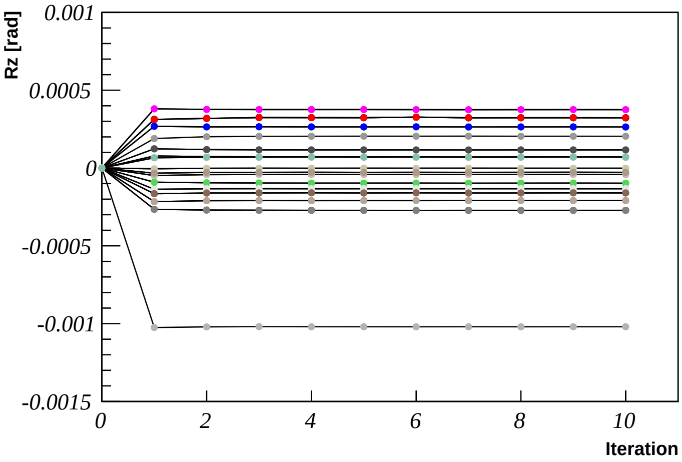

(b)

Figure 5.13: The T_x (a) and R_z (b) alignment values as a function of the alignment iteration of the modules from the TTaX layer. The module with the large alignment value R_z is the half-module below the beam pipe. As half-modules are mounted only on one side, large values for R_z are expected for this kind of modules.

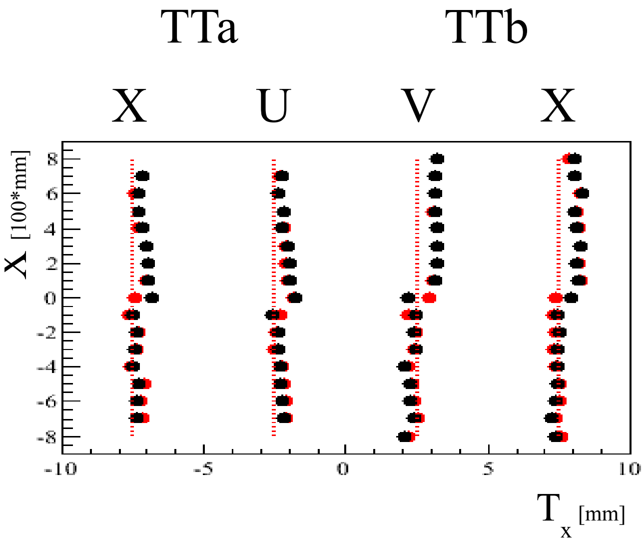

Figure 5.14: The alignment values for the parameter T_x of the TT modules with respect to the nominal position after two additional alignments. First aligning for for the parameters given in Tab. 5.5, and second for the parameters given in Tab. 5.4.

Particle	Variable	Cut
J/ψ	vertex χ^2/NDOF vertex displacement mass window	< 3 > 3 mm upstream 120 MeV/c^2
$\mu^+ \ \mu^-$	Track-χ^2/NDOF p_T isMuonLoose	< 5 > 1000 MeV/c true

Table 5.6: The J/ψ selection cuts.

5.4 Alignment validation

The improvement of the alignment is illustrated by looking at the mass resolution for the $J/\psi \rightarrow \mu^+\mu^-$ resonance. The event selection is based on the *detached J/ψ to muon muon* selection. Table 5.6 lists all selection cuts applied. The two tracks must comply the isMuonLoose[4] criteria.

The plots in Fig. 5.15 show the $\mu^+\mu^-$ invariant mass distribution for a track reconstruction using an alignment based on survey, TED data and cosmic rays on the right-hand side and with the latest alignment database v5.4 on the left-hand side. The fit to the data uses a double Crystal Ball (see Sec. 6.3) for the signal and a second order polynomial for the background. The width of the signal peak gets considerably smaller using the alignment database in the track reconstruction. The effect of the additional TT alignment on top of the global alignment v5.4 is tested in the same way (see Fig. 5.16). The additional alignment shows no significant improvement of the mass resolution. Ignoring TT hits in the track reconstruction reduces the mass resolution dramatically (see Fig. 5.17). The v5.4 alignment database applied on 2011 data shows the same resolution as the v4.1 database applied on 2010 data (see Fig. 5.17). The results of all fits are summarised in Tab. 5.7.

The reconstructed invariant mass resolution is already quite close to the one obtained from simulation studies, which showed a prompt J/ψ mass resolution of about 10 MeV/c^2 [75]. The resolution depends on the selection criteria of the J/ψ. Large momentum cuts for the muons, for example, will reduce the precision of the mass reconstruction due to larger errors on the muon momentum. The mass resolution for prompt J/ψ is slightly better than that for non-prompt J/ψs.

---

[4] For a muon with momentum p_μ with $3 < p_\mu < 6$ GeV/c, hits need to be found in muon station 2 and 3, for $6 < p_\mu < 10$ GeV/c, hits need to be found in muon stations 2,3 and 4 or 5, and for $p_\mu > 10$ GeV/c, hits need to be present in muon stations 2,3,4,5.

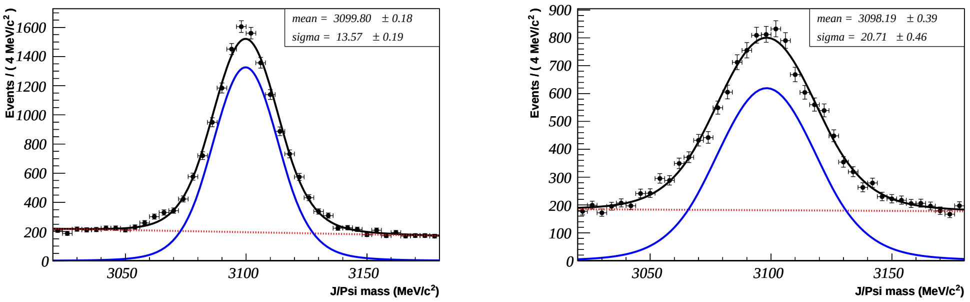

(a) (b)

Figure 5.15: The $\mu^+\mu^-$ invariant mass distribution using the alignment database v5.4 (a) or using an alignment based on survey, cosmic rays and TED data (b). The fit uses a double Crystal Ball for the peak (solid blue) and a second order polynomial for the background (dashed red). The PDG value of the J/ψ mass is 3096.92 ± 0.01 MeV [72].

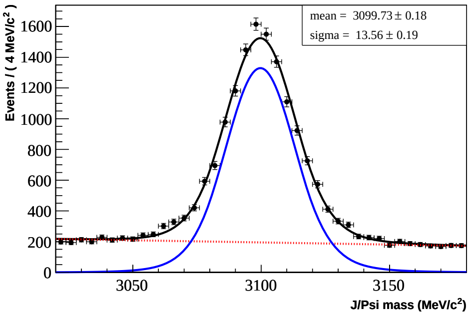

Figure 5.16: The $\mu^+\mu^-$ invariant mass distribution using the additional TT alignment performed after the global alignment v5.4.

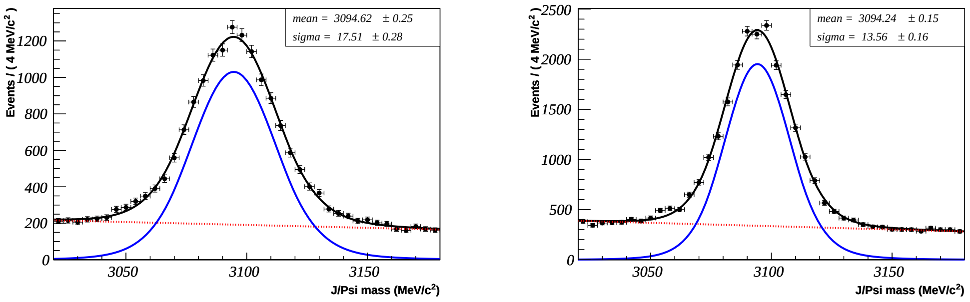

(a) (b)

Figure 5.17: The $\mu^+\mu^-$ invariant mass distribution without TT hits in the track fit using the alignment database v5.4 (a). The invariant mass peak in 2010 data using the alignment database v4.1 (b).

Alignment (data set)	Mean [MeV/c^2]	Width [MeV/c^2]
simulation [75]	3096.3±0.1	9.9±0.1
v4.1 (2010)	3094.2 ± 0.2	13.6 ± 0.2
v5.4 (2011)	3099.8 ± 0.2	13.6 ± 0.2
V5.4 (2011) with additional TT alignment	3099.8 ± 0.2	13.6 ±0.2
v5.4 (2011) without TT hits	3094.6 ± 0.3	17.5 ± 0.3
survey, cosmic rays and TED data (2011)	3098.2±04	20.7±0.5

Table 5.7: The $\mu^+\mu^-$ invariant mass resolution depending on different alignment databases. Including TT hits in the track reconstruction improves the mass resolution by more than 20%.

Chapter 6

Analysis

Angular analysis of particle decays require a good understanding of the detector. Acceptance effects due to the reconstruction and selection of the signal can distort its angular distribution. The LHCb analysis strategy of the $B_d^0 \to K^{*0}\mu^+\mu^-$ decay avails of the accurate Monte Carlo simulation to correct for these effects. The corrections can be derived by comparing the angular distributions at generation level to the distribution after reconstruction and selection. This strategy relies on the fact, that the simulation correctly describes data. Therefore, it is crucial to validate this hypothesis. This validation can be performed using a well known channel, that has larger statistics and the same final state as the signal decay. In the analysis presented in this chapter, the decay channel $B_d^0 \to K^{*0}J/\psi$, where the J/ψ decays in a muon pair, is used as a proxy for the decay $B_d^0 \to K^{*0}\mu^+\mu^-$. The angular distributions of the control channel were accurately measured at the B factories [76, 77].

The Feynman digram of the tree level electroweak decay $B_d^0 \to K^{*0}J/\psi$ is shown in Fig. 6.1. This decay has a higher branching ratio than the decay $B_d^0 \to K^{*0}\mu^+\mu^-$, which is a FCNC. The decay $B_d^0 \to K^{*0}J/\psi$ is used here as a control channel to search for possible discrepancies between Monte Carlo and data. The main difference between the two channels is that in the tree level decay the di-muon mass is fixed to the J/ψ invariant mass. This leads to different momentum spectra for the particles in the final

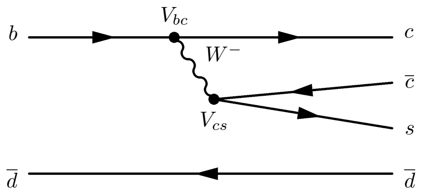

Figure 6.1: Feynman diagram of the colour suppressed B decay to the final state K^{*0} J/ψ. The diagram shows the decay of a $\overline{B^0}$.

state, compared to the FCNC $B_d^0 \to K^{*0}\mu^+\mu^-$ decay. Particle identification, selection and reconstruction efficiencies are in general dependent on the particle momentum. For this reason, the comparison between data and Monte Carlo is here performed as a function of all relevant variables, including the momentum. The branching ratio of the control channel is measured to be $\mathcal{BR}(B_d^0 \to K^{*0}J/\psi) = 1.33 \pm 0.06 \cdot 10^{-3}$, with $\mathcal{BR}(J/\psi \to \mu^+\mu^-) = 5.93 \pm 0.06 \cdot 10^{-3}$ and $\mathcal{BR}(K^{*0} \to K\pi) = 66.5 \pm 0.1$ [72].

The event reconstruction is described in the first section. In the next section, an overview of the simulated and measured data samples is given. Section 6.3 describes the variables used to select the control channel. The comparison between the measured and the simulated data is shown in Sec. 6.4. Finally, some physics observables are measured in the control channel and compared with literature.

6.1 Event reconstruction

Each event contains one or more primary vertices (PV). The PV denotes the three dimensional point within the LHCb interaction region where the two protons collide. The reconstruction of a PV requires a minimum of 6 tracks [78]. The reconstruction of the decay is performed as follow.

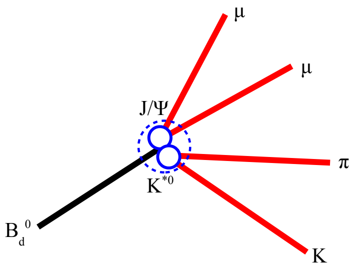

Figure 6.2: A B_d^0 meson decaying to the $K\ \pi\ \mu^+\mu^-$ final state. The kaon and the pion are combined to a K^{*0}, and the two muons are combined to a J/ψ. Finally, these two new particles are fitted into a B_d^0.

To each track a particle hypothesis is assigned using particle identification information. First, good quality tracks of opposite charge and with hits in the muon chambers are combined into a J/ψ candidate. The K^{*0} is built up of a kaon and a pion with opposite charge. Finally, if the J/ψ and the K^{*0} satisfy some loose selection criteria they are combined into a B_d^0 candidate. Note, that the decay $B_d^0 \to K^{*0}\mu^+\mu^-$ uses the same reconstruction algorithm. Figure 6.2 illustrates the decay topology. The secondary vertex (SV) refers to the B_d^0 decay vertex, i.e. the vertex formed by the combination of J/ψ and K^{*0} candidates. Particles are combined in the so-called *stripping selection*, where a loose selection is applied to reduce the number of combinatorial background. The selection cuts are described in Sec. 6.2.2.

6.2 Data Samples

The comparison between simulation and data uses three different samples: the simulated sample, and two measured data samples. The first data sample was taken during the 2010 run and corresponds to 36 pb^{-1}, while the second was taken in 2011 and corresponds roughly to 165 pb^{-1}. The comparison between data and Monte Carlo is done for both data samples.

6.2.1 Monte Carlo

The Monte Carlo sample is produced using the LHCb software package Gauss [40]. The simulation is divided into two independent steps: the generation of the primary event and the interaction between the stable particles and the detector. The first step can be further divided into two steps. First the primary pp collision of the beams is simulated using PYTHIA [22], then the decay of the produced particles are simulated using EvtGen [79]. The simulation code was adapted such that it describes the B production conditions occurring in pp collisions at the LHC.

After the event generation the software simulates the interaction of the particles with the detector. This is based on the GEANT4 package [80]. Further details about the LHCb simulation framework Gauss can be found in Ref. [81].

6.2.2 Measured Data Samples

The 2010 data set corresponds to an integrated luminosity of approximately 36 pb^{-1} of pp-collisions at a centre-of-mass energy of $\sqrt{s} = 7$ TeV. This data was taken between July and November 2010. During that time all detector components were fully operational and in stable conditions. The 2010 sample comprises two equally large subsamples with opposite magnetic field directions. The trigger had to fire in all three levels, i.e. the level zero trigger and the two software high level triggers. The level zero trigger gives a positive decision if a muon with a p_t greater than 1 GeV is found. The high level triggers confirm the level zero decision if a muon candidate and another track have a high transverse momentum. The stripping selection applied to 2010 data has a tight B_d^0 lifetime requirement ($\tau >$1 ps). Additional loose cuts reduce the combinatorial background. All cuts applied in the 2010 stripping selection are listed in Tab. 6.1. One of the most discriminating variables is the impact parameter (IP), which describes the

Particle	Variable	Cut
B_d^0	lifetime τ	> 1 ps
B_d^0, J/ψ and K^{*0}	vertex χ^2	< 9
B_d^0 and K^{*0}	mass window	300 MeV/c^2
μ, K and π	Track-χ^2/NDOF IP-χ^2 δz (ownVertex-PV)	< 5 > 9 > 0 mm
K	DLL$_K$	$>$ -5
μ	isMuonLoose	true

Table 6.1: Stripping selection for 2010 data.

decay topology. The IP of a particle is defined as the distance of closest approach of a track to the PV. Figure 6.3 shows the IP for the pion. Another important variable is the DLL$_K$, which is the particle identification likelihood explained in more details in the next section.

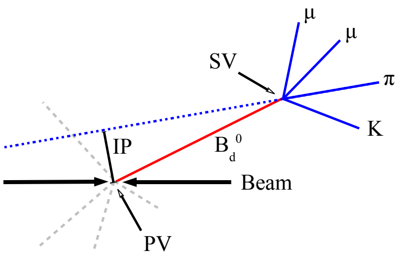

Figure 6.3: The B_d^0 meson originates from the primary vertex (PV) and the secondary vertex (SV) is indicated. The IP of the pion is shown.

The second data sample used in this analysis was taken between February and May 2011. During that period, the complete detector was fully operational. The integrated luminosity for the 2011 data set is approximately 165 pb^{-1} of pp-collisions collected at a centre-of-mass energy of $\sqrt{s} = 7$ TeV. The events are triggered with similar criteria to those used for the 2010 data sample. The level zero trigger searches for a muon with transverse momentum larger than 1 GeV. If an additional track with large transverse momentum is found, the event passes the two high level triggers. The 2011 stripping selection has no requirement on the particle identification on any of the particles. Table 6.2 lists the cuts applied in the 2011 stripping, where additional discriminating variables are used. One of the variable is ϑ, which is the angle between the reconstructed momentum of the B_d^0 and the line passing by the primary and secondary vertices. The angle ϑ is shown in Fig 6.6. Alternatively, the variable DIRA $= cos(\vartheta)$ is used.

Particle	Variable	Cut
B_d^0	B_d mass m$_{B_d}$ DIRA Vertex χ^2 IP χ^2 flight distance χ^2	$4850 < m_{B_d} < 5780$ MeV/c^2 > 0.9999 < 6 < 16 > 121
J/ψ and K^{*0}	flight distance χ^2	> 9
K^{*0}	K^{*0} mass $m_{K^{*0}}$ Vertex χ^2	$600 < m_{K^{*0}} < 2000$ MeV/c^2 < 12
μ, K and π	Track-χ^2/ NDOF IP-χ^2	< 5 > 9
μ	isMuonLoose	True

Table 6.2: Stripping selection for 2011 data.

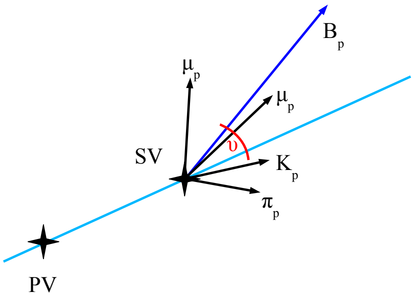

Figure 6.4: The pointing angle is shown. The light blue line pass by the PV and the SV. The dark blue line is the reconstructed momentum of the Bd meson. The pointing angle is the angle between the two lines.

After the stripping, additional selection cuts are applied in order to reduce the background to a negligible amount, before making the comparison between data and Monte Carlo. The data selection is described in details in the next section.

6.3 Discriminating variables and event selection

To have a high purity signal in the data selection, it is necessary to find variables with high discriminating power. The background sample corresponds to the 2010 data sample excluding the events with a reconstructed invariant mass within a window of 100 MeV/c^2 around the B_d^0 mass [72].

The vertex χ^2 distribution shows significant discriminating power (see Fig. 6.5).

However, a loose cut on the vertex χ^2 is applied, since the Monte Carlo does not account for the misalignment present in data. The cut is set at $\chi^2 < 4$ (blue vertical line). The cut on the DIRA variable was set using an educated guess, looking at the distribution of ϑ=acos(DIRA) (see Fig. 6.6). The cut corresponds to $\vartheta < 5$ mrad.

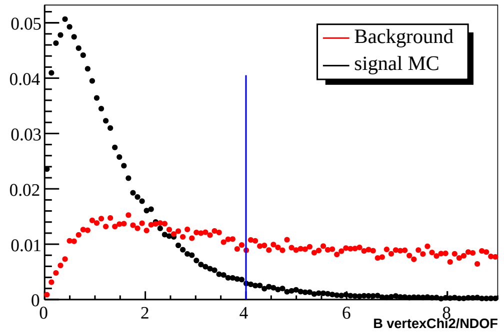

Figure 6.5: The vertex χ^2 distributions for Monte Carlo signal events (black) and sideband events (red). The cut is set to vertex $\chi^2 < 4$ and depicted with the blue vertical line in the plot. All events on the left of the blue line are selected.

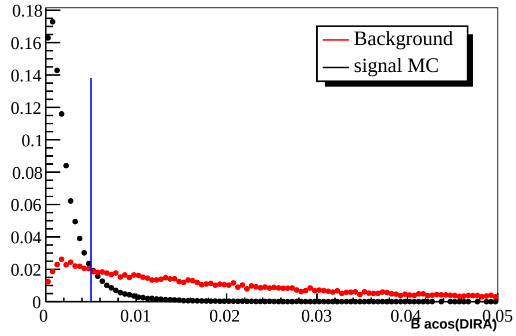

Figure 6.6: The cut is applied at $\vartheta < 5$ mrad (blue vertical line). Events on the left are selected.

For each track the quantity

$$\mathrm{DLL}_K = \Delta\log\mathcal{L}_{K\pi} = \log\mathcal{L}_K - \log\mathcal{L}_\pi \tag{6.1}$$

is computed, where $\mathcal{L}_K$ and $\mathcal{L}_\pi$ are the likelihoods for the pion and kaon hypotheses. A cut on the DLL value classifies the track as a kaon if the likelihood of the kaon hypothesis exceeds the cut value. Figure 6.7 shows the DLL_K distributions for kaons and pions using the 2011 data sample.

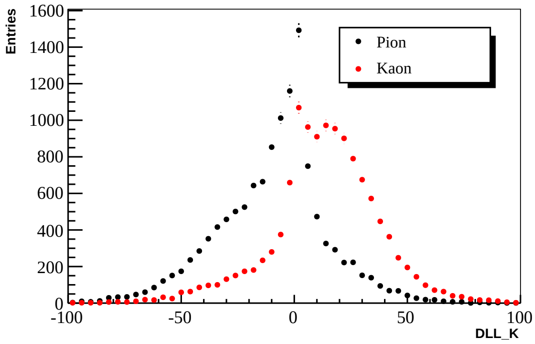

Figure 6.7: The DLL$_K$ distributions of the kaons and pions from the $B_d^0 \to K^{*0} J/\psi$ candidates using 2011 data.

The 2010 data sample has a tight lifetime cut of τ larger than 1 ps. This lifetime cut and the additional loose stripping cuts reduce the background by a considerable amount and a clear peak at the B_d^0 mass is visible already after the stripping selection (see Fig. 6.8).

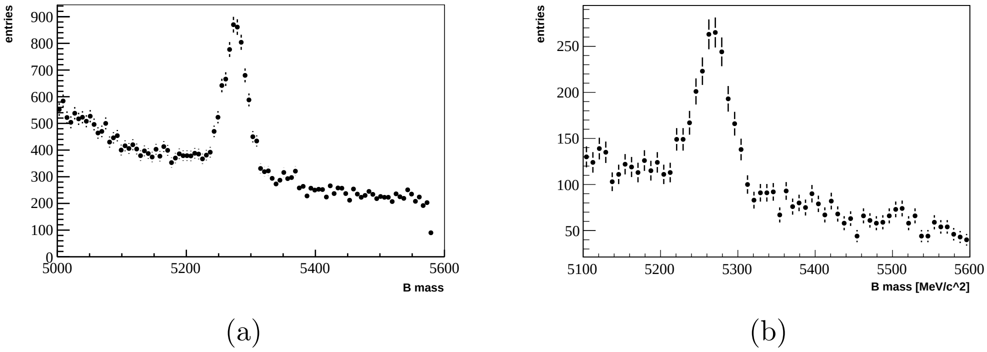

(a) (b)

Figure 6.8: The B_d^0 invariant mass distribution after the stripping selection for the full 2010 (a) and a fraction of the 2011 (b) data sample.

Mass windows are applied to the invariant mass distributions to select the J/ψ and the K^{*0} resonances.

The K^{*0} mass distribution shows a second peak at 800 MeV/c^2 (see Fig. 6.9 (a)). This peak consists of $B_s^0 \to J/\psi\,\phi$ events, where the ϕ decays into two charged kaons and one of them is misidentified as a pion. This can be inferred by Fig. 6.9 (b), which shows the same events, when the kaon hypothesis is applied to both hadrons in the final state. A peak at the ϕ mass is clearly visible. The $B_s^0 \to J/\psi\,\phi$ background is rejected by applying a veto on the events falling in a mass window of 10 MeV/c^2 around the nominal ϕ mass, indicated by the red vertical lines. Figure 6.10 shows the K^{*0} mass distribution after applying the ϕ mass veto. The fit to the data uses a Breit-Wigner distribution

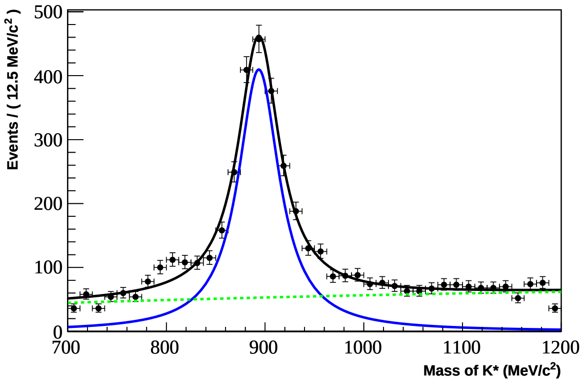

(a)

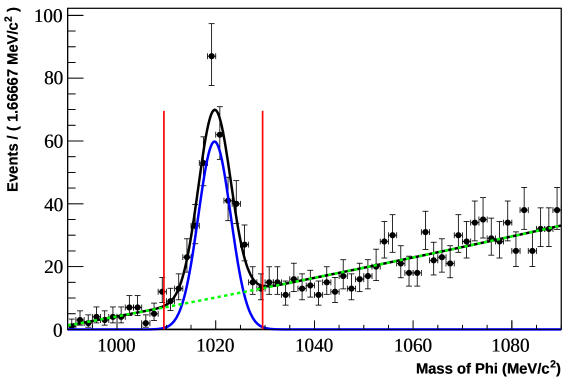

(b)

Figure 6.9: The K^{*0} invariant mass distribution (a) after applying the selection cuts DIRA > 0.9999875 and vertex $\chi^2 < 4$. A closer look at the K^{*0} invariant mass distribution shows a peak at 800 MeV/c^2. The peak is associated to ϕ's from the $\phi \rightarrow KK$ decay, where one of the kaons was misidentified as a pion. The mass distribution assuming that both hadrons in the final state are kaons is shown in (b). There is a clear ϕ contribution from the decay $B_s^0 \rightarrow J/\psi\,\phi$. The vertical red line show the 10 MeV/c^2 ϕ mass exclusion window.

for the signal and a second order polynomial accounting for the background. The K^{*0} mass window is set to 80 MeV/c^2 to improve the purity of the selected candidates.
The mass distribution of the J/ψ (see Fig. 6.11) contains a small fraction of background so an invariant mass window of ± 60 MeV/c^2 was used. The fit uses a double Crystal Ball function for the signal and a first order polynomial for the background.
The Crystal Ball function is a Gaussian core function and a power law tail below a

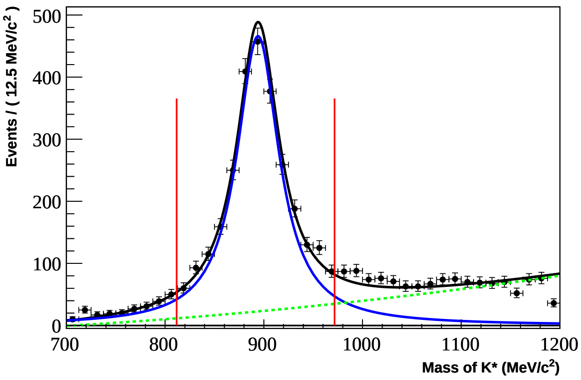

Figure 6.10: The K^{*0} invariant mass distributions after applying the selection cuts DIRA > 0.9999875 and vertex $\chi^2 < 4$ on the B_d^0 and the ϕ mass veto. The fit to the data uses a Breit-Wigner for the data and a second order polynomial for the background. The solid black line shows the sum of the signal (solid blue) and the background (dashed green). The vertical red lines indicate the selected mass region. All events within the window are selected.

Discriminating variable	Cut
B_d^0 DIRA	> 0.9999875
B_d^0 vertexχ^2/NDOF	< 4
J/ψ mass window	60 MeV/c^2
K^{*0} mass window	80 MeV/c^2
ϕ mass veto	10 MeV/c^2

Table 6.3: Selection cuts applied after the 2010 stripping selection.

certain threshold, $\alpha = \frac{x-\overline{x}}{\sigma}$. The double Crystal Ball function is used to model non Gaussian effects. These effects are also visible in Monte Carlo.

The cuts applied to the 2010 data after the stripping selection are summarised in Tab. 6.3. Applying these cuts to the output of the stripping gives a pure signal sample, as can be seen in Fig. 6.12. The fit to the B_d^0 invariant mass uses a double Crystal Ball for the signal and a first order polynomial for the background. The tail of the Crystal Ball is constrained using Monte Carlo.

The results of the fits to the mass distributions of the resonances in the decays $B_d^0 \to K^{*0} J/\psi$ and $\phi \to KK$ are listed in Tab. 6.4. The errors on the mass and σ represent only the statistical errors. The significant shift with respect to the nominal masses are known effects due to misalignment.

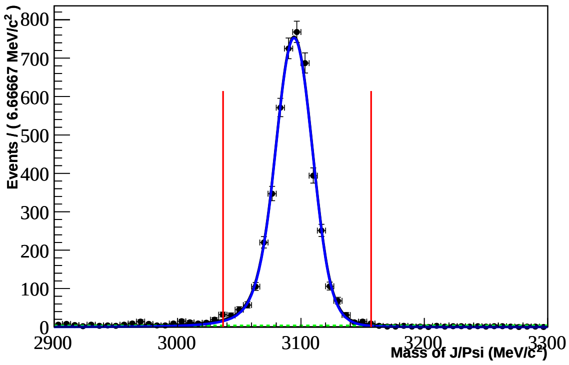

Figure 6.11: The J/ψ invariant mass distributions after applying the selection cuts DIRA > 0.9999875 and vertex $\chi^2 < 4$ on the B_d^0 and the ϕ mass veto. The fit to the data uses a double Crystal Ball function for the data and a first order polynomial for the background. The solid black line shows the sum of the signal (solid blue) and the background (dashed green). The vertical red lines indicate the selected mass region. All events within the window are selected.

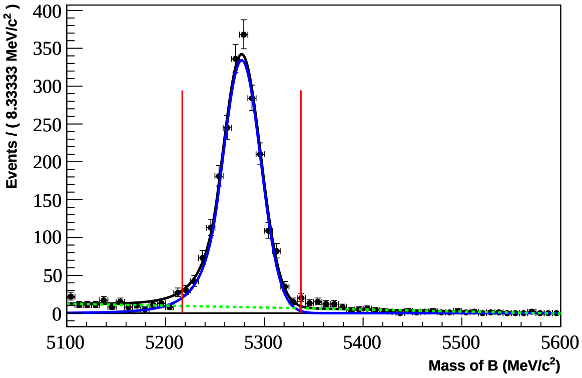

Figure 6.12: The B_d^0 invariant mass distribution obtained for the 2010 data, sample after applying all selection cuts listed in table 6.3. The fit to the distribution (black) uses a double Crystal Ball function for the signal (blue) and a first order polynomial for the background (green). The vertical lines indicate the signal mass window.

Although the 2011 stripping selection has a high signal efficiency a B_d^0 mass peak is already seen after the stripping selection (see Fig. 6.8). The selection applied to the 2011 data sample is similar to the one applied to the 2010 data sample. The cuts are listed in Tab. 6.5. A pure $B_d^0 \to K^{*0} J/\psi$ sample can be easily obtained with tight cuts

Decay	Mass [MeV/c^2]	σ [MeV/c^2]	PDG value [72] [MeV/c^2]
$B_d^0 \to K^{*0} J/\psi$	5277.1 ± 0.5	19.3 ± 0.5	5279.50 ± 0.3
$J/\psi \to \mu^+\mu^-$	3094.5 ± 0.3	14.9 ± 0.2	3096.916 ± 0.011
$K^{*0} \to K\pi$	894.1 ± 0.5	52.0 ± 0.3	891.66 ± 0.26
$\phi \to KK$	1019.8 ± 0.3	3.3 ± 0.2	1019.455 ± 0.020

Table 6.4: Results of the fits of the invariant masses of the B_d^0, J/ψ, K^{*0} and ϕ resonances.

Discriminating variable	Cut
B_d^0 DIRA	> 0.9999875
J/ψ vertex χ^2	< 6
J/ψ mass window	40 MeV/c^2
K^{*0} vertex χ^2	< 6
K^{*0} mass window	60 MeV/c^2
ϕ mass veto	10 MeV/c^2
K DDL$_K$	> -5

Table 6.5: Selection cuts applied after the 2011 stripping selection.

on the masses of the resonances J/ψ and K^{*0}. The B_d^0 invariant mass distribution of the selected events in the 2011 data sample is shown in Fig. 6.13. The fitted curve consists of a double Crystal Ball for the signal and a first order polynomial for the background.

The results of the fits to the invariant mass distributions of the B_d^0 candidates are summarised in Tab. 6.6 for the 2010 and 2011 data samples. The difference between the two sets of data is due to the different running conditions and to differences in the reconstruction software. The errors account only for the statistical uncertainties. The events within a mass window of 60 MeV/c^2 around the measured B_d^0 mass are selected for the comparison between data and Monte Carlo presented in the next section. This corresponds roughly to a 3σ window. The background fraction after the selection, in both 2010 and 2011 data samples, is smaller than 10%.

Parameter	Value	
Data set	2010	2011
mean	5277.1 ± 0.5 MeV/c^2	5271.1 ± 0.3 MeV/c^2
sigma	19.3 ± 0.5 MeV/c^2	17.6 ± 0.2 MeV/c^2
signal	2061 ± 49	5425 ± 78

Table 6.6: The results of the fit to the invariant mass of the B_d^0 candidates obtained in 2010 and 2011 data samples.

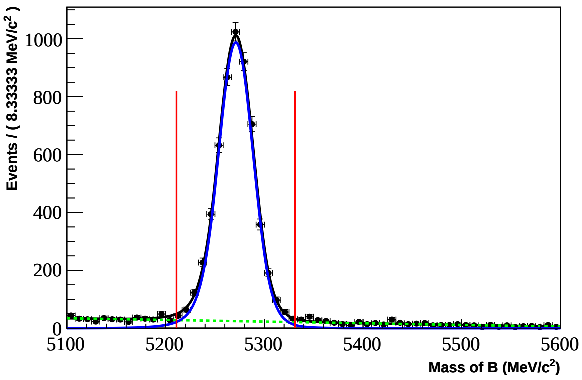

Figure 6.13: The B_d^0 invariant mass distribution for the 2011 data sample, after applying the selection cuts. The vertical lines indicate the signal mass window.

Some events can have more than one candidate passing the selection requirements. To avoid double counting, the event with the smaller vertex χ^2 is selected. Furthermore, events can have multiple candidates with the identical vertex χ^2 due to the possibility of misidentifying both hadrons: kaon and pion. In this case, the event with the larger DLL_K value for the kaon candidate is selected. This will be discussed in more details in the following section.

6.4 Comparison between data and Monte Carlo

Data and Monte Carlo are compared for several variables. The momentum p, the pseudo-rapidity η and the impact parameter for the B_d^0, the pion, the kaon and the two muons are analysed.

A significant discrepancy is seen for the impact parameter of the B_d^0 to the primary vertex as shown in Fig. 6.14 (a). On the left the impact parameter distributions are plotted for data (red) and Monte Carlo (black). The plots on the right show the distribution of the ratio between the data and the Monte Carlo. Since the B_d^0 comes from the PV, its impact parameter peaks at zero, thus it is sensitive to misalignments of the Vertex Locator which cause the differences between data and Monte Carlo. To correct for this discrepancy, the x and y positions of the measured point closest to the beam are smeared in the Monte Carlo. This parameter is extracted by using an independent sample of tracks coming from the PV [82].
The distributions of the B_d^0 impact parameter before and after the smearing are shown in Fig. 6.14. The track smearing leads to a better agreement between data and Monte Carlo. The χ^2 obtained from the fit of a flat line to the ratio of the two distributions is also shown. The improvement in the agreement between Monte Carlo and data is

clearly visible from the plot.

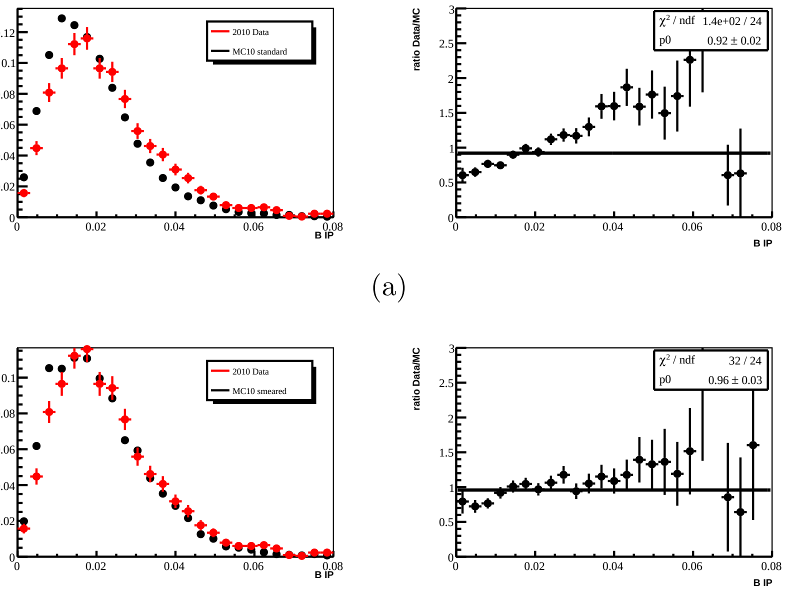

(a)

(b)

Figure 6.14: The B_d^0 impact parameter distribution before the track smearing (a) and after the track smearing (b). The plots on the left show the distributions for 2010 data in red and Monte Carlo in black. The plots on the right show the ratio $\frac{Data}{MC}$.

The particles in the final state (kaon, pion and muons) come from the secondary vertex and their impact parameter distribution is dominated by the lifetime of the B_d^0. Therefore, the effect of the IP smearing is not visible for these particles and no discrepancy between data and Monte Carlo is expected. The pion impact parameter distributions for data and Monte Carlo are shown in Fig. 6.15 before and after applying the IP smearing correction.

Another known discrepancy between data and simulation comes from the different PID likelihood distributions for pions and kaons (see Fig. 6.16). The particle identification is a key parameter for the offline signal selection. As the PID depends on the momentum of the hadron, different PID distributions in data and Monte Carlo will distort in a different way the momentum distributions if a cut on the DDL_K is applied.

The hadron particle identification relies mostly on the two RICH detectors. The hadron PID is calibrated with data, with a tag an probe technique using the decay $D^{*+} \to D^0(\to K^+\pi^-)\pi^+$ [83]. For the muons the decay $B^+ \to J\psi(\to \mu\mu)K^+$ is used. The calibration is performed as a function of the particle momentum p, the pseudorapidity η and the track multiplicity n_{track}. Using the PID efficiency, the data events

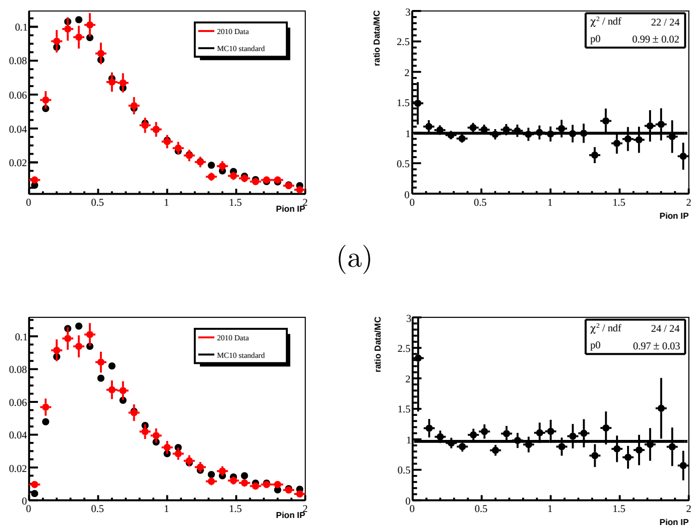

(a)

(b)

Figure 6.15: The pion impact parameter distribution for the 2010 data sample before the track smearing (a) and after the track smearing (b).

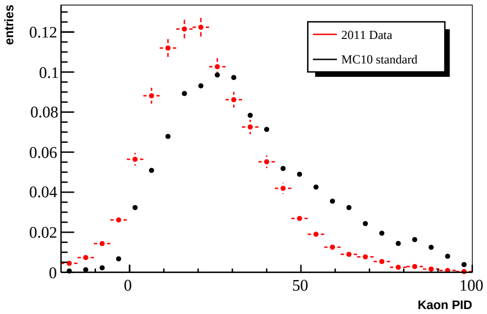

Figure 6.16: Kaon particle identification DLL_K distribution for the 2011 data (red) and the Monte Carlo (black) of the kaon.

are weighted. The weight factor ϵ is

$$\begin{aligned} N_{measured} &= N_{true} \cdot \epsilon_K \cdot \epsilon_{sel1} + N_{true} \cdot (1-\epsilon_K) \cdot \epsilon_{sel2} \\ \Rightarrow \epsilon &= \frac{N_{true}}{N_{measured}} = \frac{1}{\epsilon_K \cdot \epsilon_{sel1} + (1-\epsilon_K) \cdot \epsilon_{sel2}} \ , \end{aligned} \tag{6.2}$$

where $N_{measured}$ is the number of measured $B_d^0 \to K^{*0} J/\psi$ events, N_{true} the *true* number of $B_d^0 \to K^{*0} J/\psi$ decays inside the detector acceptance and ϵ_K the kaon PID efficiency. The term $(1-\epsilon_K)$ is the misidentification efficiency, ϵ_{sel1} and ϵ_{sel2} are the

K^{*0} invariant mass selection efficiency for the correct pion and kaon hypotheses and for the case when the pion and the kaon are swapped. Note that the pion efficiency is 100% since no PID cut is applied to pion candidates.

To validate the PID calibration, the weighted data are compared to Monte Carlo events with no PID requirements. Since the pion momentum was found to be the most sensitive to PID cuts, the comparison between data and Monte Carlo is shown for this observable before and after the PID correction (see Fig. 6.17). The agreement between data and Monte Carlo improves after the correction is applied. Tighter DLL_K cuts select a cleaner event sample and thus lead to a better agreement between data and Monte Carlo (see appendix B.1).

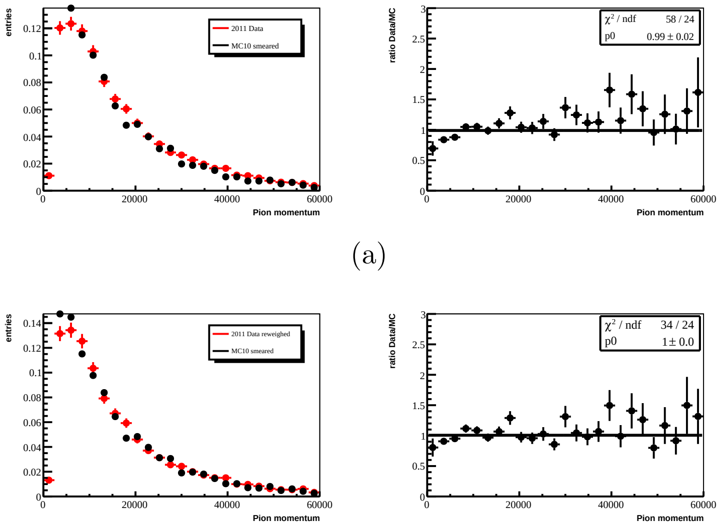

(a)

(b)

Figure 6.17: The pion momentum distribution in the 2011 data sample before the PID efficiency correction (a) and after the PID efficiency correction (b).

After correcting the Monte Carlo for the misalignment and weighting the data with the PID efficiencies several parameters are compared for the particles B_d^0, K, π and μ. The comparison is done for the 2010 and 2011 data samples. This section shows the result obtained for the 2011 data sample. The results for the 2010 data sample are shown in the appendix B.2. The comparison plots in the following are all made with a kaon likelihood cut of $\mathrm{DLL}_K > 5$. An excellent agreement is found between data and simulation for all the particles in all the observables.

The probability of swapping the pion and the kaon in the signal selection can be computed using the misidentification efficiency extracted from the D^* calibration sample and weighting this by using the signal momentum, taken from Monte Carlo.

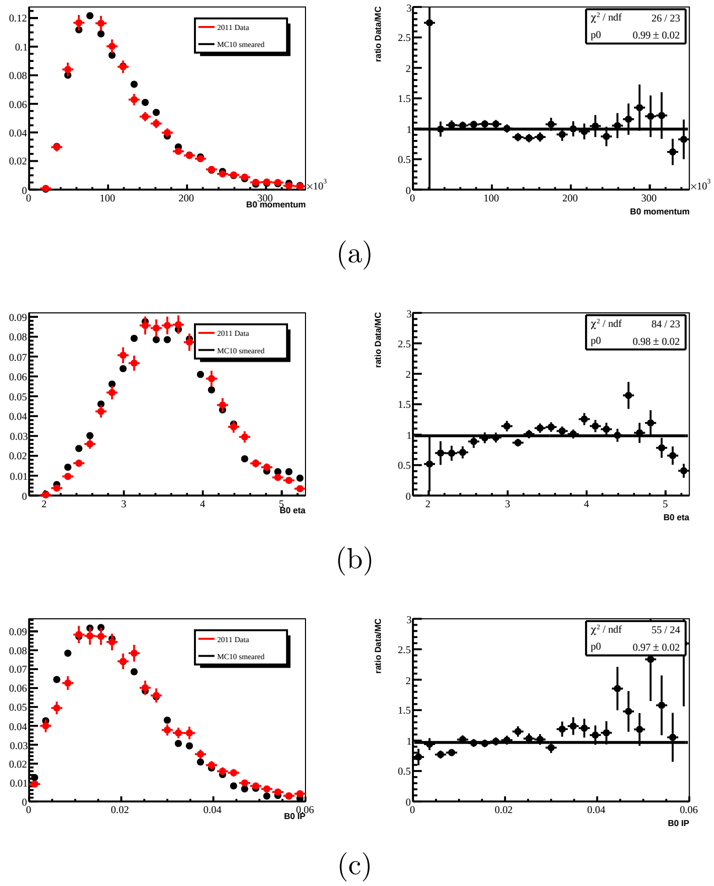

(a)

(b)

(c)

Figure 6.18: Comparison between data and Monte Carlo for the 2011 data for (a) the momentum, (b) the pseudo-rapidity η and (c) the impact parameter to the primary vertex of the B.

The rates obtained are listed in Tab. 6.7.
This probability can also be calculated using an alternative, data driven, approach. When the kaon and pion are swapped, this will lead to an event which has two different B_d^0 candidates with exactly the same vertex χ^2. One candidate where the kaon and the pion are correctly identified and a second one, where the kaon and the pion are swapped. To obtain the misidentification rate one has to count the number of events with two existing candidates with the same vertex χ^2 and divide it by the total number of events. Since this study would require a low background level, tight cuts are applied on the invariant masses of the B_d^0, J/ψ and the K^{*0}. This selection would also reduce the rate of events where the pion and the kaon are misidentified, therefore only the combination having the kaon candidate with the largest DLL_K is required to pass the mass cuts. This counting method was done using the 2010 data sample. The result is given in Tab. 6.7.

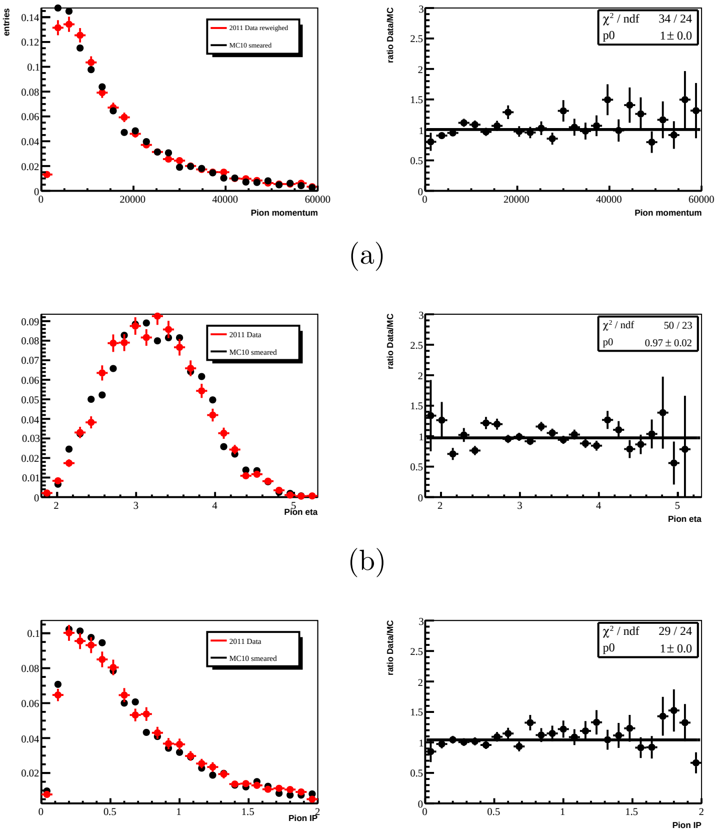

(a)

(b)

(c)

Figure 6.19: Comparison between data and Monte Carlo for the 2011 data for (a) the momentum, (b) the pseudo-rapidity η and (c) the impact parameter to the primary vertex of the Pion.

A good agreement is found between the two independent methods as a function of the DLL_K (see Tab. 6.7).

This study shows that the Monte Carlo simulation has the required accuracy, once corrected for the know discrepancies with data, to evaluate the acceptance effects. This has been a crucial ingredient for the analysis technique described in Ref. [12] and was used for the first LHCb measurement and world-best measurement of the decay $B_d^0 \to K^{*0}\mu^+\mu^-$.

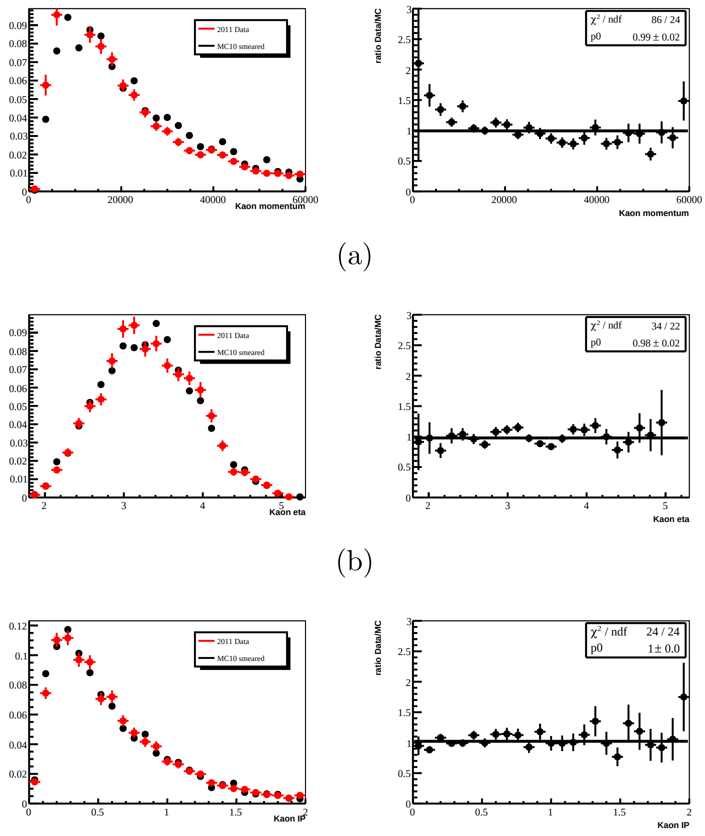

(a)

(b)

(c)

Figure 6.20: Comparison between data and Monte Carlo for the 2011 data for (a) the momentum, (b) the pseudo-rapidity η and (c) the impact parameter to the primary vertex of the Kaon.

DLL_K cut value	Monte Carlo based method	Data 2010 based method
-5	23.7 ± 4.2 %	19.2 ± 0.7 %
0	12.6 ± 2.1 %	11.3 ± 0.6 %
5	5.5 ± 1.1 %	5.5 ± 0.5 %
10	2.4 ± 0.5 %	3.2 ± 0.4 %
15	1.3 ± 0.3 %	2.0 ± 0.3 %

Table 6.7: The misidentification rate as a function of the DLL_K. The independent methods show an excellent agreement.

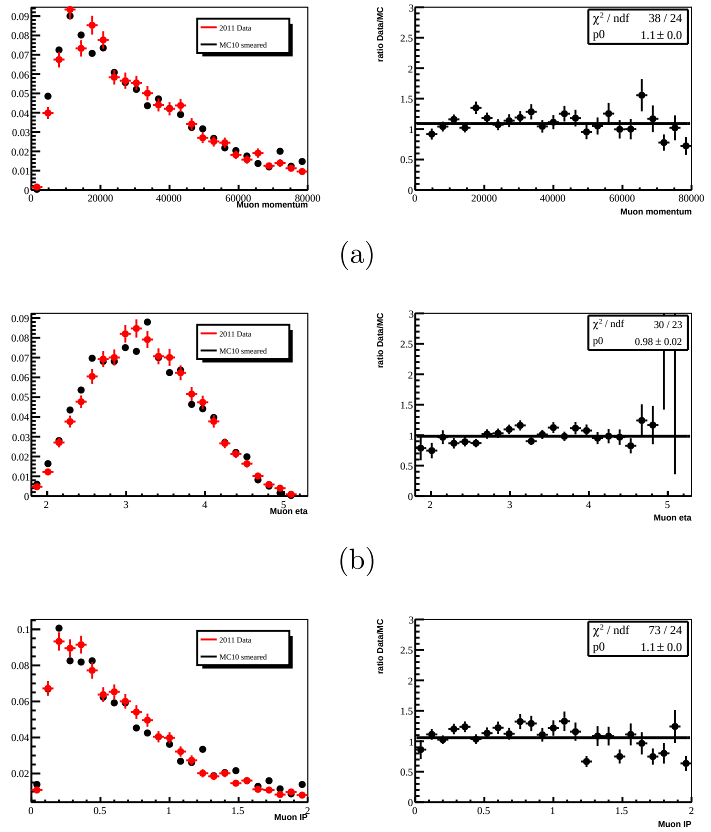

(a)

(b)

(c)

Figure 6.21: Comparison between data and Monte Carlo for the 2011 data for (a) the momentum, (b) the pseudo-rapidity η and (c) the impact parameter to the primary vertex of the Muon.

6.5 Physics observables in the $B_d^0 \to K^{*0}J/\psi$ decay

The selection described in Sec. 6.3, but with a looser B_d^0 vertex cut ($\chi^2 < 9$), gives a yield of 2640 ± 57 for the 2010 data sample. The invariant mass distribution of the B_d^0 candidates is shown in Fig. 6.22. The fit to the signal uses a double Crystal Ball function (solid blue). The background is modelled with a linear function (dashed green) and a component accounting for partially reconstructed decays (solid red) [84]. The selection efficiency is $\epsilon_{sel} = 0.61\%$, as measured using the Monte Carlo. The total $b\bar{b}$ cross section has been measured in LHCb using semileptonic decays [85]. The consistency between this data sample and with previous measurements can be checked using the formula:

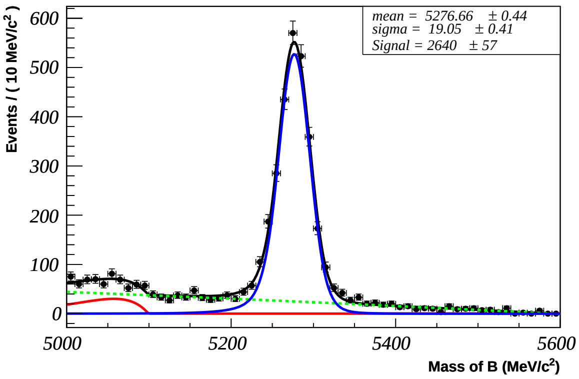

Figure 6.22: The invariant B mass distribution for a sample of 34.8 pb^{-1} integrated luminosity. The fit to the signal uses a double Crystal Ball function (solid blue). The background model uses a linear function (dashed green) and an additional component accounting for partially reconstructed decays (solid red).

$$\sigma(pp \to b\bar{b}X) = \frac{N(b\bar{b} \to K^{*0}J/\psi)}{2 \cdot f_d \cdot \mathcal{L} \cdot \epsilon_{tot} \cdot \mathcal{BR}(total)} \,, \tag{6.3}$$

where

$$\mathcal{BR}(total) = \mathcal{BR}(J/\psi \to \mu\mu) \cdot \mathcal{BR}(K^{*0} \to K^{\pm}\pi^{\mp}) \cdot \mathcal{BR}(B_d^0 \to K^{*0}J/\psi) \,, \tag{6.4}$$

$N(b\bar{b} \to K^{*0}J/\psi)$ is the number of measured $B_d^0 \to K^{*0}J/\psi$ events, $f_d = 0.403 \pm 0.011$ is the production rate of B_d^0 mesons [72], $\mathcal{L}$ is the integrated luminosity and ϵ_{tot} is the total efficiency. The cross section is measured to be

$$\sigma(pp \to b\bar{b}X) = 294 \pm 31 \ \mu\text{b} \,. \tag{6.5}$$

The error is dominated by the relative error on the luminosity of 10%. The statistical errors on the number of $B_d^0 \to K^{*0}J/\psi$ events and on f_d are both considered, while the other errors are neglected. The result is in good agreement with the result presented in Ref. [85] of $\sigma(pp \to b\bar{b}X) = 284 \pm 20 \pm 49$ μb.

Using the 2011 data sample, A_{FB} is measured for one q^2 bin corresponding to the J/ψ invariant mass. The cuts $\mathrm{p_T}(K) > 1.5$ GeV and B_d^0 vertex $\chi^2 < 4$ are applied additionally to the cuts listed in Tab. 6.5 to reduce the background to a negligible amount. Furthermore, the events are corrected by the acceptance efficiency derived from Monte Carlo studies. The Forward-Backward Asymmetry is derived by counting the number of forward and backward events and is measured to be

$$A_{FB}(B_d^0 \to K^{*0}J/\psi) = 0.002 \pm 0.018 \ . \tag{6.6}$$

This result is in perfect agreement with SM prediction ($A_{FB} = 0$) and previous measurements. To test the full procedure of the extraction of A_{FB} with samples of similar size to what is expected in the FCNC $B_d^0 \to K^{*0}\mu^+\mu^-$, the total sample is divided into smaller samples of 300 events. The A_{FB} and its errors are calculated for each subsample, as shown in Fig. 6.23. The distribution of A_{FB} is gaussian and compatible with the expected value $A_{FB} = 0$. The pull on the A_{FB} (see Fig. 6.23) is unbiased and with unitary sigma, proving the robustness of the whole procedure.

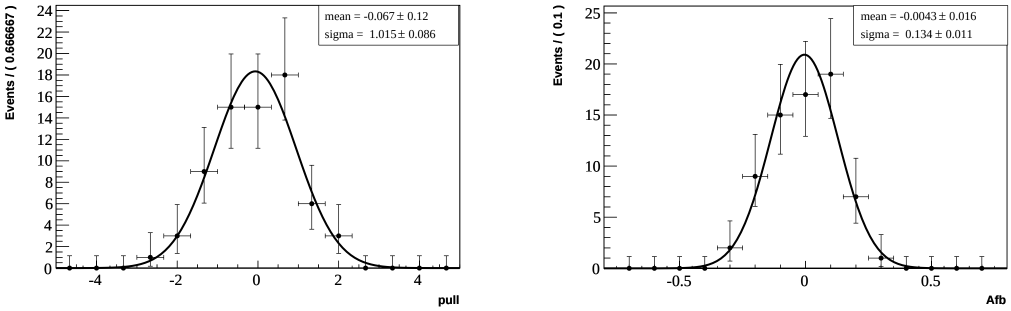

Figure 6.23: Distribution of A_{FB} (right) and the pull on A_{FB}. The distribution are obtained with subsamples of $B_d^0 \to K^{*0}J/\psi$ decay with 300 events each.

In summary the decay $B_d^0 \to K^{*0}J/\psi$ has been used to test the accuracy of the LHCb simulation. Once corrected for known discrepancies, i.e. the impact parameter resolution and the PID likelihood, the Monte Carlo agrees well with data. In light of these results the simulation has been used to compute the efficiency, necessary to extract some physics observables in the $B_d^0 \to K^{*0}J/\psi$ decay. The production cross section has been measured and found in good agreement with previous measurements. The A_{FB} has been found in excellent agreement with the SM expectation. Moreover, the large sample of $B_d^0 \to K^{*0}J/\psi$ has been divided in smaller subsamples and a pull distribution on the A_{FB} is obtained, using data. This showed that the extraction of the A_{FB} is unbiased and that the errors are correctly estimated.

Chapter 7

Summary

The design of the Tracker Turicensis was finalised in 2004. All parts of the TT within the LHCb acceptance have been modelled to a high level of detail in the detector description. The data obtained from surveys during and after the construction of the TT were implemented in the conditions database.

LHCb performed several alignment tests using data collected before the first *pp* collisions, i.e. cosmic rays and TED data. The alignment tests showed that the detector was surveyed well both during and after assembly. However, the first alignment tests including the TT could only be performed for the first time with data from collision at a low centre-of-mass energy $\sqrt{s} = 900$ MeV, collected in November 2009.
When the LHC reached a centre-of-mass energy of $\sqrt{s} = 7$ TeV in autumn 2010, global alignments including a mass constraint on the J/ψ invariant mass became possible. The global alignment significantly improved the resolution of the detector. For instance, the mass resolution of the $J/\psi \to \mu^+\mu^-$ decay went from 20.7 ± 0.5 MeV/c^2 using a pre-collision alignment to 13.6 ± 0.2 using the 2011 global alignment.
Several alignment tests on top of the global alignment have been performed for the TT. These tests helped to understand the output obtained from the global alignment and to gain experience that contributed to the results of the global alignment.
Although a lot of progress had been made in the global and the TT alignment, this task is far from complete. Problems remain, such as large non physical translations in z for the TT layers, which are not understood yet and require further investigations.

The analysis presented in this thesis used two different data samples. The 2010 data sample collected in autumn 2010 corresponding to an integrated luminosity of approximately 36 pb^{-1} and the 2011 data sample collected from February until May 2011 with an integrated luminosity of approximately 165 pb^{-1}.

The acceptance correction used in the angular analysis of the flavour changing neutral current decay $B_d^0 \to K^{*0}\mu^+\mu^-$ is based on simulation. The agreement between data and Monte Carlo was demonstrated using the tree level electroweak decay

$B_d^0 \to K^{*0} J/\psi$. After corrections for known discrepancies, i.e. the impact parameter resolution and the particle identification likelihood, data and Monte Carlo showed a good agreement for the 2010 and 2011 data samples.

As a cross check the $b\bar{b}$ cross section has been estimated, using the 2010 data sample, to be

$$\sigma(pp \to b\bar{b}X) = 294 \pm 31\ \mu\mathrm{b}\ . \tag{7.1}$$

This result does not include systematic uncertainties but is in good agreement with previous measurements.

A further cross check is the measurement of A_{FB} for one q^2 bin corresponding to the J/ψ mass using the decay $B_d^0 \to K^{*0} J/\psi$. Using the 2011 data sample and counting the forward and backward $B_d^0 \to K^{*0} J/\psi$ events, A_{FB} is measured to

$$A_{FB}(B_d^0 \to K^{*0} J/\psi) = 0.002 \pm 0.018\ , \tag{7.2}$$

taking only the statistical error into account. This measurement is in excellent agreement with the Standard Model prediction ($A_{FB} = 0$).

Appendix A

Evolution of the alignment offsets

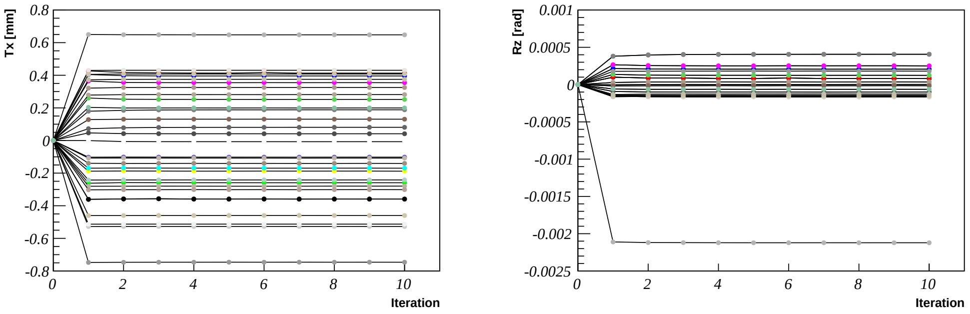

(a) (b)

Figure A.1: The T_x (a) and R_z (b) alignment offsets as a function of the alignment iteration of the modules from the TTaU layer. Surprisingly, the module with the large R_z correction is not a half-module, but a full module located next to the beam pipe.

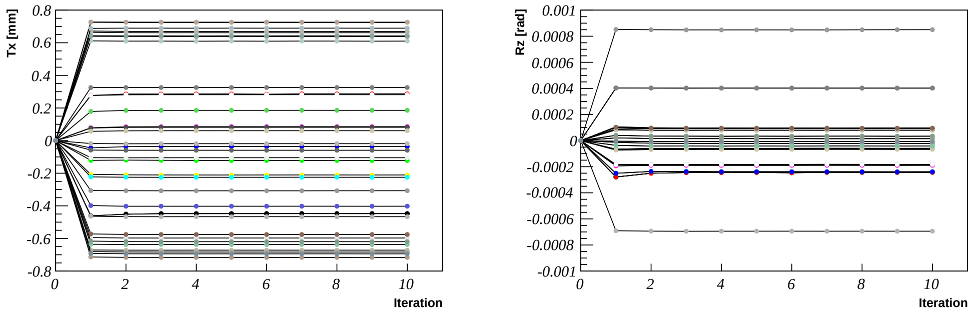

(a) (b)

Figure A.2: The T_x (a) and R_z (b) alignment offsets as a function of the alignment iteration of the modules from the TTbV layer.

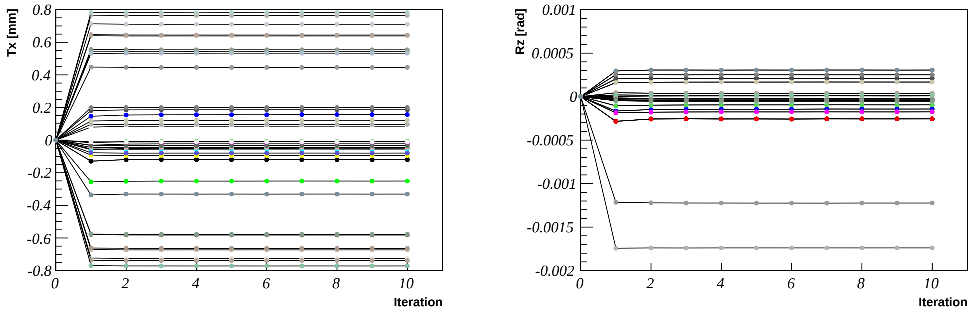

(a) (b)

Figure A.3: The T_x (a) and R_z (b) alignment offsets as a function of the alignment iteration of the modules from the TTaU layer. The two modules with a large alignment parameter R_z are the half-modules above and below the beam pipe. As half-modules are mounted only on one side, large values for R_z are possible these modules.

Appendix B

B.1 Dependency of the reweighing on the DLL$_K$ cut

The agreement between data and Monte Carlo depends on the DLL$_K$. For higher cuts the correction works better. The figures B.1 shows the effect of the correction for DLL$_K$ > -5, figure B.2 for DLL$_K$ > 5 and B.3 for DLL$_K$ > 10. The agreement between data and Monte Carlo improves for larger cuts.

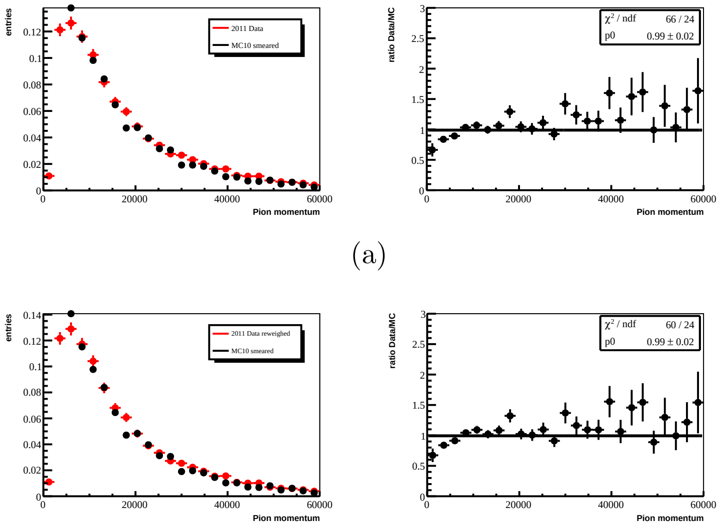

(a)

(b)

Figure B.1: The pion momentum distribution for the 2011 data sample before the PID efficiency correction (a) and after the PID efficiency correction (b) for a DDL$_K$ > -5 cut.

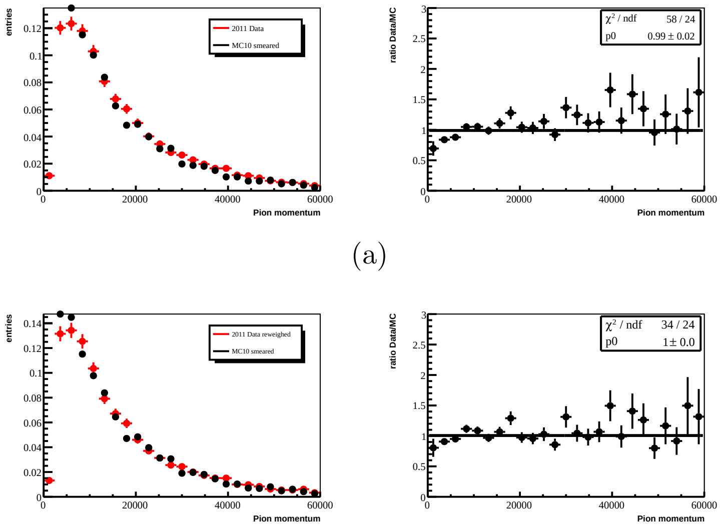

(a)

(b)

Figure B.2: The pion momentum distribution for the 2011 data sample before the PID efficiency correction (a) and after the PID efficiency correction (b) for a DDL$_K > 5$ cut.

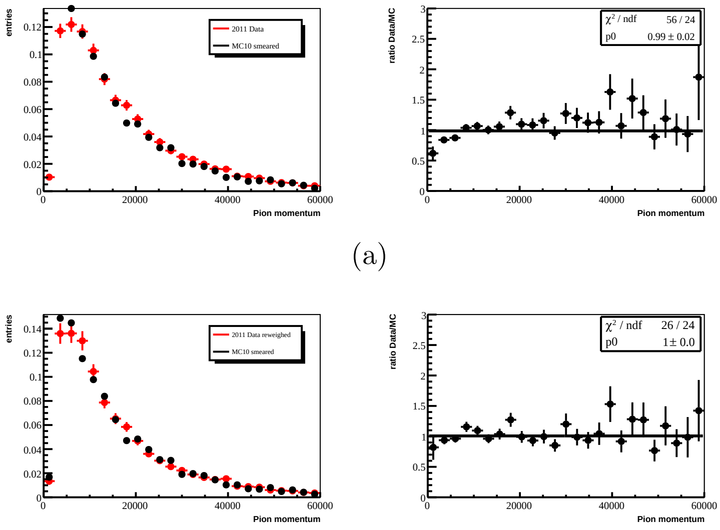

(a)

(b)

Figure B.3: The pion momentum distribution for the 2011 data sample before the PID efficiency correction (a) and after the PID efficiency correction (b) for a DDL$_K > 10$ cut.

B.2 Comparison between 2010 data and Monte Carlo

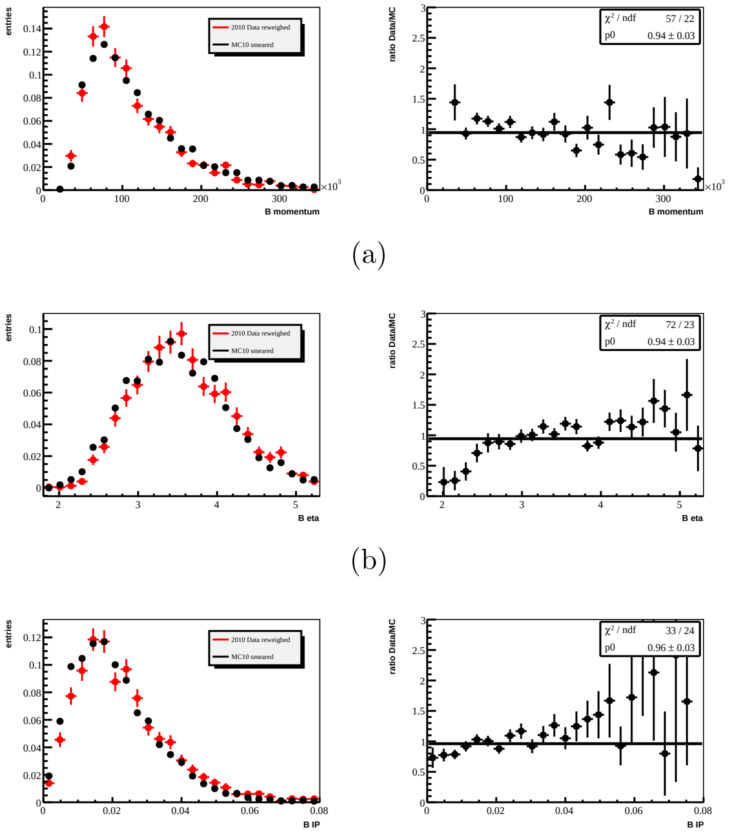

(a)

(b)

(c)

Figure B.4: Comparison between data and Monte Carlo for the 2010 data for (a) the momentum, (b) the pseudo-rapidity η and (c) the impact parameter to the primary vertex of the B.

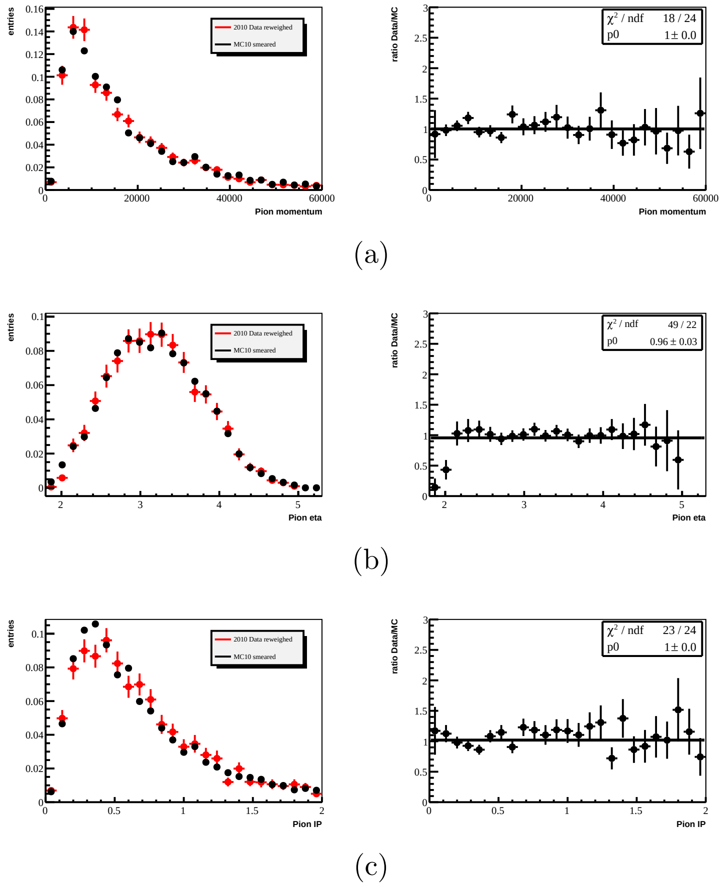

(a)

(b)

(c)

Figure B.5: Comparison between data and Monte Carlo for the 2010 data for (a) the momentum, (b) the pseudo-rapidity η and (c) the impact parameter to the primary vertex of the Pion.

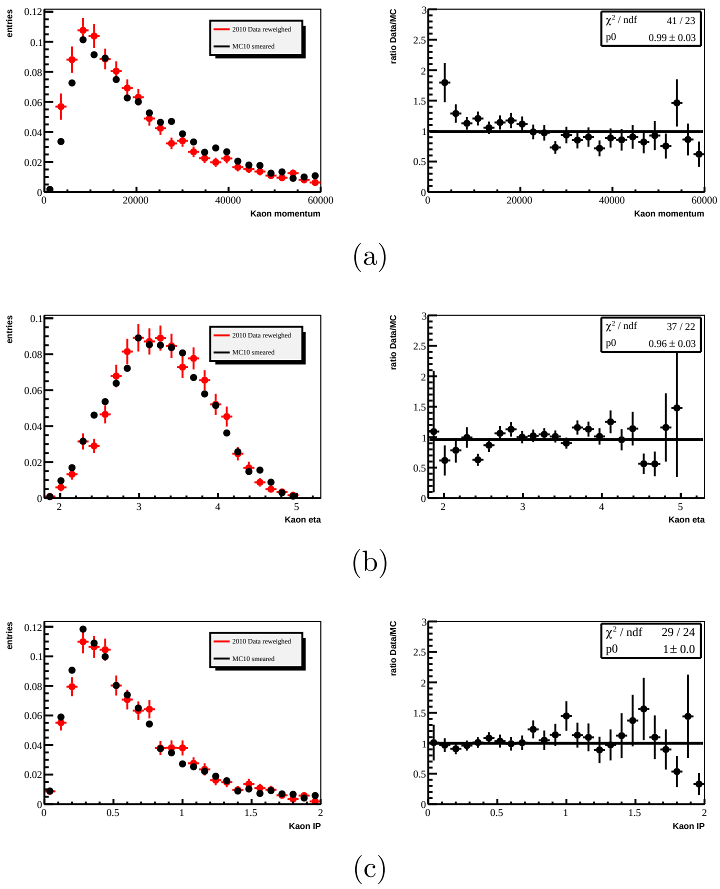

Figure B.6: Comparison between data and Monte Carlo for the 2010 data for (a) the momentum, (b) the pseudo-rapidity η and (c) the impact parameter to the primary vertex of the Kaon.

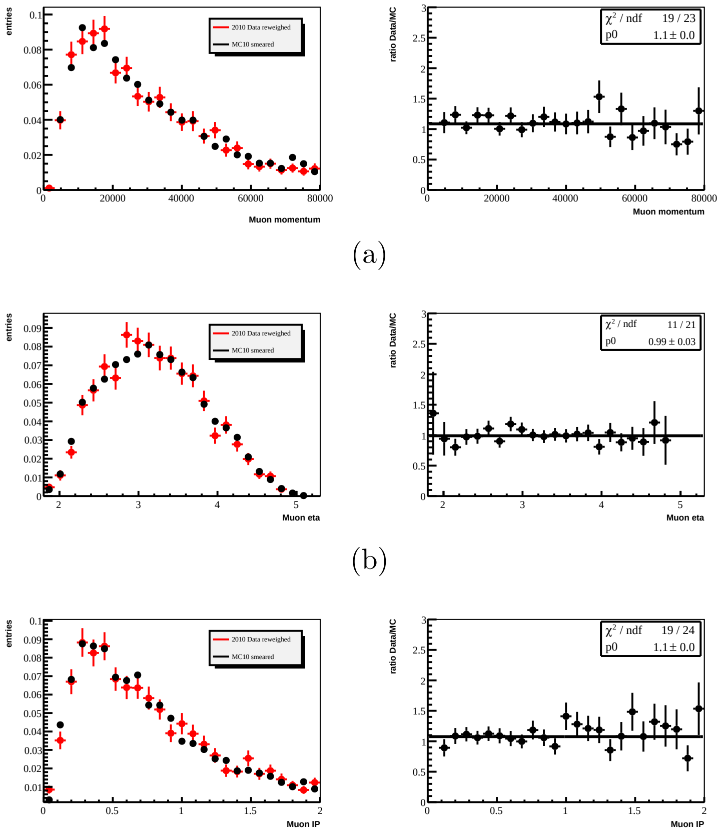

(a)

(b)

(c)

Figure B.7: Comparison between data and Monte Carlo for the 2010 data for (a) the momentum, (b) the pseudo-rapidity η and (c) the impact parameter to the primary vertex of the Muon.

Bibliography

[1] F. Halzen and A. D. Martin, *Quark and Leptons* (John Wiley and Sons, 1984).

[2] N. Cabibbo, *Unitary Symmetry and Leptonic Decays*, Phys. Rev. Lett., **10**:531, 1963.

[3] M. Kobayashi and T. Maskawa, *CP-violation in the Renormalizable Theory of Weak Interaction*, Progress of Theoretical Physics, **49(2)**:652, 1973.

[4] S. L. Glashow, J. Iliopoulos and L. Maiani, *Weak Interactions with Lepton-Hadron Symmetry*, Phys. Rev. D, **2**:1285, 1970.

[5] F. Jansen, N. Serra, G. Y. Smit and N. Tuning, *Determination of the forward-backward asymmetry in the decay $B^0 \to K^*\mu\mu$ with an unbinned counting analysis*, Tech. Rep. CERN-LHCb-2009-003, CERN, 2009.

[6] U. Egede and W. Reece, *Performing the full angular analysis of $\overline{B}_d \to \overline{K}^{*0}\mu^+\mu^-$ at LHCb*, Tech. Rep. CERN-LHCb-2008-041, CERN, 2008.

[7] U. Egede, *Angular correlations in the $\overline{B}_d \to \overline{K}^{*0}\mu + \mu-$ decay*, Tech. Rep. CERN-LHCb-2007-057, CERN, 2007.

[8] W. Altmannshofer, P. Ball, A. Bharucha, A. J. Buras *et al.*, *Symmetries and Asymmetries of $B \to K^*\mu^+\mu^-$ Decays in the Standard Model and Beyond*, JHEP, **0901**:019, 2009.

[9] B. Aubert, R. Barate, M. Bona, D. Boutigny *et al.*, *Measurements of branching fractions, rate asymmetries, and angular distributions in the rare decays $B \to K = \ell^+\ell^-$ and $B \to K^*\ell^+\ell^-$*, Phys. Rev. D, **73**:092001, 2006.

[10] J.-T. Wei, P. Chang, I. Adachi, H. Aihara *et al.*, *Measurement of the Differential Branching Fraction and Forward-Backward Asymmetry for $B \to K^*l^+l^-$*, Phys. Rev. Lett., **103**:171801, 2009.

[11] T. Aaltonen *et al.*, *Measurements of the Angular Distributions in the Decays $B \to K^(*)\mu^+\mu^-$ at CDF*, Tech. Rep. FERMILAB-PUB-11-364-PPD, 2011.

[12] The LHCb Collaboration, *Angular analysis of $B^0 \to K^{*0}\mu^+\mu^-$*, 2011, LHCb-ANA-2011-022.

[13] C. Bobeth, G. Hiller and D. van Dyk, *More Benefits of Semileptonic Rare B Decays at Low Recoil: CP Violation*, JHEP, **07**:067, 2011.

[14] ATLAS collaboration, *ATLAS: technical proposal for a general-purpose pp experiment at the Large Hadron Collider at CERN*, LHC Tech. Proposal (CERN, Geneva, 1994).

[15] CMS collaboration, *CMS, the Compact Muon Solenoid : technical proposal*, LHC Tech. Proposal (CERN, Geneva, 1994).

[16] ALICE collaboration, *ALICE: Technical proposal for a Large Ion collider Experiment at the CERN LHC*, LHC Tech. Proposal (CERN, Geneva, 1995).

[17] L. R. Evans and P. Bryant, *The LHC machine*, J. Instrum., **3**, 2008.

[18] L. Evans, *The Large Hadron Collider: a marvel of technology*, Fundamental Sciences (EPFL Press, Lausanne, Switzerland, 2009).

[19] LHCb Collaboration, *LHCb : Technical Proposal*, Tech. Proposal (CERN, Geneva, 1998).

[20] T. Virdee, *The LHC project: The accelerator and the experiments*, Nucl. Instrum. Meth., **623(1)**:1, 2010, 1st International Conference on Technology and Instrumentation in Particle Physics.

[21] J. van Tilburg, *Track simulation and reconstruction in LHCb*, Ph.D. thesis, Vrije Univ. Amsterdam, 2005, CERN-THESIS-2005-040.

[22] T. Sjostrand, S. Mrenna and P. Z. Skands, *PYTHIA 6.4 Physics and Manual*, JHEP 0605, 2006.

[23] R. Aaij *et al.*, *Prompt* K_s^0 *production in pp collisions at* $\sqrt{s} = 0.9\ TeV$, Physics Letters, **B(693)**:69, 2010.

[24] A. A. Alves *et al.*, *The LHCb Detector at the LHC*, J. Instrum., **3**:S08005, 2008.

[25] R. Antunes-Nobrega *et al.*, *LHCb reoptimized detector design and performance: Technical Design Report*, Technical Design Report LHCb (CERN, Geneva, 2003).

[26] P. R. Barbosa-Marinho *et al.*, *LHCb VELO (VErtex LOcator): Technical Design Report*, Technical Design Report LHCb (CERN, Geneva, 2001).

[27] P. De Simone, *Operation and performances of the LHCb Experiment.*, 2011, CERN-LHCb-PROC-2011-039.

[28] J. Gassner, F. Lehner and S. Steiner, *The mechanical design of the LHCb silicon Trigger Tracker*, CERN-LHCb-2004-110, 2004.

[29] P. R. Barbosa-Marinho *et al.*, *LHCb inner tracker: Technical Design Report*, Technical Design Report LHCb (CERN, Geneva, 2002).

[30] P. R. Barbosa-Marinho *et al.*, *LHCb outer tracker: Technical Design Report*, Technical Design Report LHCb (CERN, Geneva, 2001).

[31] J. M. Amoraal, *Alignment with Kalman filter fitted tracks and reconstruction of $B_s^0 \to J/\psi\phi$ decays*, Ph.D. thesis, Amsterdam, Vrije U., 2011, CERN-THESIS-2011-011.

[32] L. B. A. Hommels, *The LHCb Outer Tracker Detector Design and Production*, Tech. Rep. CERN-LHCb-2005-014, CERN, 2005.

[33] S. Amato *et al.*, *LHCb RICH: Technical Design Report*, Technical Design Report LHCb (CERN, Geneva, 2000).

[34] S. Amato *et al.*, *LHCb calorimeters: Technical Design Report*, Technical Design Report LHCb (CERN, Geneva, 2000).

[35] P. R. Barbosa-Marinho *et al.*, *LHCb muon system: Technical Design Report*, Technical Design Report LHCb (CERN, Geneva, 2001).

[36] *LHCb muon system: addendum to the Technical Design Report*, Technical Design Report LHCb (CERN, Geneva, 2003).

[37] *LHCb muon system: second addendum to the Technical Design Report*, Technical Design Report LHCb (CERN, Geneva, 2005).

[38] S. Amato *et al.*, *LHCb magnet: Technical Design Report*, CERN-LHCC-2000-007 (CERN, Geneva, 2000).

[39] P. Mato, *GAUDI-Architecture design document*, Tech. Rep. LHCb-98-064, CERN, 1998.

[40] LHCb Collaboration, *LHCb Computing Technical Design Report*, CERN-LHCC-2005-019, 2005.

[41] M. Clemencic, H. Degaudenzi, P. Mato, S. Binet *et al.*, *Recent developments in the LHCb software framework gaudi*, J. Phys.: Conf. Ser., **219**, 2010.

[42] S.Ponse, I. Belyaev, P. M. Vila and A. Vallasi, *Detector description framework in LHCb*, arXiv:physics/0306089, 2003.

[43] R. Chytracek *et al.*, *The LHCb detector description framework*, Proc. of CHEP 2000, 2000.

[44] M. Needham and A. Wenger, *Material budget calculation for the LHCb TT station*, CERN-LHCb-2005-020, 2005.

[45] M. Needham and D. Volyanksyy, *Updated geometry description for the LHCb trigger tracker*, CERN-LHCb-2006-032, 2006.

[46] C. Salzmann and J. van Tilburg, *TT detector description and implementation of the survey measurements*, CERN-LHCb-2008-061, 2008.

[47] J. Gassner, F. Lehner and S. Steiner, *The production, assembly and testing of the LHCb Silicon Trigger Tracker.*, CERN-LHCb-2004-109, 2004.

[48] D. Hutchcroft, *VELO Pattern Recognition*, Tech. Rep. CERN-LHCb-2007-013, CERN, 2007.

[49] O. Callot, *FastVelo, a fast and efficient pattern recognition package for the Velo*, Tech. Rep. CERN-LHCb-PUB-2011-001, CERN, 2011.

[50] O. Callot and M. Schiller, *PatSeeding: A Standalone Track Reconstruction Algorithm*, Tech. Rep. CERN-LHCb-2008-042, CERN, 2008.

[51] M. Needham, *The Tsa Reconstruction Framework*, Tech. Rep. CERN-LHCb-2007-037, CERN, 2007.

[52] O. Callot and S. Hansmann-Menzemer, *The Forward Tracking: Algorithm and Performance Studies*, Tech. Rep. CERN-LHCb-2007-015, CERN, 2007.

[53] M. Needham, *Performance of the Track Matching*, Tech. Rep. CERN-LHCb-2007-129, CERN, 2007.

[54] M. Needham and J. van Tilburg, *Performance of the track matching*, Tech. Rep. CERN-LHCb-2007-020, CERN, 2007.

[55] O. Callot, M. Kucharczyk and M. Witek, *VELO-TT track reconstruction*, Tech. Rep. CERN-LHCb-2007-010, CERN, 2007.

[56] O. Callot, *Downstream Pattern Recognition*, Tech. Rep. CERN-LHCb-2007-026, CERN, 2007.

[57] R. Kalman, *A new approach to linear filtering and predictions problems.*, Journal of Basic Engineering, **35**, 1960.

[58] R. Fruhwirth, *Application of Kalman Filtering to track and vertex fitting*, Nucl. Instrum. Meth., **A(262)**:444, 1987.

[59] W. Hulsbergen, *The global covariance matrix of tracks fitted with a Kalman filter and an application in detector alignment*, Nucl. Instrum. Meth., **A(600)**:471, 2009.

[60] L. Nicolas, *Alignment of the LHCb Tracking Stations and Selection of* $X(3872)$ *and* $Z(4430)^{\pm}$ *in pp Collisions at 14TeV*, Ph.D. thesis, Lausanne, EPFL, 2009, CERN-THESIS-2009-129.

[61] W. Baldini *et al.*, *LHCb Alignment Strategy*, Tech. Rep. CERN-LHCb-2006-035, CERN, 2006.

[62] M. Gersabeck, *Initial LHCb VELO Alignment from Survey Measurements*, Tech. Rep. CERN-LHCb-2008-044, CERN, 2008.

[63] G. Conti and F. Blanc, *IT Survey Measurements: Analysis and Implementation in the LHCb Software*, Tech. Rep. CERN-LHCb-2008-069, CERN, 2008.

[64] M. Deissenroth, *Software Alignment of the LHCb Outer Tracker Chambers*, Ph.D. thesis, Heidelberg, Universität Heidelberg, 2010, CERN-THESIS-2010-063.

[65] S. Borghi *et al.*, *First spatial alignment of the LHCb VELO and analysis of beam absorber collision data*, Nucl. Instrum. Meth., **A618**:108, 2010.

[66] M. Needham, *First alignment of the Inner Tracker using data from the TI-8 sector test*, Tech. Rep. CERN-LHCb-2009-030, CERN, 2009.

[67] S. Viret, C. Parkes and M. Gersabeck, *Alignment procedure of the LHCb Vertex Detector*, Nucl. Instrum. Meth., **A(596)**:157, 2008.

[68] M. Gersabeck, C. Parkes and S. Viret, *LHCb VELO software alignment - Part III: the alignment of the relative sensor positions*, Tech. Rep. CERN-LHCb-2007-138, CERN, 2008.

[69] S. Viret, C. Parkes and D. Petrie, *LHCb VELO software alignment, Part I: the alignment of the VELO modules in their half boxes*, Tech. Rep. CERN-LHCb-2005-101, CERN, 2005.

[70] S. Viret, C. Parkes and M. Gersabeck, *LHCb VELO software alignment - Part II: the alignment of the VELO detector-halves*, Tech. Rep. CERN-LHCb-2007-067, CERN, 2007.

[71] V. Blobel, *Software alignment for tracking detectors*, Nucl. Instrum. Meth., **A(566)**:5, 2006.

[72] K. Nakamura *et al.*, *(Particle Data Group)*, J. Phys., **G 37(075021)**, 2010.

[73] L. Nicolas and M. Needham, *Alignment of the Inner Tracker Stations Using First Data*, Tech. Rep. CERN-LHCb-PUB-2009-012, CERN, 2009.

[74] R. Aaij, B. Adeva, M. Adinolfi, C. Adrover *et al.*, *Measurement of J/ψ production in pp collisions at $\sqrt{s} = 7$ TeV*, European Physical Journal C, **71**:1, 2011.

[75] J. M. Amoraal, *The $J/\psi \to \mu\mu$ selection*, Tech. Rep. LHCb-2007-052. CERN-LHCb-2007-052, CERN, 2007.

[76] B. Aubert, M. Bona, D. Boutigny, Y. Karyotakis *et al.*, *Measurement of decay amplitudes of $B \to J/\psi K^*$, $\psi(2s)K^*$, and $\chi_{c1}K^*$ with an angular analysis*, Phys. Rev. D, **76**:031102, 2007.

[77] R. Itoh, Y. Onuki, K. Abe, K. Abe *et al.*, *Studies of CP Violation in $B \to J/\psi K^*$ decays*, Phys. Rev. Lett., **95**:091601, 2005.

[78] M. Krasowski, M. Kucharczyk, W. Männer, G. Polok and M. Witek, *Primary vertex reconstruction*, Tech. Rep. LHCb-2007-011. CERN-LHCb-2007-011, CERN, 2007.

[79] D. J. Lange, *The EvtGen particle decay simulation package*, Nucl. Instrum. Meth., **A(462)**:152, 2001.

[80] The GEANT4 Collaboration, S. Agostinelli *et al.*, *GEANT4, a simulation toolkit*, Nucl. Instrum. Meth., **A(506)**:250, 2003.

[81] I. Belyaev *et al.*, *Handling of the generation of primary events in Gauss, the LHCb simulation framework*, LHCb-PROC-2010-056, 2010.

[82] The LHCb Collaboration, *Measurement of Δm_s in the decay $B_s^0 \rightarrow D_s^-(K^+K^-\pi^-)(3)\pi$*, 2011, LHCb-ANA-2011-005.

[83] S. Easo, *Nuclear Science Symposium Conference Record, IEEE*, p. 1554 (2008).

[84] The LHCb Collaboration, *Measurement of direct $\mathcal{CP}$ violation in charmless charged two-body B decays at LHCb*, 2011, LHCb-ANA-2011-023.

[85] R. Aaij *et al.*, *Measurement of $\sigma(pp \rightarrow b\bar{b}x)$ at $\sqrt{s}$=7 tev in the forward region*, Phys. Lett. B, **694**:209, 2010.

Acknowledgement

This last page is dedicated to the people, who made my PhD study possible and helped me out during this years.

First of all, I am very thankful to Prof. Dr. Ueli Straumann for giving me the opportunity to work in his research group as a PhD student for the LHCb experiment and offering excellent working conditions.

I would like to thank Jeroen van Tilburg for his support from the beginning of my PhD study and for introducing me to various topics. He has been a appreciated expert to me concerning many questions over the last years. Furthermore I would like to thank him for proofreading my thesis.

Special thanks go to Nicola Serra, who helped me out a lot to finalise my analysis on the rare decay and for also proofreading my thesis. Thanks for proofreading also goes to Mark Tobin and Olaf Steinkamp.

Many thanks also go to all my colleagues at the University of Zürich, who have been a great support and help. Specially, I would like to thank the members of my office Albert, Angela, Michel and Jonathan.

I am thankful to all people who ensured a well working experiment. This work would not have been possible without the indefatigable work of all persons working at the LHC and the LHCb experiment at CERN.

Finally, I would like to thank Masha, my family and my close friends for the support and encouragement over the years.

Curriculum Vitae

Personal information

Last Name: Salzmann
First Name: Christophe
Day of Birth: 18. August, 1979
Hometown and Canton: Maschwanden, ZH

Education

2007–2011	**Dissertation** in Physics, University of Zürich *LHCb Spectrometer Alignment and Verification of its Performance using the Decay* $B_d^0 \to K^{*0} J/\psi$ Supervisor: Prof. Dr. Ulrich Straumann
2006	**Master of Science** at University of Zürich
2006	**Master Thesis** University of Zürich *Observation of the* $B_s^0 \to \Psi(2S)\phi$ *decay with the DØ Experiment* Supervisor: Prof. Dr. Ulrich Straumann
2000–2006	Study of Physics, University of Zürich
1999–2000	Practical work at Bünter Investment Research, Pfäffikon SZ
1994–1999	**Matura**, typus economics Kantonsschule Enge, Zürich